GAMMA RAY SCATTERING NON DESTRUCTIVE EVALUATION STUDIES

by

PRIYADA . P.

Enrollment No: PHYS02200804005
Indira Gandhi Centre for Atomic Research,
Kalpakkam, India

A thesis submitted to the
Board of Studies in Physical Sciences
In partial fulfillment of requirements
For the degree of

DOCTOR OF PHILOSOPHY

of

HOMI BHABHA NATIONAL INSTITUTE

MARCH, 2013

Homi Bhabha National Institute

Recommendations of the Viva Voce Board

As members of the Viva Voce Board, we certify that we have read the dissertation prepared by **Priyada. P** entitled **"Gamma Ray Scattering Non Destructive Evaluation Studies"** and recommend that it may be accepted as fulfilling the dissertation requirement for the Degree of Doctor of Philosophy.

Date: 14-10-2013

Chairman - **Dr. B. Venkatraman**

N. Mohan Kuma

Date: 14 - 10 - 2013

Convener – **Dr. N. Mohankumar**

R.S. Keshavamurthy

Date: 14/10/2013

Member 1 – **Dr. R. S. Keshavamurthy**

Date: 14 . 10 . 2013 .

Member 2 – **Dr. D. Ponraju**

Date: 14. 10. 2013

Technology
Advisor - **Dr. Shivaramu**

14.10.2013

Examiner- **Prof. B. L Ahuja**

Date:

Final approval and acceptance of this dissertation is contingent upon the candidate's submission of the final copies of the dissertation to HBNI.

Date:
Place:

CERTIFICATE

I hereby certify that I have read this dissertation prepared under my direction and recommend that it may be accepted as fulfilling the dissertation requirement.

I also certify that corrections suggested by examiners are incorporated in this dissertation.

N. Mohan Kumar

Date: 14-10-2013

Place: Kalpatta

Dr. N. Mohankumar

Thesis Supervisor

STATEMENT BY AUTHOR

This dissertation has been submitted in partial fulfillment of requirements for an advanced degree at Homi Bhabha National Institute (HBNI) and is deposited in the Library to be made available to borrowers under rules of the HBNI.

Brief quotations from this dissertation are allowable without special permission, provided that accurate acknowledgement of source is made. Requests for permission for extended quotation from or reproduction of this manuscript in whole or in part may be granted by the Competent Authority of HBNI when in his or her judgment the proposed use of the material is in the interests of scholarship. In all other instances, however, permission must be obtained from the author.

(Priyada. P)

Date: 14-10-2013
Place: Kalpakkam

DECLARATION

I, hereby declare that the investigation presented in the thesis has been carried out by me. The work is original and has not been submitted earlier as a whole or in part for a degree / diploma at this or any other Institution / University.

(Priyada. P)

To my family…

ACKNOWLEDGEMENTS

I thank Dr. Baldev Raj, Shri. S. C. Chetal, former directors of IGCAR and Dr. P. R. Vasudeva Rao, the Director of IGCAR for permitting me to pursue research at this premier institute. I would like to extend my thanks to Shri. S. A. V. Satyamurthy, Director, EIRSG. I am grateful to Dr. B. Venkatraman, Head, RSD and Associate Director, RSEG for his motivating words, advices and insightful suggestions.

This thesis would not have been possible without the help, support, advices and patience of my technology advisor Dr. Shivaramu to whom I am greatly indebted. I have great pleasure to express my deep sense of gratitude to him for all his creative ideas, suggestions and contributions which made my research work interesting. I am grateful to him for finding time to thoroughly read and correct my thesis even after his superannuation. I extend my thanks to Mrs. Pushpa Shivaramu for the care and affection she always showed towards me.

I am grateful to present and past Doctoral Committee members Dr. B. Venkatraman, Dr. N. Mohankumar, Dr. R. S .Keshavamurthy, Dr. D. Ponraju, Dr. P. Mohankrishnan, and Dr. C. P. Reddy for their valuable suggestions during the research work and thesis preparation. I am thankful to Dr. M. Saibaba, AD, RMG and his colleagues for providing the facilities for an enjoyable stay at enclave. The fellowship provided by Department of Atomic Energy is greatly acknowledged.

The help and support of Mrs. M. Margret and Mr. R. Ramar my colleagues at lab and the highly beneficial scientific interactions with them are greatly acknowledged. I thank Dr. L. Thilagam, SRI, AERB for making me familiar with MCNP and for providing the technical supports during my research work. I am thankful to Mr. George Joseph for providing highly beneficial and insightful tutorial on MCNP code. Thanks are due to Mr. Ajay Rawat and Mr. Soubhadra Sen for their support during various stages of thesis work. Help provided by Mr. Sekar, helper during the experiment arrangements is specially mentioned. The contributions of Mr. K. A. Gopal and Mr. K. R. Sekar, IDEAS in establishing this experimental facility are greatly acknowledged. I thank each and every member of RSD and QAD for their support and help provided during various stages of my research work.

Special thanks to my batch mates Pravati, Maneesha, Debasmita, Sarath, Ilaiyaraja, Herojit, Naveen, Jagadeesh, Pradeep, Sudhanshu, Mariyappa, Lakshmoji, Jammu Ravi, Vishnu, Bhubathi and Siva Srinivas for those memorable birthday celebrations and get togethers. The Kalpakkam life wouldn’t have been enjoyable and memorable without the companionship of Rajini, Shima, Juby, Brijitta, Assa, Neethu, Jisha, Sreeja, Sabeena, Rasmi, Meera, Anju, Nitu, Chithra, Anbu, Leona and Kamali. I am thankful to all my teachers from school to college for their support and blessings during all my endeavors. The encouragement and inspiration received from Dr. M. Raveendranathan and Dr. Anuradha Misra are gratefully remembered. I am very much grateful to my friends Krithika, Anjali, Riddhi, Greeshma, Ramina, Dhanya, Vinitha, Mridula, Arun Nair, Anand, Sharath, Krishnadas, Shyam and Suchitra for their support and comradeship. Thanks are due to Krithika for providing me the best help in collecting various literatures related to my thesis work.

The unconditional love and support of my parents and my grandparents has been a great source of strength, happiness and joy throughout my life. I thank them for having faith in my decisions and choices. Thanks a lot to Dr. Varada and Arun for being with me always with great patience as good listeners, strong support and pillars in my life. I express my sincere gratitude to all who had guided and mentored me throughout my life. There may be many whose contributions and supports attributed this thesis work really happened. I thank you all.

(**Priyada. P**)

CONTENTS

Synopsis **i**
List of figures **iii**
List of tables **vii**

Chapter I
Introduction

1.1 Introduction 1
1.2 Ionizing radiation based NDE 5
  1.2.1 Interaction of photons with matter 7
    1.2.1.1 Photo electric effect 8
    1.2.1.2 Rayleigh scattering 9
    1.2.1.3 Compton scattering 9
    1.2.1.4 Pair production 11
  1.2.2 Transmission technique 12
  1.2.3 Scattering technique 13
    1.2.3.1 Measurement model in scattering NDE method 13
    1.2.3.2 Compton profile 16
  1.2.4 Comparison between scattering and transmission technique 17
1.3 Literature survey 18
  1.3.1 Medical physics applications 19
  1.3.2 Agricultural and food processing applications 21
  1.3.3 Industrial applications 22
  1.3.4 Comscan 29
  1.3.5 Scattering imaging modes 29
    1.3.5.1 Point by point mode 29
    1.3.5.2 Line by line mode 29
    1.3.5.3 Plane by plane mode 30
  1.3.6 Estimation of multiple scattering and attenuation factor 30
    1.3.6.1 Multiple scattering 31
    1.3.6.2 Attenuation correction 32
1.4 Motivation 33
1.5 Objectives 34

1.6 Overview of the thesis 35
References 35

Chapter II
Experimental set-up, procedure and Monte Carlo methods

2.1 Introduction 44
2.2 Experimental set-up 44
  2.2.1 Radioactive sources 46
  2.2.2 Detector and electronics 48
    2.2.2.1 Detector 49
    2.2.2.2 Preamplifier 50
    2.2.2.3 HV power supply 51
    2.2.2.4 Spectroscopy amplifier 52
    2.2.2.5 Multi-channel analyzer 52
  2.2.3 Shielding 54
  2.2.4 Collimators 54
    2.2.4.1 Voxel size calculation 55
2.3 Experimental procedure 58
  2.3.1 Automation details 59
  2.3.2 Data analysis 60
2.4 MCNP 62
  2.4.1 Detector, source model 63
  2.4.2 Pulse height spectra simulation 63
References 65

Chapter III
Detection and quantification of thickness loss due to corrosion in mild steel

3.1 Introduction 66
3.2 Algorithm used for attenuation correction and density iteration 68
3.3 Experimental procedure 70
  3.3.1 Sample description 70
  3.3.2 Gamma scattering method 70
  3.3.3 Gammatography 70

3.3.4 Radiography 71
3.4 Quantification of thickness loss 71
References 78

Chapter IV

Measurement of concentration and interface level of fluids/solutions

4.1 Introduction 80
4.2 Sample details 83
4.3 Multiple scattering 84
4.3.1 Scattering experiments 84
4.3.2 Transmission experiments 91
4.4 Relative sensitivity 92
4.5 Fluid interface and level detection 96
4.6 Attenuation correction and surface imaging 100
References 109

Chapter V

Non-destructive characterization of concrete for the detection of inclusions and voids and estimation of water content

5.1 Introduction 111
5.1.1 Radioactive methods for concrete NDE 112
5.2 Detection of embedded inclusions in concrete blocks 116
5.2.1 Sample details 116
5.2.2 One dimensional profiles for locating the voids 117
5.2.3 Algorithm for reconstruction of density in gamma scattering method 121
5.2.3.1 Algorithm for calculation of incident and scattered path lengths in each voxel 122
5.2.3.2 Algorithm for attenuation correction and density reconstruction 123
5.2.4 Reconstruction of density images 128
5.3 Determination of water content in concrete 132
5.3.1 Sample details 132
5.3.2 Quantification of water content from experimental intensities 133

5.3.2.1 Transmission technique 135
5.3.2.2 Scattering technique 136
References 141

Chapter VI

Conclusions, summary and future scope of work

6.1 Conclusions and summary 144
6.2 Improvements and future scope of study 148

Appendix A

Gamma photon techniques for detection of nucleation in super-heated emulsion detectors for neutron dosimetry

A.1 Introduction 150
A.2 Transmission model 152
A.3 Scattering method 154
References 159

SYNOPSIS

Adequate Non-Destructive Techniques (NDT) are required for ensuring the quality and maintenance during manufacture, construction and operation stages in any industry, therein reducing the operating cost and investment. Among various NDT techniques, gamma scattering method is highly useful due to its non contact and single sided access advantages. However, the complications due to attenuation effects, multiple scattering and the resultant difficulties in reconstruction make this technique more uncommon. The aim of this study is to identify some of the attractive applications of the gamma scattering technique for Non-Destructive Evaluation (NDE) and to provide simple recipes for attenuation correction, multiple scattering correction and density reconstruction. A comparison of gamma scattering technique with transmission method is also carried out. All the experiments are performed with an indigenously developed automated experimental setup consisting of a high resolution High Purity Germanium (HPGe) detector and collimated radioactive sources (^{137}Cs, ^{241}Am). The system can function in both transmission and scattering modes simultaneously. The scattered and transmitted intensities of the sample under investigation are obtained from the area under the corresponding peaks in the pulse height spectra. These intensities are related to the density of the sample. Hence, any variation in density or presence of defect reflected in these intensities and quantification of defects is carried out by using these intensities. The experimental results are supported by those simulated using Monte Carlo N Particle (MCNP) code. The following cases are investigated. The corrosion detection in mild steel and intercomparison of results obtained by gamma scattering, gammatography and radiography techniques is carried out. The minimum detectable limit of thickness loss is 1.4 mm. The fluid-fluid, fluid-air interface level detection and density determination by gamma scattering method and inter comparison with transmission (gammatography) technique is carried out. The obtained accuracies and resolution of the level detections and density measurements are higher in case of gamma scattering method compared to transmission method. An improved gamma scattering method for determination of concentration of low atomic number solutions is presented. A nonlinear relation between the gamma scattered intensity and the sample radius including the attenuation and multiple scattering contributions was suggested in this work. The scattered intensity per electron from fluid samples of various scattering volumes were simulated using MCNP code and they varied according to the prescribed nonlinear relation with an accuracy R^2 greater than 0.90. The density values obtained by extrapolating the above nonlinear fit were in good agreement with that of standard densities. The application of gamma scattering technique to detect voids embedded in concrete blocks and their characterization is demonstrated and this technique could locate the hidden and surface voids of various sizes ranging from 0.5 - 3 cm diameter from the intensity profile. A simple algorithm for density reconstruction for any scattering angle from the scattered intensities is developed. The algorithm is verified by reconstructing the densities from the scattered intensities obtained from a homogeneous concrete block of density 2.24 g/cm^3 and the resultant mean density is 2.2217 g/cm^3. The utility of gamma scattering technique to quantify the water (moisture) content in concrete is tested and good agreement with the gravimetric and transmission methods is obtained within accuracy of 10%. The superiority of gamma scattering NDE technique over transmission technique for low atomic number samples is explored in detail in the present study. The theoretical calculations and algorithms described are simple and easy to execute. These studies could emphasize clearly the importance of scattering technique in NDE applications and the improvements required for the experimental system for achieving higher accuracy and portability.

LIST OF FIGURES

Figure Number	**Caption**	**Page Number**
1.1	Schematic representation of gamma ray interaction processes with matter	8
1.2	Schematic representation of the scattering model	14
2.1	Schematic of the experimental set-up	45
2.2	Experimental set-up	45
2.3	Decay scheme of ^{137}Cs	47
2.4	Decay scheme of ^{241}Am	48
2.5	Block diagram of detector system with electronics	48
2.6	Cross sectional image of 50% efficiency detector	50
2.7	Geometry used for calculating the voxel size	55
2.8	Calculated voxel sizes for different collimator combinations (source diameter x detector diameter) as a function of scattering angle.	56
2.9	Block diagram of automation and data collection	59
2.10	Images of control panel and data collection screen	60
2.11	PHS of scattered (252 keV) and transmitted (661 keV) intensities	61
2.12	Continuum subtraction for photopeak	61
3.1	Geometry for calculating the attenuation factor	68
3.2	Experimental scattered PHS obtained from reference and corroded MS plates for scattering angles of 109° (a) and 91° (b).	71
3.3	Experimental scattered PHS for scattering angle of 109° obtained from normal and from different spatial locations of corroded MS plates and corresponding photo peaks are shown in the inset	73
3.4	Cross sectional view of experimental set-up modeled in MCNP	73
3.5	Comparison of MC simulated scattered spectra with experimental results at scattering angle 91°	74

3.6 Simulated PHS for various amount of corrosion 75

3.7 Quantitative estimates of the values of S/N plotted as a function of thickness loss 75

3.8 Radiographic images of (a) reference sample and (b) corroded sample 76

3.9 Measured thickness loss in cm by gamma scattering, radiography and gammatography techniques 77

4.1 Experimental set-up with source, sample and detector labeled 84

4.2 Comparison of MCNP spectra with experimental ones for water (left) and 15 wt % NaCl (right) 85

4.3 Comparison of MCNP spectra with experimental ones for glycerine (left) and olive oil (right) 85

4.4 $n_c/\Delta V$ as a function of sample radius for water , 5 wt % K_2HPO_4 and 30 wt % K_2HPO_4. The fitted curves with fitting parameters (inset table) along with extrapolated ones are shown 87

4.5 $n_c/\Delta V$ as a function of sample radius for 2 and 10 wt % KI. The fitted curves with fitting parameters (inset table) along with extrapolated ones are shown 87

4.6 $n_c/\Delta V$ as a function of sample radius for 5 wt % and 25 wt % glucose and NaCl. The fitted curves with fitting parameters (inset table) along with extrapolated ones are shown 88

4.7 Multiple to single scattering fraction (S_m/S_1) for various solutions as a function of radius of the sample 90

4.8 Transmission attenuation co-efficient obtained from MCNP simulations as a function of sample thicknesses for 0.7 and 0.5 cm detector collimators 92

4.9 Relative sensitivity as a function of concentration in transmission (left) and scattering (right) methods for K_2HPO_4 solution 93

4.10 Relative sensitivity as a function of fluid density in transmission (left) and scattering (right) methods 94

4.11 Measured transmitted and scattered counts as a function of vertical height of glass container 96

4.12 Scattered intensity profile of glycerine olive oil column for various 100 durations

4.13 Image of the simulated sample with both incident and scattered paths are shown 101

4.14 Surface image of water hexane column from raw counts (left) and attenuation corrected counts (right) 102

4.15 Scattered attenuation corrected images of various immiscible fluid combinations in different containers 103

4.16 Relative scattered counts (solution/water) for varying concentrations of (a) NaCl, (b) $C_6H_{12}O_6$, (c) K_2HPO_4 and (d) KI respectively 104

4.17 Densities obtained by i) non-linear extrapolation method correcting for attenuation and multiple scattering ii) from raw scattered intensity ratio and iii) by attenuation correction only for various solutions are compared with the standard densities 105

4.18 $n_c/\Delta V$ as a function of sample radius for glycerine (left) and and hexane (right). The fitted curve (inset equation) along with extrapolated ones is shown 107

4.19 Comparison of densities of fluids obtained from scattering and transmission methods with the standard densities 108

5.1 Concrete samples ((a) sample 1 and (b) sample 2) embedded with voids 116

5.2 One dimensional scattered intensity profile as a function of vertical height for large and small voxel sizes 117

5.3 Scattered and transmitted intensity profiles of concrete sample 1 embedded with two voids 118

5.4 Scattered and transmitted intensity profiles of concrete sample 2 embedded with four voids of different sizes 119

5.5 Number of scattered photons per electron ($n_c/ \Delta V$) as a function of the concrete sample radius inside the voxel (fitted and extrapolated curve) 120

5.6 Geometry for calculating the attenuation factor 122

5.7 Reconstructed density contour plots of a concrete layer from the MCNP and experimental intensities 128

5.8 Surface contour plots of sample 1 (a) and sample 2 (b) 129

5.9 Three dimensional images of sample 1 (a) and sample 2 (b) (all dimensions are in cm) 130

5.10 Surface images of sample 2 obtained from reconstructed densities with error correction (a) and without error correction (b) 131

5.11 Transmitted intensities as a function of volumetric water content 135

5.12 Linear attenuation coefficient calculated from transmitted intensities as a function of volumetric water content 136

5.13 Scattered intensity as a function of volumetric water content 137

5.14 Attenuation correction factor as a function of volumetric water content 138

5.15 MCNP simulated PHS for dry concrete and water saturated concrete 139

5.16 Scattered intensities and volumetric content determined from the same sample 140

A.1 Photographs of bubble detectors before (a) and after neutron exposure (b) 151

A.2 Transmitted PHS of sample 1 and sample 2 before (0 mSv) and after (8.3 mSv) neutron exposure 153

A.3 Experimental transmitted intensities plotted as a function of neutron dose along with the error bars for sample 1 and sample 2. The dashed curve indicates the least square fitting as per the theoretical model formulated and the fitted parameters are shown in the inset 154

A.4 Scattered PHS of sample 1 and sample 2 before and after neutron exposure for various doses 155

A.5 Experimental scattered intensities plotted as a function of neutron dose along with the error bars for sample 1 and sample 2. The dashed curve indicates the least square fitting as per the theoretical model formulated and the fitted parameters are shown in the inset 156

A.6 Relative sensitivities of transmission and scattering techniques for sample 1and sample 2 as a function of neutron dose (a and b respectively) and relative sensitivities of transmission experiments for 59.54 and 661.6 keV gamma energies (c) 157

LIST OF TABLES

Table Number	Caption	Page Number
4.1	Multiple to single scattering ratio calculated from the constants obtained from fitting for various solutions	89
4.2	Measurement sensitivity of transmission and scattering technique as per equations (4.5) and (4.6)	95
4.3	Immiscible fluid-fluid interface levels (measured from the bottom of the glass container) along with levels obtained from scattering and transmission methods	98
4.4	Concentration of solutions derived from the densities obtained by scattering method	106
5.1	Fractional weights of constituents elements in concrete samples with various amount of water content.	134
5.2	Attenuation factor calculated using XCOM for concrete sample with various amount of water content	134
5.3	Comparison of volumetric water content determined gravimetrically, transmission method and scattering method	139

PUBLICATIONS

List of publications in referred international journals

1. **P. Priyada**, M. Margret, R. Ramar, Shivaramu, M. Menaka, L. Thilagam, B. Venkataraman, Baldev Raj, "Intercomparison of Gamma Scattering, Gammatography and Radiography Techniques for Mild Steel Nonuniform Corrosion Detection", Review of Scientific. Instruments. 82(3), 035115 (2011)
2. **P. Priyada**, M. Margret, R. Ramar, Shivaramu, "Intercomparison of gamma ray scattering and transmission techniques for fluid–fluid and fluid–air interface levels detection and density measurements", Applied Radiation and Isotopes, 70 (3),462-469 (2012)
3. **P. Priyada**, R. Ramar, Shivaramu, "An improved Compton scattering method for determination of concentration of solutions", Applied Radiation and Isotopes, 70 (10), 2421-2427 (2012)
4. **P. Priyada**, R. Ramar, Shivaramu, "Application of gamma ray back-scattering technique for non-destructive evaluation of voids in concrete", Applied Radiation and Isotopes, 74, 13-22 (2013)
5. **P. Priyada**, R. Ramar, Shivaramu, "Determining the water content in concrete by gamma scattering method", (Communicated to Annals of Nuclear Energy)
6. **P. Priyada**, R. Ramar, H. Krishnan, S. Viswanathan, Shivaramu, "Gamma photon techniques for detection of nucleation in super-heated emulsion detectors for neutron dosimetry", (Communicated to Radiation Protection Dosimetry)

List of conference papers

1. **P. Priyada**, M. Margret, R. Ramar, M. Menaka, Shivaramu, B.Venkataraman and Baldev Raj, Inter Comparison of Gamma Scattering with other NDE Techniques for MS Corrosion Detection, NDE-2010 Kolkata.
2. Shivaramu, **P. Priyada**, M. Margret, R. Ramar, Intercomparison of gamma ray scattering and transmission techniques for fluids interface level and density determination, Accepted for Oral Presentation and available online, 5th Pan American Conference for NDT, Mexico.
3. **P. Priyada**, M. Margret, R. Ramar and Shivaramu. Intercomparison of gamma ray scattering and transmission techniques for fluids interface level and density determination, NDE-2011 Chennai.
4. **P. Priyada**, R. Ramar and Shivaramu, Intercomparison of gamma scattering and transmission techniques for measurement of water content in concrete, Nineteenth National Symposium on Radiation Physics (NSRP19), 2012, Mamallapuram, Chennai.

Chapter I Introduction

1.1 Introduction

Quality and reliability are inevitable for all products and services and hence it is required to monitor and maintain them. Non Destructive Evaluation (NDE) techniques have been widely used for the aforesaid purpose. Inspecting or testing structures and materials without destructing it and thus evaluating the flaws or defects quantitatively, is known as NDE. “NDE is the examination of an object with technology that does not affect the object’s future usefulness” is the definition given by American Society of Non Destructive Testing [1]. Quality control is very important from the stage of manufacturing to testing the final product and further monitoring during the operation of the system. Pre-service and in-service assessment using proper NDE methods assure safe and reliable performance of the plants, therein reducing the operating cost and investment [2]. There are applications for NDE methods in medical imaging and diagnoses, quality control, security check-up, on line manufacturing process control, material characterization and flaw detection. Even though NDE do not give any guarantee that failures won’t happen, it can detect the flaws before failure and thus can minimize the probability to occur.

Human body is the best sensor and on our day to day life we are utilizing it to detect something or the other through heat, touch, vision, sound and smell. We can say precisely that NDE is an extension of this sensing with the help of external gadgets. The history of NDE starts from early 1800's, but its growth is rapid only after 1950. As the technology advances, with the help of recent computation advancements, deeper knowledge on materials and the effective sensors and detectors the field of NDE is also growing day by day [3]. In a typical Non Destructive Testing (NDT), the source which emits some form of energy is sent to the object under study or evaluates the energy generated intrinsically in the object. Inside the object the energy alters and then exits to be detected by a sensor. This detected energy carries information about the nature of the object and can be interpreted later. This source object sensor/detector arrangement is the gist of NDE [4]. Handling the noise produced during the test, interpretation of the received signal, proper mathematical modeling and finally analysis/ imaging/ quantification of the material are the main challenges in this field. In industrial NDE, interpretation plays a vital role and hence some prior understanding about the object is also essential. There are more than 40 techniques that can be categorized as NDE techniques and which are constantly researched and developed to enhance its effectiveness. But six NDE methods form the base for all other techniques [5]. An overview of these major six NDE techniques is given below [6].

Visual examination: - Visual examination is the simplest NDE method where either scattered or transmitted light from an object is detected. The most important detector in this technique is human eye. With the aid of magnifiers and external light sources, the visibility can be enhanced. When inspection cannot be performed directly due to accessibility restrictions, borescopes (fiber optic cable for the passage of incident and reflected light), miniature cameras and video recordings are used. This technique is limited mainly to surface defect determination.

Liquid penetrant testing: - Liquid penetrant testing is based on the capillary action of the materials and it is mainly used to detect the surface openings and discontinuities in non porous materials. Steps involved in this method are cleaning of the surface of the test sample, applying the penetrant, removal of the penetrant after the required duration and the application of developer for further interpretation. Penetrant can be applied to the sample either by dipping it into a tank containing the penetrant solution or by spraying it over the sample. Through the surface cracks and openings the penetrating solution enters deeper to the material through capillary action. After the dwell time the excess penetrant is removed from the surface using proper solvents or emulsifiers. Then the surface is dried and a developer is applied on it. The trapped penetrant inside the cracks comes out, which indicates the location of flaw. This technique is useful for inspecting the new and in-service materials and to provide quality control checks. It is highly inexpensive, portable and sensitive but utility is limited to surface opening cracks. Moreover, this method is not effective for hot objects.

Magnetic particle testing: - When a magnetic flux is applied to a ferromagnetic material, the magnetic fields align themselves. But the presence of crack or discontinuity in the material opposes the field and so the field bends around the crack to realign. In this case some of the magnetic lines exit and re-enter the material forming a leakage field. When minute magnetic particles are sprinkled over the material, these particles aggregate and gather by the leakage field indicating the presence of discontinuity. The outline of the discontinuity including its location, size, shape and extend can be obtained from this technique. Magnetic particle testing is inexpensive, portable and quicker. However, its application is limited to ferromagnetic materials with surface or near surface defects. Post inspection demagnetization and surface cleaning are also required.

Radiographic testing: - Radiographic testing is used to detect the internal defects in a material. A radiographic film is placed on one side of the sample and the sample is exposed to X-rays or gamma rays. X-rays or gamma rays attenuate while passing through the material depending on the internal structure. The exposed film after processing reveals the shadow image of the sample to obtain the data regarding the flaws. This method is widely used for defect detection in casting, welding and forging. Radiography testing can perform over a large area of the sample at the same time and it is very useful to obtain the internal structure and discontinuities. The radiographic film processed is a permanent record and the analysis can be done away from the work site. But this method requires precautions and proper training to avoid the hazards due to radiation exposure. This method requires access to both the sides of the sample and is not suitable for thick samples and planar discontinuities.

Ultrasonic testing: - Ultrasonic testing utilizes a sound wave of frequency 0.5 to 20 MHz. The sound wave travel through the material with some energy loss and using a transducer reflected or transmitted sound waves are detected for further interpretation. This method is widely used for thickness measurement, flaw detection and mechanical property determinations. The advantages of this technique include higher penetration, more accurate results, rapid and automated results with single sided access. But it is not suitable for complex geometries and rough surfaces. A direct contact with the sample and surface preparation are requisites in this technique. Due to its point by point scanning nature extensive test duration is required for extended structures.

Eddy current testing: - An eddy current is generated in the sample by bringing it close to an alternate current carrying coil. The magnetic field of the coil will be affected by the magnetic field of the eddy current and these changes will be in accordance with the material near the coil. Hence these modifications are considered for detecting the discontinuities. This technique is useful for detecting thin thicknesses like coating, defects in tube walls and sorting the material. But its application is limited to conductor materials with smooth surfaces. Its penetration depth is limited.

Every technique is having its own advantages and limitations and the prior knowledge of these ensures the integrity of the analysis. Often a second opinion using another technique is also required to ensure the status of the material.

1.2 Ionizing radiation based NDE

Radiations like X-ray, gamma or neutron are used as the source of energy in radioactive NDE methods and the special attractive features of these sources are listed below.

1. Highly penetrating nature of these radiations enables the inspection of thick and dense structures.
2. Since these radiations interact directly with the electrons, it can provide information about material’s density and composition which other techniques can’t
3. No direct contact with the object is required and hence this technique is highly recommended in harsh environments (highly poisonous, high temperature, high pressure, corrosive, explosive etc.).
4. Radiation interacts with matter regardless of its physical properties, thermal, magnetic and electric conductivity.
5. No surface preparations are required.

In photon based NDE techniques X-rays or gamma rays are utilized due to their penetrating, non invasive and non destructive nature. X-rays and gamma radiation differs in their origin, i.e., X-rays are produced by electron transitions between the shells of an excited atom while gamma rays are produced by nuclear transitions. In X-ray machines the production is achieved by bombarding a high atomic number target with a beam of fast electrons. The incident electrons interact with atomic electrons and shift some of them to excited states. As the excited electrons return to normal states, energy is released in the form of X-rays. The X-ray energy will be equal to the difference between the excited state and normal state energies and this is characteristic to the target material. Bremsstrahlung radiation is also produced due to the deceleration of electrons and it can have maximum energy corresponds to the incident electron energy. Thus an X-ray spectrum consists of a continuous part due to bremsstrahlung and characteristic part due to atomic transitions.

Gamma rays are emitted after a beta decay or alpha decay. Parent nuclide undergoes beta decay or alpha decay leaving the daughter nuclide in excited state. This excited nuclide will come to its normal state along with one or more gamma radiation and these gamma rays carry the difference in energy between the excited and normal state. Thus gamma radiations from isotopes are monochromatic in nature. The gamma photon energy of each isotope is unique and the selection of isotope for the NDE application is based on its energy and half life. The energy of gamma photons is higher compared to that of X-ray photon due to the fact that the origin of former is from the nucleus. The penetration of photons depends on its energy and density and thickness of the sample. X-rays are widely accepted for surface or subsurface defect detection due to their higher intensity and hence reduced measurement duration. But gamma photons from radio isotopes are preferred for higher penetration. Due to their continuous energy spectrum of X-rays, it is difficult to obtain information without the use of proper filters. On comparison with X-ray sources, gamma ray sources have the advantages of portability, no power requirement, monochromatic energy, small size and deeper penetration. Hence, the selection of X-rays or gamma rays for the non destructive applications can be made judiciously based on the requirement, sample properties and time limitations. Commonly used radioactive sources and their typical applications in industrial measurements are reviewed in detail by Johansen and Jackson [7]

Gamma radio isotopes are very much useful in industrial gauging applications and their utility for gauging of hot rolled metal strips is one among them. Applications of radio isotopes include the tracer applications, plant mutation for improved quality products, pest control and food preservation [8, 9]. Even though radiations from isotopes are useful for many applications, great care has to be taken while handling them. Generally awareness and training are required for the operator regarding the safe handling of isotopes. All the photon based NDE techniques are based on the interaction of photons with matter and in order to understand these techniques, their feasibilities and advantages, photon interaction with matter has to be studied thoroughly.

1.2.1 Interaction of photons with matter

Photons carry no charge and they interact with matter mainly through four processes; (i) Photo electric effect, (ii) Rayleigh scattering, (iii) Compton scattering and (iv) Pair production [10, 11]. Schematic representations of all these four interactions are given in figure 1.1.

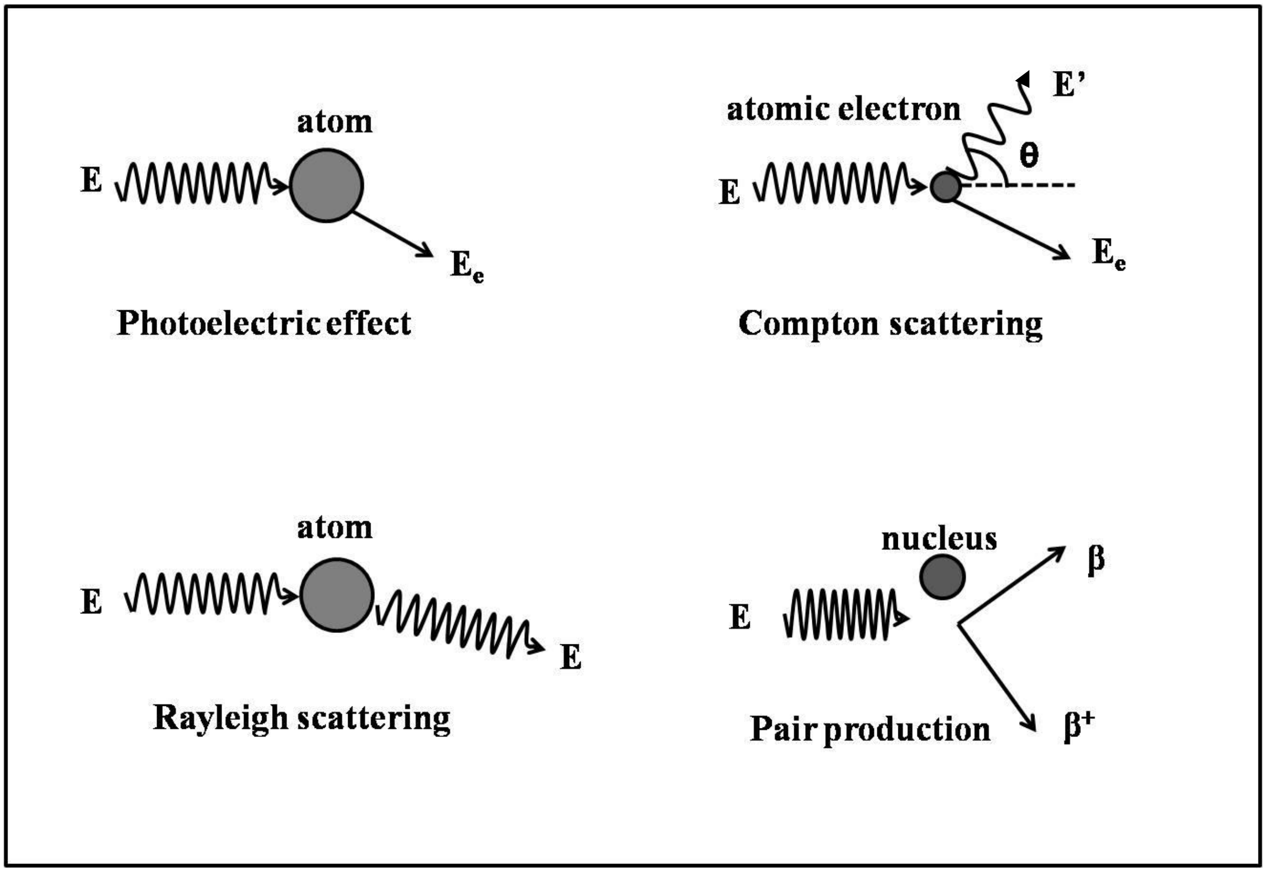
atom
E
E_e
Photoelectric effect
atomic electron
E'
θ
E
E_e
Compton scattering
atom
E
E
Rayleigh scattering
nucleus
β
E
$β^+$
Pair production

Figure 1.1 Schematic representation of gamma ray interaction processes with matter

1.2.1.1 Photo electric effect

A gamma ray can interact with matter in such a way that it loses all its energy to knock out an electron mainly from tightly bound shells and this process is known as photo electric effect. Some of the incident energy is used to overcome the binding energy of the electron, and the remaining energy is converted to the kinetic energy of the electron. Some of the energy remains with the atom for momentum conservation. The vacancy created is filled by an electron from a higher shell followed by X-ray or Auger electron emission. The probability of photo electric effect is largest for K shell electrons.

Photo electric effect is predominant in low energy region (<0.1 MeV) and high Z absorbers. Probability for this process is given by

$$\tau \propto \frac{Z^{\approx(4-5)}}{E^{3}} \qquad (1.1)$$

where Z is the atomic number of the target and E is the energy of the incident photon beam. Photo electric interaction is the predominant interaction for low energy gamma rays, X-rays and bremsstrahlung radiations. The dependence of cross section on atomic number is explored in NDE applications to obtain composition and effective atomic number information.

1.2.1.2 Rayleigh scattering

Rayleigh scattering is elastic in nature and hence no energy transfer occurs due to scattering. In Rayleigh scattering, the interaction of incident photon takes place with a bound atomic electron and hence the whole atom takes the recoil. It is significant only for low energy and high Z absorber situations. Rayleigh scattering cross section is proportional to $Z^{2.5}$.

1.2.1.3 Compton scattering

When the incident energy E >> B.E (binding energy of electron), the electron can be treated as a free electron. Compton scattering is the interaction of photons with free electrons. In Compton scattering, when a photon collides with a free electron which is at rest, it loses some amount of energy to electron and deflects from original direction. A recoil electron also emitted from the material and the direction of recoil will be in such a way that the momentum is conserved. In this process the least tightly bound electrons of the outermost shells are recoiled. Energy of incoming photon will be shared by scattered photon and recoiled electron and thus total energy will be conserved. Compton scattering is incoherent in nature. The scattered energy and the incident energy are related through the scattering angle and can be derived from the equations of conservation of momentum and energy. The scattered energy E´ is related to the E and scattering angle θ as follows:

$$E' = \frac{E}{[1+\frac{E}{511}(1-\cos(\theta))]} \tag{1.2}$$

E and E´ should be represented in keV in the equation (1.2). Microscopic cross section of this process (probability of interaction per electron) is a function of scattering angle and the same is given by Klein-Nishina relation where r_0 is the classical electron radius.

$$\frac{d\sigma_{KN}(E,\Omega)}{d\Omega} = \frac{r_0^2}{2}\left[\frac{E'}{E}\right]^2\left[\frac{E'}{E}+\frac{E}{E'}-\sin^2(\theta)\right] \tag{1.3}$$

At small energies it will reduce to Thomson's scattering relation (r_0^2 $(1+\cos^2\theta)/2$). In the case of scattering from a volume, many electrons are available for photons to interact. The electron density (ρ_e) of a material depends upon its material density (ρ) and the relation is given below.

$$\rho_e = \rho\, N \frac{Z}{A} \tag{1.4}$$

where N is the Avogadro's number and A is the atomic mass. Thus the probability of Compton scattering from a volume depends upon the number of available electrons and in turn to the density and atomic number of the target. Any variation in material density of the target, from which the photon scatters, will reflect in the scattering cross section and thereby in the scattered intensity. This is the basic physics which makes this process attractive for NDE applications.

Even though Klein–Nishina relation is derived on the assumption that electrons are free and at rest, in reality it is not so. Hence, an incoherent scattering function represented by

S is introduced considering the momentum transfer .When the incident energy is greater than binding energy of the electrons; free electron assumption is considered to be valid. The modified equation for cross section is given by

$$\frac{d\sigma\ (E,\Omega)}{d\Omega} = \frac{d\sigma_{KN}(E,\Omega)}{d\Omega} S(E,\theta,Z) \tag{1.5}$$

Tables of incoherent scattering functions were generated and available in literature [12]. The Compton scattering is predominant interaction in the energy range 50 keV to 1.5 MeV. The probability of Compton scattering is more for low Z materials and composites. Unlike other interactions, the Compton scattering cross section is directly related to material density of the target.

1.2.1.4 Pair production

A gamma ray with energy greater than 1.02 MeV can create an electron positron pair in the vicinity of a nucleus. The limit of 1.02 MeV is because that it is the minimum energy required for creating electron and positron. Rest of the incident energy will be shared by the electron and positron as kinetic energies. This process is known as pair production. The presence of nucleus is necessary for momentum conservation. When the gamma energy exceeds 2.04 MeV, pair production can take place in the presence of electron field also [13]. After production, both positron and electron lose their kinetic energy by excitation, ionization or bremsstrahlung process and after losing the energy positron and electron pair annihilates to produce 2 quanta of photons having energy 0.51 MeV. Probability for pair production is given by

$$\tau = \frac{Z^2}{137}\left(\frac{e^2}{m_0 c^2}\right)^2 \qquad (1.6)$$

When radiation passes through any material, any of the following interactions can happen and the total probability of any sort of photon removal independent of interaction mode is given by mass attenuation coefficient (μ/ρ). The contributions of each of these processes on total attenuation coefficient depend on the photon energy and target atomic number. Total attenuation coefficient is given below:

$$\frac{\mu}{\rho} = \frac{\mu}{\rho}_{ph} + \frac{\mu}{\rho}_{Com} + \frac{\mu}{\rho}_{Ray} + \frac{\mu}{\rho}_{pp} \qquad (1.7)$$

There are two different modes of gamma photon NDE techniques; (i) transmission mode; where source and detector are placed on the opposite sides of the object (ii) scattering mode; where both the source and sample are placed on the same side of the object. Gamma transmission technique is well established and industrial Computed Tomography (CT) systems employing this technique are available. Photon scattering NDE method is well studied, still less popular due to the complications in quantification arising from attenuation and multiple scattering effects and due to requirement of longer scanning time. Details about these two techniques are given below.

1.2.2 Transmission technique

When a collimated beam of monochromatic gamma photons penetrates the material, the attenuation of the gamma rays will occur and the amount of attenuation depends upon the incident photon energy, material properties such as atomic number, composition and density.

This is the basic principle behind the gamma transmission technique. Transmitted intensity is related to incident intensity and material properties as follows:

$$I_t = I_{0t}\exp(-\mu x) \tag{1.8}$$

where I_{0t} is the intensity of incident radiation, I_t is the transmitted intensity, μ is linear attenuation coefficient of the target and *x* is the thickness of the target. Linear attenuation coefficient (product of mass attenuation coefficient and density) is a function of incident energy, material density and composition. Thus lighter materials absorbs photon lesser compared to denser materials. Hence the transmitted intensity carries compressed information regarding the density and composition properties of the material through which it traversed. Radiography systems and CT systems utilize this theory.

1.2.3 Scattering technique

Scattering is considered as a problem in radiology and CT due to its effects on image quality, sensitivity and reconstruction complexities. But the information carried by scattered radiations are useful to retrieve the material properties such as density, composition and this is utilized in scattering technique for analysis and interpretations.

1.2.3.1 Measurement model in scattering NDE method

The schematic diagram of backscatter geometry of the experimental arrangement is shown in figure 1.2. A scattering angle greater than 90° can be considered as back scatter geometry due to the possibility of placing source and detector on the same side of the sample. Source and detector are shielded and collimated and a detailed description of the experiment system is provided in the next chapter. The scattering volume determined by the source and detector collimators is represented by the point P.

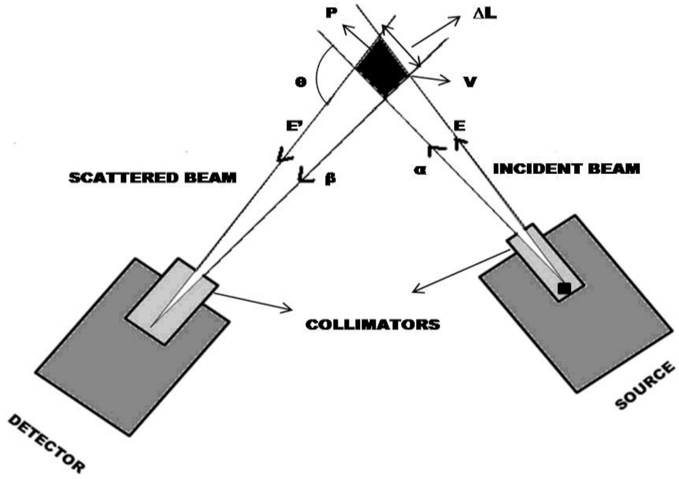

Figure 1.2 Schematic representation of the scattering model

The intersection of source beam and detector field of view is the interested scattering volume known as voxel. The scattered intensity carries information about the material inside this voxel. The basic assumptions of this model are (i) the attenuation through air is neglected (ii) the photons are undergoing scattering only once (iii) the contribution from the entire scattering volume is lumped into one point (iv) the contribution in variation in θ and corresponding variations in E' are neglected and (v) the material density is homogeneous inside the voxel. Many of these assumptions demand the voxel to be sufficiently small [4].

The number of detected photons depends on the number of scattered photons as well as on the attenuation all along the path within the material. The path of photons from the source to the detector can be divided into three stages which determine their contribution to the measured signal. In the first stage, the photons travel from the source to the scattering point P along path α. In an homogeneous material gamma rays are attenuated according to the equation (1.8) and can be re written as:

$$I_{1s} = I_{0s} \exp - \left[\left(\frac{\mu(E)}{\rho} \right) \rho\, x \right] \tag{1.9}$$

where I_{1s} and I_{0s} are the transmitted and incident intensity, respectively, $\mu(E)/\rho$ is the mass attenuation coefficient of the material for photons of energy E, ρ is the density of the material and x is the length of path α. The second stage of development for the signal is the scattering towards the detector which occurs at point P. The scattered intensity, I_{2s}, is determined by:

$$I_{2s} = I_{1s} \frac{d\sigma_{KN}(E,\Omega)}{d\Omega} S(E,\theta,Z)\, d\Omega\, \rho_e V \tag{1.10}$$

where $d\Omega$ is the solid angle subtended by the detector and its collimator, V is voxel size and ρ_e is the electron density at point P. The electron density at P is the material property that of interest and attempting to measure. It is proportional to the physical density ρ as described in equation (1.4). The third stage of development is the transport of the scattered photons back through the materials towards the detector. The signal is further attenuated, so that:

$$I_S = I_{2s} \exp - \left[\left(\frac{\mu(E')}{\rho} \rho\, x' \right) \right] \tag{1.11}$$

where I_s represents the intensity reaching the detector, $\mu(E')/\rho$ is the mass attenuation coefficient for scattered photons of energy E' and x' is the length of path β within the material. Combining the expressions for the three stages, the signal intensity corresponding to point P can be written as:

$$I_S(P) = I_{0s} \exp\text{-} \left[\left(\frac{\mu(E)}{\rho} \right) \rho\, x \right] \frac{d\sigma(E,\Omega)}{d\Omega} S(E,\theta,Z)\, d\Omega\, \rho_e(P) V \exp\text{-} \left[\left(\frac{\mu(E')}{\rho} \right) \rho\, x' \right] \tag{1.12}$$

According to (1.12) we can expect an unambiguous interpretation of the signal $I_S(P)$ as a function of material density at point P. For a fixed source and detector positions and the collimator sizes, equation (1.12) reduces to:

$$I_S(P) = K\rho AF \tag{1.13}$$

where, $$K = I_{0s}\frac{d\sigma(E,\theta)}{d\Omega}S(E,\theta,Z)\,d\Omega\;N\frac{Z}{A}V \tag{1.14}$$

and $$AF = \exp\text{-}\left[\int_0^x\left(\frac{\mu(E)}{\rho}\right)\rho\,dt\right]\exp\text{-}\left[\int_0^{x'}\left(\frac{\mu(E')}{\rho}\right)\rho\,dt'\right] \tag{1.15}$$

K is a constant for given experimental setup and AF is the attenuation factor. It is clear from the equation (1.13) that for a given experimental setup any variation in sample density will reflect in the scattered intensity and this is utilized for identification of flaws, voids or defects in materials. Generally in Compton scatter applications, the incoherent scattering function is ignored since the coupling between electrons and nuclei is small compared to the majority of photons used in medical and industrial applications [14].

1.2.3.2 Compton profile

Generally the area under the photopeak or scattered intensity is used for density gauges and photon scattering imaging systems. When radiations undergo Compton scattering, the scattered beam experiences a Doppler broadening due to the movement of electrons. Thus the shape and width of the scattered peak also show variations with the composition and electron density. The study of this broadened line shape (Compton profile) provides information regarding electronic structure of atoms, molecules and solids [15, 16].

Electronic structure and momentum calculations of various compounds are still a happening research area [17-19].

1.2.4 Comparison between scattering and transmission technique

Photon based transmission and scattering NDE methods are having their own advantages and disadvantages. The suitable technique can be chosen according to the requirement in terms of duration, sample size, accessibility etc. A detailed comparison of these techniques is given below.

- Since the source and detector are to be placed on the opposite sides of the detector, transmission technique cannot be employed for situations where two side accesses are restricted. But the single sided access property of scattering technique is useful in such situations and this is the most attractive feature of this technique.
- Similarly scattering can take place in any direction and provision for placing multiple detectors simultaneously is available in scattering method. This feature provides a feasibility to select the detector position in such a way that the attenuation is minimized [20]. But this degree of freedom is limited in transmission method.
- As it is clear from the equation (1.8), transmitted intensity carries line integrated information along the photon path whereas scattered intensity carries the information from the scattering volume. Thus retrieving localized information is not possible through transmission technique without multiple projections. But scattered intensity provides localized and volume information.
- Due to the differential or localized nature of scattering technique, it is highly sensitive to smaller variations compared to transmission technique. Moreover, scattering technique is highly sensitive to low atomic number composites due to higher cross

section of Compton scattering. Thus the fractional contrast is better in the case of scattering technique and it is affected by superposition effect in transmission case. Furthermore, the contrast is independent of defect size in scattering technique [21]. This high contrast and deeper penetration of scattering technique is attractive to detect the light materials inside the heavy ones [22].

- Multiple projections are required for reconstructing the images in transmission technique whereas it can be done directly from scattering intensities.
- Scattering technique is sensitive to plane defects which are collinear to plane. This advantage can be utilized for detecting the delaminations in composite materials.
- Compton scatter imaging technique is having an additional advantage of imaging the electron density of the object directly rather than the attenuation coefficients in case of transmission tomography.
- A portable scattering system can be designed with both source and detector attached to the same cabin and this avoids the errors that can arise due to the alignment of the source and detector at the same height in the transmission system.
- The probability of scattering to a particular direction is very small compared to its transmission probability. Due to this reason higher scanning speed can be achieved in transmission technique. In scattering technique scanning speed depends on the source strength, geometry of the system and the size of collimators.

1.3 Literature survey

A detailed review of applications of Compton scattering technique utilizing either X-ray or gamma ray in various fields including medical, agriculture, food processing and industry are given below.

1.3.1 Medical physics applications

The direct relationship of Compton scattered intensity with the electron density of the scattering material made gamma scattering technique an attractive NDE technique. In 1959 Lale [23] introduced scattering technique in medicine for the examination of internal tissues. Later many groups had worked in this field with further modifications and improvements for various applications. Bone mineral density determination for the diagnosis of osteoporosis [24-33], iodine content determination [34.35], fat ,tissue and other body components characterization [36-38], chest/lung imaging [39-41] etc. are some of the various applications found in literature where gamma backscattering technique is utilized.

Clarke and Van Dyk introduced a combination of scattering and transmission method with the scattered and transmitted beams occupy the same spatial path for bone mineral content measurement [23]. In this method, sources and scattering angle have to be selected in such a way that scattered energy of primary beam should be the energy of transmitted source. Two transmitted and two scattered intensities with the help of 180º rotation of the source – detector system were measured for calculating the electron densities with respect to water. Combinations of ^{60}Co and ^{137}Cs [23], ^{198}Au and ^{203}Hg [24] were some of the sources used in earlier systems. A clinical study of bone mineral density quantification using low energy sources ^{153}Sm and ^{170}Tm using a 90° scattering angle was carried out and the measured densities varied between 1.11 g/cm^3 and 1.53 g/cm^3 [25].

In dual energy scattering method, a gamma isotope with more than one characteristic gamma energies are employed instead of two sources and transmission measurements. This method eliminates the need of reorientation of the source – detector system. The scattered intensities obtained for two different scattered photo peaks are recorded and two simultaneous equations formed from these measurements are solved for electron density. These two intensities are from same scattering volume and hence due to the same density. Huddleston and Weaver utilized 41 and 100 keV gamma energies of ^{153}Gd for dual energy scattering [42]. The electron densities of solutions having different concentrations were calculated in their work to establish its use in bone mineral density calculation. Harding and Tischler [43] used this method by employing 100 and 160 kV X-ray sources to obtain the cross sectional images of ear. The photo electric component of the attenuation parameter was calculated from this experiment and it was used for correcting the higher attenuation at bones. The exposed skin dose was 20 mSv for 20 min in their experiment.

Coherent to Compton scattering ratio depends on the average atomic number and average mass number. Attenuation effects and error due to geometry can be minimized by considering the coherent to Compton ratio but with long measurement duration [44]. Puumalainen et al. [45] introduced this ratio method for bone mineral density determination. Later many researchers explored the utility of this technique for bone mineral density determination [28-31, 34]. This ratio method was used for the determination of fat content in tissues of samples taken from lever patients and normal humans through autopsy [46]. The corresponding radiation exposure calculated for in vivo measurements was 10 mrem. The coherent to Compton ratio method was also employed for determining the stable iodine content [33, 34] and body composition measurement [31]. ^{241}Am source is a common choice for the coherent to Compton ratio experiments owing to the high probability of coherent scattering at this energy. But some of the researchers reported the use of low energy X-ray sources [27, 30] and ^{153}Sm [28] for this purpose. Scanning duration can be reduced to one sixth by employing an X- ray source compared to that of high strength gamma source [30].

Line scan method is another technique introduced by Sharaf [47], in which attenuation of the test sample and the reference sample were neglected. From the line scan, along the depth attenuated scattered signals were plotted as a function of depth and slope of the same was obtained. This procedure was followed for different samples and a linear relation between slope and the density was obtained and further proved its ability to determine the variations in concentration. This method is highly useful in characterization of lung and body fluids especially because attenuation of the chest can be neglected.

The scattered gamma intensities are utilized by many researchers for obtaining the cross sectional images of chest, lung etc. [39, 41, 48-53]. Lale [22] utilized the gamma photons from a ^{192}Ir source and a NaI(Tl) scintillation detector to obtain thorax images of rabbit and guinea pigs. Poor image contrast, systematic errors and high image noise were reported due to the use of high energy gamma photons from ^{60}Co [50]. The requisite of high energy sources can be avoided for limited scan depths to obtain good image contrast [54]. Guzardi and Mey [51] utilized a ^{203}Hg source and a Compton camera to get two dimensional cross sectional chest images of simulated samples. They demonstrated the ability of this technique with real clinical results with 0.09 rem dose per each view. Guzardi and Licitra have reviewed various approaches of photon scattering imaging methods in medical field in detail [55].

1.3.2 Agricultural and food processing applications

Compton scattering technique can be utilized in both agricultural and food processing industry extensively, even though only fewer studies are reported in this field. Bull and Zwiggelaar [56] suggested some of the areas where Compton scattering based technique can be used for food inspection. Foreign body detection, presence of bone material in meat, voids in fruits, adulteration in milk and fat products etc. are some of the areas where this technique is feasible. Later this has been experimented in polystyrene spheres with voids to analyze the delectability of voids, contrast and signal to noise ratio [57].

Some preliminary studies were carried out to determine the soil density from the gamma backscattered intensity in 1960s [58, 59]. Density and water content estimation in soil are important to determine the goodness of the soil for the agriculture purpose. Balogun and Cruvinel [60] used Compton scatter imaging technique for determining the density and compactness of the soil. They used a ^{137}Cs source and NaI(Tl) detector for their study. The images obtained from scattered intensities showed the compactness of the soil. Later Cruvinel and Balogun [61] had estimated and constructed the image of the density and water content distribution in the soil using the same technique by ^{241}Am and ^{137}Cs sources. Yusuf Sahin et al. [62] have also proved this technique for determination of water content using ^{133}Ba source. The ability of Compton scatter technique for estimating the water content in soil had been evaluated using MCNP simulation [63].

1.3.3 Industrial applications.

The features of scattering method including single sided access, sensitivity and volume information attracted it to the industrial NDE applications. In many industries, online monitoring of quality and quantity of products, and the inspection of machineries are mandate. The ability of scattering method in determining the density and hence flaws, corrosion, intrusions etc. is making it applicable for this need. Even though Compton scattering imaging was developed initially for the applications in medical field, the high radiation dose was not favorable in its rapid development for clinical applications but in industrial applications this will not create any serious problem [64].

Gamma transmission technique is an established technique used in commercially available density gauges. Some of the industries where it has tested successfully are quoted in literature [9]. Backscattering technique is effective for determining the density of a sample from volume and can use as an alternate for transmission technique [65]. Density gauging in many industrial application like petroleum pipelines [66], atmospheric density [67] and concentration of the solutions [68,69] are some of the industrial applications found in literature using the quantitative Compton scattering technique. *In situ* measurement of aqueous solutions is useful in oceanography and solar pond research [68]. In powder metallurgy, scattering method was utilized to know the density of middle products just after compression since this density represents the quality of the final product [70, 71]. Due to the single sided access, possibility of scattering densitometry found attractive to examine the surface layers of large voluminous structures like bridges, structures and high ways. The density of the repaved layer of known thickness was measured and compared with the density of the layer measured before pavement for ensuring the quality [72]. Compton scattering measurement was performed on concrete samples for determination of density [73].

Since the scattered intensities can be related to the localized density, scattering technique can be used for discriminating materials with different densities within the same structure. Some researchers had utilized gamma scattering technique for locating voids and rebars in concrete [74-79]. The feasibility of Gamma scattering technique for detecting cracks, voids and delaminations in concrete structures was reported by Gautam et al. [73]. Tuzi and Sato described a method to locate rebar positions experimentally and theoretically [75, 76]. Design aspects of a system with optimized parameters like source energy, collimators and scattering angles are available in the detail work carried out by Hussein and Whynot [74].

Most of the workers utilized ^{137}Cs and ^{192}Ir sources for higher depth penetration. Similar flaw detection in aluminum blocks with steel inclusions and void creations were studied [80-86]. The voids of linear dimensions of the order of half of the source beam were detected using a proto type gamma ray scattering system with ^{137}Cs source and this proved the sensitivity of scattering NDE technique [82]. Anjos and co workers [83] used 2 Ci ^{137}Cs source and NaI(Tl) detector for detecting the defects in aluminum blocks and a defect as smaller as 1.6 mm was detected using the system. In their work, reasons for selecting a scattering angle of 90º i.e., for minimum measurement time and voxel size was justified with the help of experiments. Ho and Hussein [81] used the angular bounds obtained from the FWHM of the scattered photo peak as a measure to determine the size of voids in an aluminum block and calculated the size of the void from the extreme angles obtained from angular bounds, scattering angle and detector position. Achmad and Hussein discussed a non rotating method for determining the electron density of a point within an object using an X-ray source of 400 kV [84]. They calculated the electron density of wood, lucite and aluminum samples. All these reported studies highlighted the ability of scattering technique to determine non-destructively the flaws or inclusions inside a large structure.

In the aircraft industry, the detection of corrosion in aluminum parts and debonding of aluminum structures are essential for quality assurance and maintenance. The advantages of scattering technique in terms of detection from multiple layers, higher probability in composites and lack of requirement of surface preparation along with the other inherent features suffice for the corrosion detection of aircraft parts. Various sizes of voids were machined in a large steel plate and some of the holes were filled with FeO powder to represent corrosion and the whole system was kept hidden under an aluminum plate. A limited backscatter experiment was performed using ^{241}Am and ^{109}Cd sources and NaI(Tl) detector and the system could detect corrosion of 1 mm in size through an aluminum thin layer of 1-2 mm [87]. The defects in metal casting of jet engine turbine blades had been investigated using the scattering technique [21]. An artificially generated defect of size 0.1 mm thickness in an aluminum rubber interface was detected using an X-ray source [88]. A high resolution collimator in which multiple channels focused to the same volume was developed and employed in the experiment. This collimator design helped in reducing the scanning duration and improving the efficiency of the system. Jama et al. [89] found that photon scattering is useful to determine the adhesive thickness and debonding in composite and aluminum welds. Dunn and Yacout [90] demonstrated gamma scattering technique using ^{241}Am source for detecting the corrosion in aluminum sheets with simulated corrosion and voids. Their work proved the ability of the backscattering technique to detect the hidden or inaccessible flaws in samples similar of actual aircraft. An X-ray scanning method for detecting the hidden flaws especially in aircraft parts, with respect to a flawless sample was proposed and verified in an aircraft paint-thickness sample [91]. The quantification of corrosion using photon scattering studies was suggested [92, 93] and all these studies were carried out by varying the thickness of the specimen under study. A field study by employing a transportable gamma scattering system for locating the termite damaged railway sleepers is available in literature. The system consisted of two 12 Ci ^{137}Cs source and four NaI(Tl) scintillation detectors with corresponding data processing units [94]. The truck containing the above system was moved slowly above the track to provide an online testing. The ratio of coherent to Compton scattered intensity was used for finding out the alloy composition variation in aluminum foils [95].

Photon scattering technique is useful in thickness measurements for thick objects where charged particle gauging is less reliable and for thin objects where the photon transmission technique is ineffective [96]. The ability of gamma scattering technique to determine the thickness variations in pipe wall was reported by Puttmann in 1955 using a ^{60}Co source and NaI(Tl) detector [97]. A high speed Compton scatter system for imaging the pipe wall thickness was described by Xu et al. [98]. They used a wide aperture annular detector to quantitatively measure pipe wall thickness for empty and water filled pipes with or without heat insulation. Sharma et al. reported a gamma backscattering system with ^{137}Cs source to determine the pipe wall thickness, locating the defects in the wall under insulation and to identify the liquid flowing through the pipe [99]. A comparison of gamma, beta and X-ray backscatter technique to determine the thickness of glass container surface revealed the superiority of gamma scattering technique over beta scattering technique [100]. Later this method was used for steel plates where the FWHM of the counting rate curve is used to measure the thickness when the voxel is smaller than the sample thickness [101]. They suggested that when the sample is smaller than the voxel, the peak counting rate can be considered as an indication of the sample thickness. This method could detect the thickness upto 25 mm in steel with a precision of 5-10% using a 5 Ci ^{60}Co source. A relation between the scattered peak energy and tube wall thickness was established with an accuracy of 6% and this calibration was used to detect the surface defects in tube walls [102]. Recently scattering technique has been used for measuring the thickness of organic films [103], and oil crusts [104]. This technique is extremely useful to examine the last welded layer of a large thick sample [105]. Paraffin deposits in the pipe wall are serious issues facing in the petroleum industry, and a continuous monitoring system is required for this purpose without affecting the movement of the product. Lopes et al. experimentally proved that gamma scattering system is capable of identifying the paraffin deposits and the achieved minimum detectable limits of their system were 10% and 20% of the deposits with respect to total internal area using a well collimated and fan beam geometry respectively [106].

Photon scattering method was used for the determination of ash content in coal [107-109]. In archeology, this technique had been used effectively for determining the detachments and inhomogenities in the paintings and frescos and characterization of coins [110, 111]. Cesareo quantified the silver contents in coins through elastic and inelastic scattering of ^{241}Am source and compared the results with those obtained by gravimetric, gamma transmission and X-ray florescence techniques [109]. Dual Modality Densitometry (DMD) measurement is useful for the measurement of Gas Volume Fraction (GVF) in oil/ gas/ water flows [112-114] and measurements of water salinity [115]. Detailed critical reviews of various applications of X-ray or gamma scattering are available for further information regarding the developments in this field [21, 116-122].

Even though very limited studies were reported, gamma ray backscattering is also one of the possible tools for fluid level and interface determination. Due to the lower penetration of the back scattered gamma ray, its application is limited in thick metallic wall containers. Fluid level in containers with thermal insulation of 50 mm or steel wall thickness of 32 mm can be scanned using a ^{137}Cs source. But for higher thick walls or insulations, ^{60}Co source with proper collimation and shielding is required [64]. The application of gamma ray level indicators to determine the changeover of fuels at the delivery end of the pipelines for separate storing was reported in the literature [123]. This technique was employed in well logging to locate the interface between liquids in underground storage cavities containing various materials and to determine brine/product interface in underground cavities used for storing chemicals [64]. Gamma scattering technique was utilized for the level measurement systems in gravitational separators with appropriate simulation studies for optimized geometrical conditions [124].

Gamma scatter imaging was introduced by Lale [22] in medical field and later many researchers improved it. Similarly, this technique was used as an imaging tool in industry. An X-ray back scatter tomographic imaging system for radiologically thin or thick samples was demonstrated by Harding [19]. The superiority of scattering sensitivity over transmission was described in this work. This preliminary work led the way into the invention of Comscan system [118]. Holt and Cooper suggested that gamma ray scattering NDE technique could be considered as an alternate for radiography when the complexity due to size, shape and access prevents the latter [82]. In their work, two dimensional images of aluminum blocks with voids were obtained from the scattered intensities and the results showed the sensitivity of scattering technique. Landmine detection and hidden explosive scanning are two areas in security aspects where this technique is useful [125, 126]. A system known as Automatic Inspection Device for Explosive Charge in Shell (AIDECS) developed by IRT Corporation utilized multi-hole focusing collimators and had been used to examine the voids in mortar shells [21, 115]. This system could detect 1/16" voids and to measure a filler-case separation as small as 9 mils down in the base of the shell where the steel is thickest. The gamma ray back scattering system found useful in demilitarization of practice bombs [21]. This system could detect the presence of live cartridge surrounded by dust, sand and debris.

1.3.4 Comscan

Comscan is a commercial X-ray back scatter system [116-119] consisting of an X-ray source operated at 160 kV and two arrays of 11 Bismuth Germanate (BGO) detectors. The source beam is collimated using slit collimators and tungsten collimators are provided for the scattered beam. Various wedge type collimators employed for collimating the scattered beam according to the depth. The intensity of scattered intensity is correlated with the material density and the cross sectional images are constructed. The saturating depth of this system is 50 mm in plastic, 13 mm in aluminum and 1 mm in steel. The Comscan is efficient and fast for surface and near surface scanning. It is mainly used for detecting the defects in aircraft, automobile parts, fiber- reinforced plastic materials and car wheels due to their low atomic number. [95, 127]

1.3.5 Scattering imaging modes

1.3.5.1 Point by point mode

Radiation source is collimated to a fine narrow beam and a single detector which is also collimated is used for detecting the intensities. In this mode, scattered intensity from a single point or a small volume is collected at a time. Scattered intensities from different points can be collected by moving the sample along the three dimensional plane. In this method, if L is the width of the voxel the scanning time will be a function of L^{-7} and hence scanning time will be more for smaller voxels [117]. The measurement time can be reduced by increasing the source strength or voxel size.

1.3.5.2 Line by Line mode

Long measurement duration in point by point method was overcome by utilizing a line by line scanning mode. A narrow source beam is used to irradiate the sample and the scattered radiation across this photon path is detected using an array of detectors. Slit collimators or plane lamellas are used for collimating the scatter radiation so that each detector array collimates to its own region in primary beam [118]. The commercial system Comscan works in the line scanning geometry [116]. A pencil beam of gamma rays and an un-collimated Si(Li) detector are utilized to obtain the cross sectional images in medical applications [47, 48]. The detector detects the scattered signal from various points of the primary beam and the intensity and energy of these scattered intensities varies with distance and position.

1.3.5.3 Plane by plane mode

Two dimensional detectors like X-ray films are utilized to get the images of a plane at a time. This configuration is utilized for imaging the lung function and diseases [51, 54] and by employing a dynamic detector it can be used for obtaining moving images [118].

1.3.6 Estimation of multiple scattering and attenuation factor

The scattered signal is affected by two effects. The first one is due to the removal of photons from a specific spectral region due to the absorption in the sample and the second one is due to the generation of secondary radiation due to multiple interactions. Collimation, attenuation and multiple scattering effects slowed down the establishment of scattering technique as a NDE tool [82]. The estimation of these two factors for unambiguous interpretation of density and material properties made this scattering analysis complicated compared to transmission technique. The multiple scattering and self absorption factors have opposite effects on scattered intensity i.e., the multiple scattering enhances and self absorption decreases the scattered intensity [120]. Generally, when the optical thickness is less than unity both multiple scattering and attenuation contributions can be neglected [117].

1.3.6.1 Multiple scattering

Any photon which undergoes scattering more than once is considered as multiple scattered and the contribution of these multiply scattered photons in the scattered intensity will act as a source of error. Multiple scattering can be of any of the following categories: i) one scattering is followed another scattering, ii) multiple photoelectric interactions and iii) mixed scattering and photoelectric interactions [121]. The multiple scattering interactions depends upon the thickness of the sample and hence on the number of scattering centers in the interaction volume and photon attenuation co-efficient. Often the multiple scattering contributions are underestimated or overlooked because it is a complex and highly geometry dependent problem [128]. In a Compton scattering experiment, some reduction in multiple scattered components can be achieved by selecting a small energy width ΔE around the Compton peak and by using a high resolution detector and proper collimation. Selecting a small voxel is also an effective method for reducing the multiple scattering contributions. The multiple scattering can be reduced by selecting grid like lamellas in line by line scattering mode [42]. There are several methods reported for multiple scattering fraction calculations in literature. The extrapolation of Compton profiles to zero thickness is one of the methods available [129-132]. Reed and Eisenberger [128] used a linear dependence of multiple scattering on sample thickness and Weyrich [133] used a linearizing function which is linear for smaller thickness and saturates at higher thicknesses. Felsteiner and Pattison [131] used a linear extrapolation method based on a Monte Carlo calculation method. Another experimental method used was displaced beam technique [134] and it has been found that total scattered intensity is affected by multiple scattering contributions approximately by 10-15%. The analytical methods followed were based on some simplifications to handle the complexities of the multiple scattering. Hence Monte Carlo simulation was used by some of the researchers to completely account the real experimental situations [135-136]. Paramesh et al. [139] observed a saturation thickness up to which multiple scattering increased with sample thickness and then saturated as a function of atomic number of the target. The dependency of saturation thickness on scattering angle, collimator size, sample Z value and incident energy were studied later [140-141]. Felsteiner and Pattison [135] demonstrated that for low Z materials nearly 10% multiple scattering contributions existed and this was almost independent of incident energy. But in the case of high dense material a very low saturation thickness was observed for low energies and as a function of incident energy, the saturation thickness increased. A numerical method for estimation of multiple scattering was described by Das et al. [144]. Experimental evidences of multiple scattering as presence of double peaks in scattered peaks and detailed Monte Carlo calculations for calculating the multiple scatter fractions were discussed by Barnea et al. [145]. Higher multiple scatter fractions were observed for higher atomic number materials for higher scattering angle.

1.3.6.2 Attenuation correction

The amount of attenuation depends on the attributes of the regions encountered along the direction of the incident and scattered beams. This result in a nonlinear problem; while scattering is a linear process, attenuation is an exponential phenomenon. In Lale's [22] work, the attenuation effect was completely ignored by the use of a high-energy photon source from a linear accelerator, reducing to a linear imaging problem. Clarke et al. [146] utilized a ^{60}Co source and neglected the attenuation contribution. The attenuation problem was subsequently addressed by a number of researchers. Balogun and co workers [147] adopted a method of reconstructing the image in which prior knowledge of material's mass attenuation co-efficient is needed for attenuation correction. An integration method over a circle (the locus of the scattered points with same energy) was developed by Norton [148] and a modified and improved version of this was adopted by Jiajun Wang [149]. Arendtsz and Hussein [150, 151] proposed a solution for density reconstruction by solving a non linear equation which represents the scattering model using iterative method till convergence applicable to thin/ light objects. In the forward problem the scattered intensities were simulated from the prior knowledge of electron densities and in the inverse problem the image was reconstructed using an iterative method. This method was limited for thin/.light objects within the mean free path range. Later Arsenault and Hussein [152] suggested an algorithm using Compton scattering of X-ray fan beams for dense/.thick objects. Point to point scanning and reconstruction is another efficient method introduced by Battista [49] for scattering angle 135º. This scanning process required high radiation dose compared to the CT [149]. Prettyman et al. [153] used an independent CT data for obtaining the attenuation factors and scatter data for obtaining density. El Khetabi et al. [154-155] avoided the rotation of the sample by employing multi detectors and by taking the ratio of scattered intensities which are having same incident path length and scattering point and many more works on scattering image technique can be found elsewhere [156].

1.4 Motivation

Even though the photon scattering technique is having many advantages, still less popular due to the complications in quantification arising from attenuation and multiple scattering effects, requirement of longer scanning time and proper collimation. Hence proper accounting for attenuation and multiple scattering will make this technique more effective in field studies. Most of the algorithms available for three dimensional image reconstruction require either multiple number of detectors, fan beam geometry or dual energy sources. These requirements make the system costly and bulky. Thus an algorithm using a collimated source and single detector is required for the development of a portable device. Comparison with transmission technique is required for choosing either of the method for better accuracy and a comparison of this sort is not widely studied. A study of Compton scattering incorporating multiple scattering, self absorption estimation and density reconstruction would be highly beneficial for NDE characterization and assessment of thick, high dense structural materials.

1.5 Objectives

The main objectives of the present work reported in this thesis are as follows:

- To develop semi empirical methods for correcting multiple scattering and attenuation contributions
- To develop an algorithm for three dimensional density reconstruction using a single source and detector
- To provide an intercomparison of scattering and transmission technique on sensitivity and accuracy
- A gamma scattering gauge for corrosion detection in non uniformly corroded sample
- A gamma scattering gauge for fluid-fluid interface level detection
- Gamma scattering density gauge for detecting smaller variations in concentration and density of fluids
- A gamma scattering technique for detecting the voids and moisture content in structural concrete material

1.6 Overview of the Thesis

Chapter 1 gives a brief introduction to ionizing radiation based and other main NDE techniques and interaction of radiation with matter. Literature survey on photon scattering studies and applications, motivation and objectives are described in this chapter. ***Chapter 2*** describes the experimental set up, theoretical and Monte Carlo calculations used in the present work. Gamma scattering method for detection and quantification of corrosion in Mild Steel (MS) plate is discussed in ***chapter 3***. An intercomparison of results with transmission and radiography techniques are also provided. ***Chapter 4*** demonstrates the utility of scattering method in determining the fluid-fluid and fluid-air interface levels and for quantifying the density or concentration of the solutions which are having closer attenuation parameters. A unique nonlinear relation is used to explain the dependency of scattered intensity per unit volume on sample radius. In ***chapter 5*** gamma scattering method for detecting the defects and moisture content in the concrete ($\approx$ 2.24 g/cm^3) blocks are discussed. An improved algorithm based on the point to point scanning method prescribed by Battista et.al [49] is used for the attenuation correction and image reconstruction. ***Chapter 6*** summarizes the major research findings, improvements and recommendations for future work.

References

1. "What is NDE?", American Society of Non Destructive testing, (2000) http://www.asnt.org/whatndt/
2. B. Raj, B. Venkatraman, 12th A-PCNDT 2006-Asia Pacific Conference on NDT, Auckland, New Zealand, (2006) 1-11

3. Heiller, C., Handbook of Nondestructive Evaluation, McGraw-Hill
4. Hussein, E.M.A., Hand book on Radiation probing and imaging, Vol.1, First edition, Springer, (2003)
5. Raj, B., Venkatraman, B., Practical Radiography, Alpha Science Int'l Ltd, (2004)
6. "Liquid Penetrant and Magnetic Particle Testing at Level 2", Training course series no.11, IAEA,(2000), http://www.pub.iaea.org/MTCD/publications/PDF/TCS-11.pdf
7. Johansen, G.A., Jackson, P., "Radioisotope Gauges for Industrial Process Measurements", Wiley, England, (2004)
8. Libby, W.F., Annual Review on Nuclear Science, 11 (1961), 461-482
9. "Industry Benefits from Radioisotopes", IAEA publication, http://www.iaea.org/Publications/Magazines/Bulletin/Bull063/06305002630.pdf
10. Evans, R.D., The Atomic Nucleus, McGraw Hill, (1955)
11. Cember, H., Johnson, T.E., Introduction to Health Physics, Fourth Edition, McGraw Hill, (2008)
12. Hubbell, J.H., Veigele, W.J., Briggs, E.A., Brown, R.T., Cromer, D.T., Howerton, R.J., J. Phys. Chem. Ref. Data, 4 (1975), 471-538
13. Perrin, F., Comptes Rendus, 197 (1933), 1100
14. Speller, R.D., Horrocks, J.A., Phys. Med. Biol., 36 (1991), 1-6
15. Williams, B.G., Compton scattering, McGraw Hill, (1977)
16. Cooper, M.J., Rep. Prog. Phys., 48 (1985), 415-481
17. Ghaleb, A.M., Mohammed, F.M., sahariya, J., Sharma, M., Ahuja, B.L., Physica B, 412 (2013), 106-111
18. Bhamu, K.C., Ahuja, B.L., Appl. Radiat. Isot., 70 (2012), 942-945
19. Bhamu, K.C., Sahariya, J., Ahuja, B.L., J. Phys. Chem. Solids, (2013), http://dx.doi.org/10.1016/j.jpcs.2013.01.020
20. Harding, G., IEEE Trans. Nucl. Sci., NS-29 (1982), 1259-1265
21. Cesareo, R., Brunetti, A., Golosio, B., Lopes, R.T., Barroso, R.C., Castellano, A., Quarta, S., Nucl. Instrum. Meth. A, 525 (2004), 336-341

22. Stokes, J.A., Alvar, K.R., Corey, R.L., Costello, D.G., John, J., Kocimski, S., Lurie, N.A., Thayer, D.D., Trippe, A.P., Young, J.C., Nucl. Instrum. Methods, 193 (1982), 261-267
23. Lale, P.G., Phys. Med. Biol., 4 (1959), 159-167
24. Clarke, R.L., Van Dyk, G., Phys. Med. Biol., 18 (1973), 532-539
25. Garnett, E.S., Kennett, T.J., Kenyon, D.B., Webber, C.E., Radiology, 106 (1973), 209-212
26. Webber, C.E., Kennet, T.J., Phys. Med. Biol., 21 (1976), 760-769
27. Olkkonen, H., Karjalainen, P., Brit. J. Radiol., 48 (1975), 594-597
28. Puumalainen, P., Uimarihuhta, A., Olkkonen, H., Alhava, E.M., Phys. Med. Biol., 27 (1982), 425-429
29. Kerr, S.A., Kouris, K., Webber, C.E., Kennet, T.J., Phys. Med. Biol., 25 (1980), 1037-1047
30. Shukla, S.S., Leitcher, I., Karellas, A., Craven, J.D., Greenfield, M.A., Radiology, 158 (1986), 695-697
31. Webster, D.J., Lillicrap, S.C., Phys. Med. Biol., 30 (1985), 531-539
32. Morgan, H.M., Shakeshaft, J.T., Lillicrap, S.C., Appl. Radiat. Isot., 49 (1998), 555-557
33. Morgan, H.M., Shakeshaft, J.T., Lillicrap, S.C., Brit. J. Radiol., 72 (1999), 1069-1072
34. Puumalainen, P., Sikanen, P., Olkkonen, H., Nucl. Instrum. Methods, 163 (1979), 261-263
35. Sharma, A., Singh, M., Singh, B., Sandhu, B.S., J. Med. Phys., 34 (2009), 182-187
36. Shakeshaft, J., Morgan, H.M., Lillicrap, S.C., Phys. Med. Biol., 42 (1997), 1403-1413
37. Al-Bahiri, J.S., Spyrou, N.M., Appl. Radiat. Isot., 49 (1998), 1677-1684
38. Elshemey, W.M., Elsayed, A.A., El-Lakkani, A., Phys. Med. Biol., 44 (1999), 2907-2915
39. Garnett, E.S., Webber, C.E., Coates, G., Cockshott, W.P., Nahmias, C., Lassen, N., CMA Journal, 116 (1977), 153-154

40. Pistolesi, M., Solfanelli, S., Guzzardi, R., Mey, M., Giuntini, C., J. Nucl. Med., 19 (1978), 94-97
41. Wolf, E.A., Munro, T.R., Int. J. Appl. Radiat. Isot., 36 (1985), 97-102
42. Huddleston, A.L., Weaver, J.B., Int. J. Appl. Radiat. Isot., 34 (1983), 997-1002
43. Harding, G., Tischler, R., Phys. Med. Biol., 31 (1986), 477-489
44. Tothill, P., Phys. Med. Biol., 34 (1989), 543-572
45. Puumalainen, P., Uimarihuhta, A., Alhava, E.M., Olkkonen, H., Radiology, 120 (1976) 723-724
46. Puumalainen, P., Olkkonen, H., Sikanen, P., Int. J. Appl. Radiat. Isot., 28 (1977), 785-787
47. Sharaf, J.M., Appl. Radiat. Isot., 54 (2001), 801-809
48. Farmer, F.T., Collins, M.P., Phys. Med. Biol., 16 (1971), 577-586
49. Farmer, F.T., Collins, M.P., Phys. Med. Biol., 19 (1974), 808-818
50. Battista, J.J., Santon, L.W., Bronskill, M.J., Phys. Med. Biol., 22 (1977), 229-244
51. Battista, J.J., Bronskill, M.J., Phys. Med. Biol., 26 (1981), 81-99
52. Guzzardi, R., Mey, M., Phys. Med. Biol., 26 (1981), 155-161
53. Lenti, M., Nucl. Instrum. Meth. A, 588 (2008), 457-462
54. Harding, G., Tischler, R., Phys. Med. Biol., 31 (1986), 477-489
55. Guzardi, R., Licitra, G., CRC Crit. Rev. Bio. Eng., 15 (1988), 237-268
56. Bull, C.R., Zwiggelaar, R., J. Agr. Eng. Res., 68 (1997), 77-87
57. McFarlane, N.J.B., Bull, C.R., Tillett, R.D., Speller, R.D., Royle, G.J., Johnson, K.R.A., J. Agr. Eng. Res., 75 (2000), 265-274
58. Uemura, T., Jpn. J. Appl. Phys., 4 (1965), 667-676
59. Taylor, D., Kansara, M., Nucl. Instrum. Methods, 59 (1968). 305-308
60. Balogun, F.A., Cruvinel, P.E., Nucl. Instrum. Meth. A, 505 (2003), 502-507
61. Cruvinel, P.E., Balogun, F.A., Eng.Agric.Jaboticabal, 26 (2006), 151-160
62. Sahin, Y., Un, A., Demir, D., Ozgul, M., Fidan, M., X-ray Spectrom.,
63. Avelar, F., Carneiro, C.J.G., Silva, M.R.S., Penna, R., Porto, P.A.A., International Nuclear Atlantic Conference-INAC 2007
64. Holt, R.S., Endeavour, 9 (1985), 97-105

65. Edmonds, E.A., “Radiation scattering techniques” in : Charlton, J.S., (Ed), Radioisotope Techniques for Problem solving in Industrial Process, Glasgow, Leonard Hill, (1986), 247-268
66. Gouveia, M.A.G., Lopes, R.T., de Jesus, E.F.O., Camerini, C.S., Nucl. Instrum. Meth. A, 505 (2003), 540-543
67. Gardner, R.P., Whitaker, D.R., Nucl. Eng. Des., 7 (1968), 13-28
68. Gayer, A., Bukshpan, S., Kedem, D., Nucl. Instrum. Methods, 192 (1982), 619-621
69. Guang, L., Shang-Qi, Z., Zhong, H., Shuang-Kou, C., Chinese J. Chem., 25 (2007), 164-167
70. Zhu, P., Peix, G., Babot, D., Muller, J., NDT & E Int., 28 (1995), 3-7
71. Zhu, P., Duvauchelle, P., Peix, G., Babot, D., Meas. Sci. Technol., 7 (1996), 281-286
72. Dunn, W.L., Hutchinson, J.E., Int. J. Appl. Radiat. Isot., 33 (1982), 563-567
73. Adil, N., Brit. J. Nondestr. Test., 19 (1977), 72-77
74. Gautam, S.R., Hopkins, F.F., Klinkseik, R., Morgan, I.L., IEEE Trans. Nucl. Sci., NS-30 (1983), 1680-1684
75. Hussein, E.M.A., Whynot, T.M., Nucl. Instrum. Meth. A, 283 (1989), 100-106
76. Tuzi, S., Sato, O., Appl. Radiat. Isot., 41 (1990), 1013-1018
77. Tuzi, S., Sato, O., Appl. Radiat. Isot., 44 (1993), 1279-1284
78. Chankow, N., Pojchanachai, S., Nucl. Instrum. Meth. B, 213 (2005), 418-421
79. Sharma, A., Sandhu, B.S., Singh, B., J. Korean Phys. Soc., 59 (2011), 2880-2883
80. Jama, H.A., Hussein, E.M.A., Appl. Radiat. Isot., 50 (1999), 331-342
81. Mullin, S.K., Hussein, E.M.A., Nucl. Instrum. Meth. A., 353 (1994), 663-667
82. Ho, A.C., Hussein, E.M.A., Appl. Radiat. Isot., 53 (2000), 541-546
83. Holt, R.S., Cooper, M.J., NDT Int., 20 (1987), 161-165
84. Anjos, M.J., Lopes, R.T., Borges, J.C., Nucl. Instrum. Meth. A, 280 (1989), 535-538
85. Achmad, B., Hussein, E.M.A., Appl. Radiat. Isot., 60 (2004), 805-814
86. Banerjee, K., Dunn, W.L., Appl. Radiat. Isot., 65 (2007), 176-182

87. Yacout, A.M., Van Haaren, M.H., Dunn, W.L., Appl. Radiat. Isot., 48 (1997), 1313-1320
88. Duvauchelle, P., P. Girier, P., Peix, G., Appl. Radiat. Isot., 41 (1990), 199-205
89. Jama, H.A., Hussein, E.M.A., Lee-Sullivan, P., NDT & E Int., 31 (1998), 99-103
90. Dunn, W.L., Yacout, A.M., Appl. Radiat. Isot., 53 (2000), 625-632
91. Dunn, W.L., Appl. Radiat. Isot., 61 (2004), 1217-1225
92. Bridge, B., Gunnell, J.M., Imrie, D.C., Olson, N.J., Nondest. Test. Commun., 2 (1986), 103-113
93. Ong, P.S., Patel, V., Balasubramanyan, A., J. Nondestruct. Eval., 16 (1997), 135-146
94. Fookes, R.A., Watt, J.S., Seatonberry, B.W., Davison, A., Greig, R.A., Lowe, H.W.G., Abbott, A.C., Int. J. Appl. Radiat. Isot., 29 (1978), 721-728
95. Cooper, M.J., Rollason, A.J., Tuxworth, R.W., Journal of Physics E : Scientific Instruments, 15 (1982), 568-572
96. Hussein, E.M.A., Hand book on Radiation probing and imaging, Vol.2 ,First edition, Springer, (2003).
97. Putman, J.L., Jefferson, S., Cameron, J.F., Kerry, J.P., Pulsford, E.W., J. Sci. Instrum., 32 (1955), 394-398
98. Xu. X., Gould, R., Khan, S., Klevans, E.H., Kenney, E.S., Nucl. Instrum. Meth. A, 353 (1994) 334-337
99. Sharma, A., Sandhu, B.S., Singh, B., Appl. Radiat. Isot., 68 (2010), 2181-2188
100. Mohammadi, H., Int. J. Appl. Sci., 32 (1981), 524-526
101. Asa’d, Z., Asghar, M., Imrie, D.C., Meas. Sci. Technol., 8 (1977), 377-385
102. Silva, I.L.M., Lopes, R.T., de Jesus, E.F.O., Nucl. Instrum. Meth. A,422 (1999), 957-963
103. Kim, J.Y., Choi, Y.S., Park, Y.J., Song, K., Jung, S.H., Hussein, E.M.A., Appl. Radiat. Isot., 69 (2011), 1241-1245
104. Mamatrishat, M., Abuliemu, A., Jie, Ding., Shiheng, W., arXiv preprint arXiv:0803.2086 (2008)
105. Stepanov, V.E., Ivanov, O.P., Potapov, V.N., Sudarkin, A.N., Urutskoev, L.I., Nucl. Instrum. Meth. A, 422 (1999), 724-728

106. Lopes, R.T., Valentine, C.M., de Jesus, E.F.O., Camerini, C.S., Appl. Radiat. Isot., 48 (1997), 10-12
107. Charbucinski, J., Mathew, P.J., Nucl. Instrum. Methods, 193 (1982) 269-273
108. Boyce, I.S., Int. J. Appl. Radiat. Isot., 34 (1983), 45-54
109. Arikan, P., Zararsiz, A., Kirmaz, R., Efe, N., Nucl. Instrum. Meth. B, 95 (1995) 82-86
110. Cesareo, R., Nucl Instrum Methods, 179 (1981), 545-549
111. Castellano, A., Cesareo, R., Buccolieri, G., Donativi, M., Palama, F., Quarta, S., De Nunzio, G., Brunetti, A., Marabelli, M., Santamaria, U., Nucl. Instrum. Meth. B, 234 (2005), 548-554
112. Tjugum, S.A., Johansen, G.A., Holstad, M.B., Radiat. Phys. Chem., 61 (2001), 797-798
113. Tjugum, S.A., Frieling, J., Johansen, G.A., Nucl. Instrum. Meth. B, 197 (2002), 301-309
114. Tjugum, S.A., Johansen, G.A., Holstad, M.B., Meas. Sci. Technol., 14 (2003), 1777-1782
115. Johansen, G.A., Jackson, P., Appl. Radiat. Isot., 53 (2000), 595-601
116. Holt, R.S., Cooper, M.J., Jackson, D.F., Nucl. Instrum. Methods, 221 (1984), 98-104
117. Harding, G., Kosanetzky, J., Nucl. Instrum. Meth. A, 280 (1989), 517-528
118. Harding, G., Radiat. Phys. Chem., 50 (1997), 91-111
119. Harding, G., Harding, E., Appl. Radiat. Isot., 68 (2010), 993-1005
120. Hussein, E.M.A, Waller, E.J., Radiat. Meas., 29 (1998), 581-591
121. Cesareo, R., Hanson, A.L., Gigante, G.E., Pedraza, L.J., Mahtaboally, S.Q.G., Phys. Rep., 213 (1992), 117-178
122. Lawson, L.R., Mater. Eval., 60 (2002), 1295-1316
123. Jefferson, S., “Radioisotopes: A new tool for industry”, George newness limited, London, (1957).
124. Holstad, M.B., Johanson, G.A., Jackson, P., Eidsnes, K.S., IEEE Sens. J., 5 (2005), 175-182
125. Harding, G., Radiat. Phys. Chem., 71 (2004), 869-881

126. Hussein, E.M.A., Desrosiers, M., Waller, E.J., Radiat. Phys. Chem., 73 (2005), 7-19
127. Sponder, L., Technical Report 34, (1993), Department of Defence, Defence Science and Technology Organisation, Aeronautical research Laboratory, Australia
128. Kennett, T.J., Webber, C.E., Phys. Med. Biol., 21 (1976), 770-780
129. Reed, W.A., Eisenberger, P., Phys. Rev. B, 6 (1976), 4596-4604
130. Tanner, A.C., Epstein, I.R., J. Chem. Phys., 61 (1974), 4251-4257
131. Shivaramu, Gopal, S., Sanjeevaiah, B., Nucl. Instrum. Methods, 140 (1977), 529-532
132. Felsteiner, J., Pattison, P., Nucl. Instrum. Methods, 173 (1980), 323-327
133. Weyrich, W., Ber. Bunsen. Phys. Chem., 79 (1975), 1086-1095
134. Philips, W.C., Chin, A.K., Philos. Mag., 27 (1973), 87-93
135. Felsteiner, J., Pattison, P., Cooper, M., Philos. Mag., 30 (1974), 537-548
136. Felsteiner, J., Pattison, P., Nucl. Instrum. Methods, 124 (1975), 449-453
137. Tanner, A.C., Epstein, I.R., Phys. Rev. A, 14 (1976), 328-340
138. Fernandez, J.E., Badiali, M., Guidetti, A., Scot, V., Nucl. Instrum. Meth. A, 580 (2007), 77-80
139. Paramesh, L., Venkataramaiah, P., Gopala, K., Sanjeeviah, H., Nucl. Instrum. Methods, 206 (1983), 327-330
140. Singh, M., Singh, G., Sandhu, B.S., Singh, B., Appl. Radiat. Isot., 64 (2006), 373-378
141. Singh, M., Singh, G., Sandhu, B.S., Singh, B., Radiat. Meas., 42 (2007), 420-427
142. Singh, M., Singh, G., Singh, B., Sandhu, B.S., Nucl. Instrum. Meth. A, 580 (2007), 54-57
143. Singh, G., Singh, M., Sandhu, B.S., Singh, B., Appl. Radiat. Isot., 66 (2008), 1151-1159
144. Das. G., Panda, B.K., Mahapatra, D.P., Padhi, H.C., Physica Stata Solidi(b), 149 (1988), 355-362
145. Barnea, G., Dick, C.E., Ginzburg, A., Navon, E., Seltzer, S.M., NDT & E Int., 28 (1995), 155-162
146. Clarke, R.L., Milne, E.N., Van Dyk, G., Invest. Radiol., 11 (1976), 225-235

147. Balogun, F.A., Spyrou, N.M., Nucl. Instrum. Meth. B, 83 (1993), 533-538
148. Norton, S.J., J. Appl. Phys., 76 (1994), 2007-2015
149. Wang, J., Chi, Z., Wang,Y., J. Appl. Phy., 86 (1999), 1693-1698
150. Arendtsz, N.V., Hussein, E.M.A., IEEE Trans. Nucl. Sci., 42 (1995), 2155-2165
151. Arendtsz, N.V., Hussein, E.M.A., IEEE Trans. Nucl. Sci., 42 (1995), 2166-2172
152. Arsenault, P.J., Hussein, E.M.A., IEEE Trans. Nucl. Sci., 53 (2006), 1622-1633
153. Prettyman, T.H., Gardner, R.P., Russ, J.C., Varghese, K., Appl. Radiat. Isot., 44 (1993), 1327-1341
154. Khettabi, F.El., Hussein, E.M.A., Inverse Probl., 19 (2003), 447-495
155. Khettabi, F.El., Hussein, E.M.A., Jama, H.A., IEEE Trans. Nucl. Sci., 51 (2004), 641-647
156. Hussein, E.M.A., Nucl. Instrum. Meth. B, 263 (2007), 27-31

Chapter II Experimental set-up, procedure and Monte Carlo methods

2.1 Introduction

The experimental set-up and the theoretical methods used for this study are described in this chapter. The details regarding the automation of the instrument, data acquisition and analysis of scattered intensity are discussed. Monte Carlo N Particle (MCNP) [1] code is utilized in this work as a supportive tool for the experimental studies. The important functions of MCNP employed in the simulations are described. In the scattering experiments, intersection of source and detector field of view is known as voxel and it decides the spatial resolution of the technique. When diverging source and detector beams are considered, the intersection of two cones inclined at an angle is the resultant voxel. The analytical method followed for calculating the voxel size is also described in this chapter.

2.2 Experimental set-up

The experimental set-up used for this study is an indigenously designed automated PC controlled scanning system consisting of CNC controlled 6-axis source detector system and 4-axis job positioning system, a High Purity Germanium (HPGe) detector and radioactive sources (^{137}Cs and ^{241}Am). The schematic diagram and photograph of the experimental set-up are shown in figures 2.1 and 2.2 respectively. Shielded sources and detector, sample holder and the job positioning system for the movement of sample are marked in the photograph (figure 2.2). This set-up can be used for scattering and transmission experiments simultaneously. The details of the various components of experimental set-up are described below.

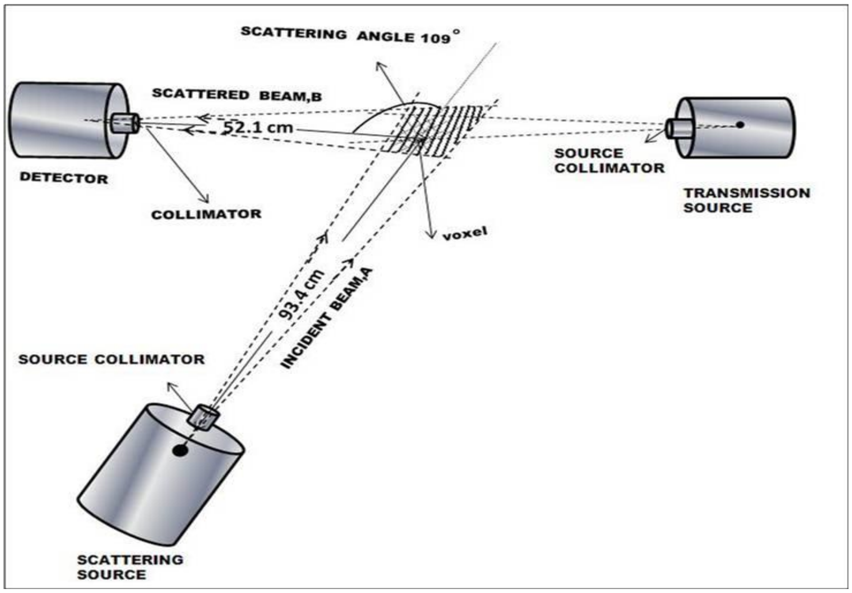
SCATTERING ANGLE 109°
SCATTERED BEAM,B
52.1 cm
DETECTOR
COLLIMATOR
SOURCE COLLIMATOR
TRANSMISSION SOURCE
voxel
93.4 cm
INCIDENT BEAM,A
SOURCE COLLIMATOR
SCATTERING SOURCE

Figure 2.1 Schematic of the experimental set-up

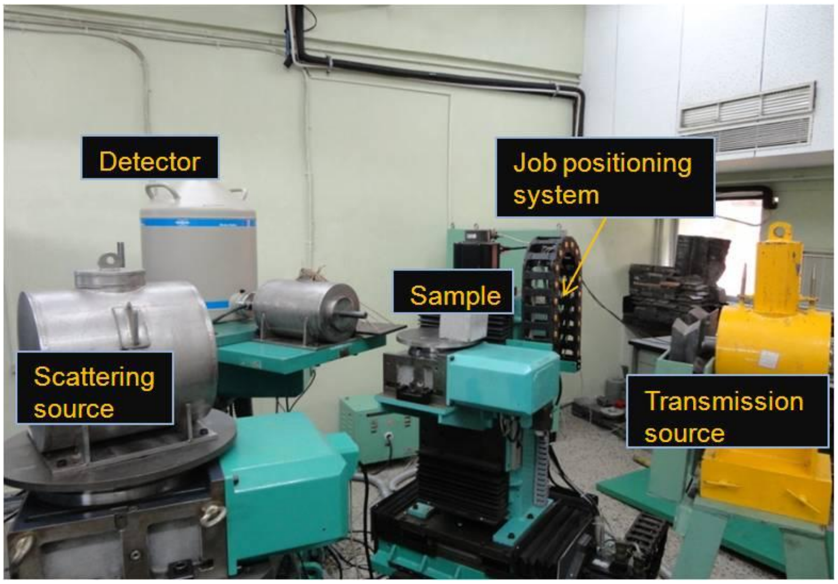
Detector
Job positioning system
Sample
Scattering source
Transmission source

Figure 2.2 Experimental set-up

2.2.1 Radioactive sources

The first step in photon transmission or scattering processes is photon incidence on target material. For this purpose a 'photon source' is required which can provide high intense and well defined energy photons. Generally X-ray systems are used as the source for photons in which energy will be in the range of few keV. The penetration power of X-rays is less compared to that of gamma rays. Thus the sample thickness that can be analyzed or the scanning depth is limited by this fact. Bremsstrahlung photon beams (3-6 MeV) from small electron Linear Accelerator (LINAC) is used for greater penetrability and high intensity. These unique features make it a very desirable photon source for industrial applications. However, the installation and maintenance cost of LINAC system makes it less preferable. Radioactive sources are other choice for gamma photons. The gamma rays from radioactive isotopes produce an energy spectrum that has distinct emission energy peaks, thus providing well-defined photon energies that enable easier analysis of the measured signal. Moreover, gamma ray isotopic sources are portable, self-contained, self-energizing, small in size and usable in hostile environments. The other advantages of these radioactive sources are relatively long half-life, high specific activity and simple means of production. The disadvantage of using the radioactive isotopes is the low counting rate compared to the high counting rate of X-rays and LINAC. It is preferable and very convenient to use ^{137}Cs radioactive source which emits photons of energy 661.6 keV, within the energy range where the Compton process dominates. The ^{60}Co (1.17 and 1.33 MeV) can also be used for higher penetration but it is desirable to use radioisotopes that emit mostly at a single energy. Otherwise, detector may not be able to distinguish between scattered energies of the original photons with energies very close to each other. This will result in ambiguity and complexness in the variation of count rate with energy and density.

^{137}Cs radio isotope which emits gamma photon of 661.6 keV is a fission product and it decays by beta mode to ^{137}Ba with a half life of 30.2 years. The decay scheme of the ^{137}Cs is depicted below in figure 2.3 and sources of activity 4.2 Ci and 4.3 mCi are employed for scattering and transmission experiments respectively. This particular source is selected because of its mono energetic nature, long half-life and due to the predominant cross section for Compton process in its energy range. Comparably lower strength source is used for transmission experiments to reduce the continuum background in scattered Pulse Height Spectra (PHS) when transmission and scattering experiments are performed simultaneously.

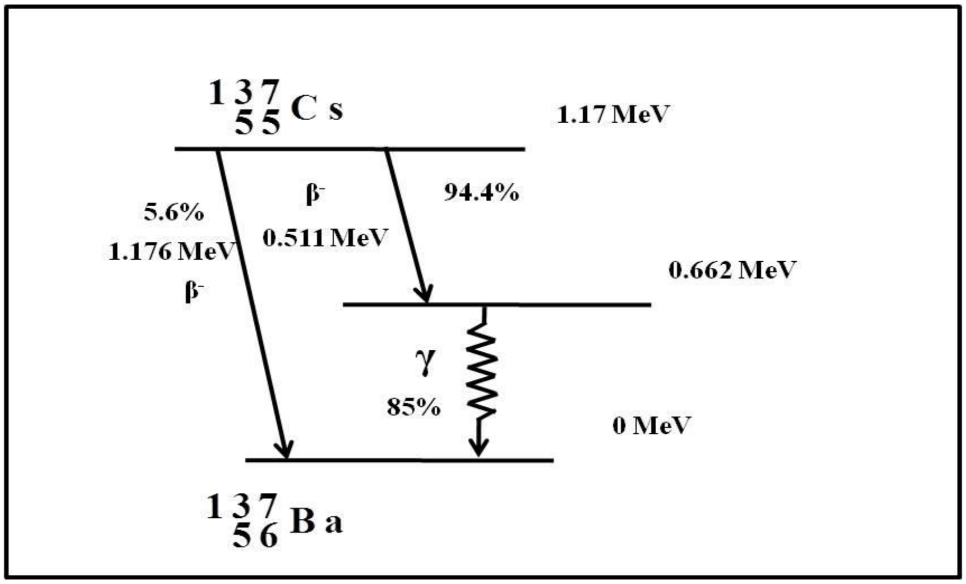

Figure 2.3 Decay scheme of ^{137}Cs

^{241}Am isotope decays by alpha decay to ^{237}Np with a half-life of 432.7 years and the predominant gamma energy following the alpha decay is 59.54 keV. This isotope has found applications in many commercial uses including fluid density gauges, thickness gauges and medical diagnostic devices and a 10 mCi source is used for conducting the transmission experiment. Due to the low penetration capability of 59.54 keV gamma photons from ^{241}Am, its usage is limited for high dense, thick or hidden inside high density background materials. The decay scheme of ^{241}Am source is shown in figure 2.4

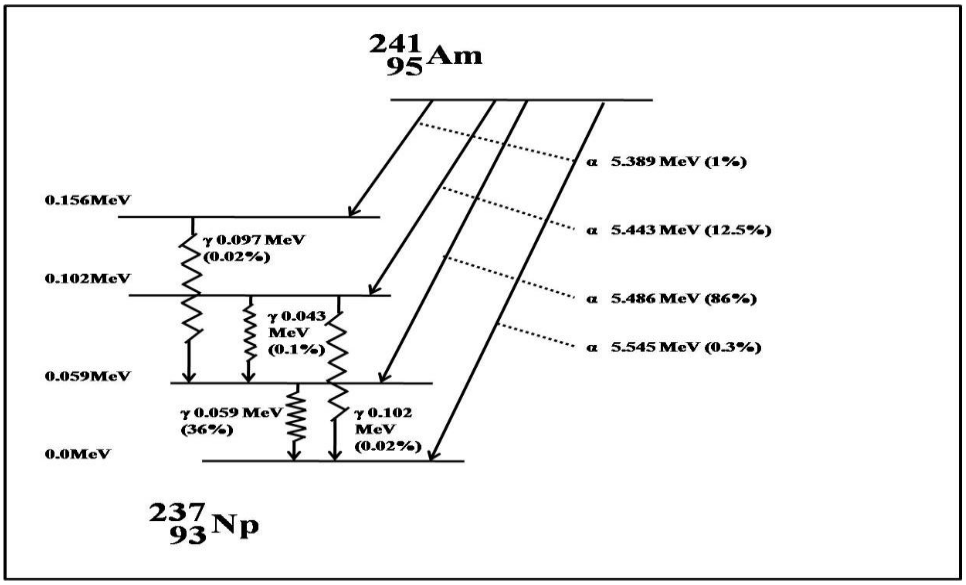
$^{241}_{95}$Am
α 5.389 MeV (1%)
α 5.443 MeV (12.5%)
α 5.486 MeV (86%)
α 5.545 MeV (0.3%)
0.156MeV
γ 0.097 MeV (0.02%)
0.102MeV
γ 0.043 MeV (0.1%)
0.059MeV
γ 0.059 MeV (36%)
γ 0.102 MeV (0.02%)
0.0MeV
$^{237}_{93}$Np

Figure 2.4 Decay scheme of ^{241}Am

2.2.2 Detector and electronics

A pulse height analysis system includes the detector and the corresponding processing electronics units. The block diagram of the detector system along with other electronic components is shown in figure 2.5. A detail description about each of these components is provided.

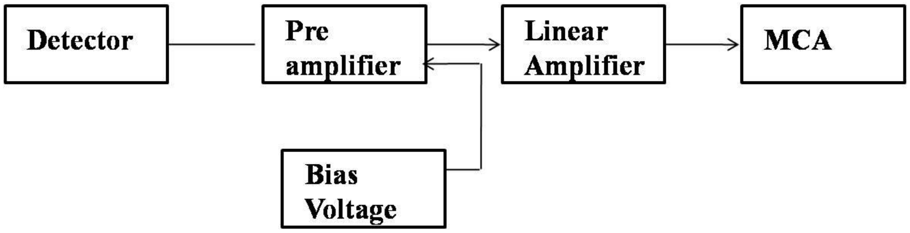
Detector
Pre amplifier
Linear Amplifier
MCA
Bias Voltage

Figure 2.5 Block diagram of detector system with electronics

2.2.2.1 Detector

Commonly used radiation detectors are ionization chambers, proportional counters, Geiger Muller (GM) counters, scintillation detectors and semiconductor detectors. Ionization detectors are the first electrical devices used for detecting radiation [2]. Ionization produced by charged particles is the basis of detection in ionization chamber, proportional counter and GM counter and the efficiency of detection for gamma rays is relatively poor. Detection of radiation based on the scintillation produced by them in crystals like NaI is the working principle of scintillation detectors. Electron-hole pair generation due to the ionizing radiation in a depleted layer of p-n junction semiconductor is utilized for the detection of radiation in semiconductor detectors. Energy required for producing an e-h pair is 2.96 and 3.62 eV for Ge and Si respectively which is very small compared to the 100 eV for photoelectron generation in scintillation counter and 30 eV for ion pairs in gas chamber [3]. More e-h pairs are produced for the incident energy in semiconductor detectors and hence high resolution is achieved compared to scintillation detectors. Energy resolution is the ability of a detector to detect and differentiate two closely lying energies and it is nearly 0.15% and 6% for HPGe and NaI detectors respectively at 1.33 MeV gamma energy. High resolution is a requisite for detectors employed in Compton scattering applications and this reduces the multiple scatter contribution in the scattered Pulse Height Spectra (PHS).

A 50% efficiency high resolution Bruker Baltic make HPGe p-type co-axial detector is used in the present experiment. A liquid nitrogen dewar vessel of capacity 30 L is attached to the detector. Gamma ray energy range of this detector is 40-10000 keV. All cooled parts of the detector unit are covered with multi layer thermal insulation in order to reduce the heat leakage. The cross sectional image of the crystal is given in figure.2.6. The crystal size of detector is 6.6 cm in diameter and 6.6 cm in length and the end cap is of thickness 0.6 mm. The detector resolution at 661.6 keV is found to be 0.21%.

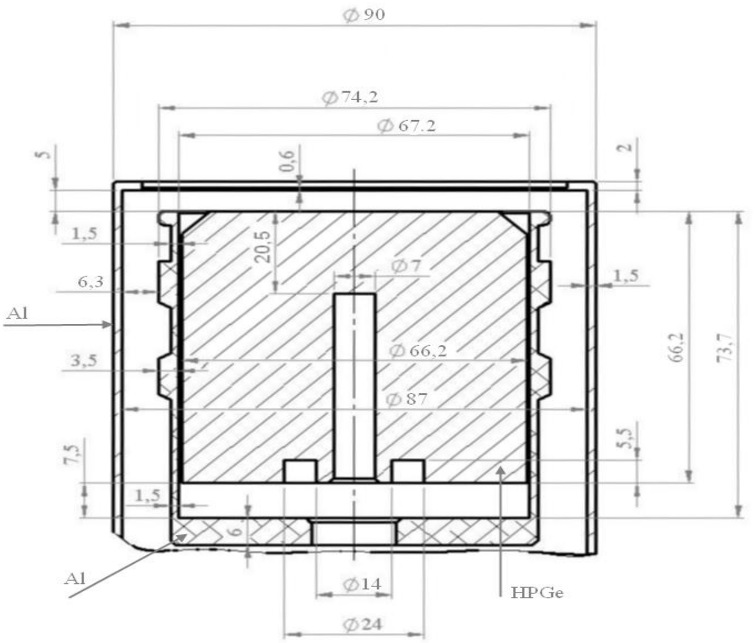

Figure 2.6 Cross sectional image of 50% efficiency detector

2.2.2.2 Preamplifier

A preamplifier is integrally attached to the detector as close as possible and the main function of preamplifier is to provide impedance match between the high impedance of the detector with the low impedance of the amplifier. In addition to this, bias voltage is applied to the detector through the preamplifier. Preamplifiers can be of charge sensitive or voltage sensitive type and in voltage sensitive configuration, the amplitude of the output pulse will be proportional to the amplitude of the input pulse. But for semiconductor detectors charge sensitive preamplifiers are used and in this configuration the output voltage is proportional to the integrated charge supplied to the input terminals. The incoming charge is collected in a capacitor and discharged through a resistance feedback network. This makes the output of preamplifier a linear tail pulse with large decay time and help to facilitate the full collection of charge from detectors. In the present experimental set-up, detector and input stage of preamplifier are placed inside the vacuum chamber and cooled to liquid nitrogen temperature. Warm part of preamplifier is placed outside of the chamber with connecting wires. The low voltage +/- 12 V is fed to preamplifier/ detector during operation. The pre amplifier used is having an output signal voltage rise time less than 0.15 µs and output signal voltage fall time less than 50 µs.

2.2.2.3 High Voltage (HV) power supply

Most of the radiation detectors require an external voltage supply known as detector bias for proper detection. Ionization chambers require low biasing voltage whereas semiconductor and scintillation detectors require bias voltage in the order of kV. The bias voltage for optimum resolution for the HPGe detector used in the present work is + 4500 V and this is provided from a programmable HV power supply which can provide +/- 5500 V maximum output accommodated in a Nuclear Instrumentation Module (NIM) bin of CAEN make. HV outputs are delivered through SHV connectors. The output polarity is selectable and the selected polarity will be indicated by two LEDs on the front panel. A provision for the ramping step size (RAMP-UP and RAMP-DOWN) selection is available. Safety features available in this HV model are over voltage and under voltage warning when the output voltage differs from the programmed value by more than 2%, a provision for setting maximum voltage to avoid the over biasing of detector and over current detection. When the over current status is lasting more than the pre set time, the output voltage will become zero either in the RAMP-DOWN rate or at the fastest rate.

2.2.2.4 Spectroscopy amplifier

The signal produced in detector is too small to be processed without amplification. The output signal from pre amplifier is connected to an amplifier for proper amplification of the signal. Generally the input of the amplifier is a tail pulse with a decay time of approximately 100 μs, and if another pulse is also coming within this period, the amplitude will increase and this is known as pile up. To avoid pile up either counter rate has to be decreased or a proper pulse shaping has to be provided. The spectroscopy amplifier also provides pulse shaping to prevent the pulse pile up and to optimize signal to noise ratio. A direct relationship between input and output amplitudes is required for obtaining pulse height information and a linear amplifier is used to preserve the same. In the present experimental set-up, a linear amplifier of Tennelec make with selectable peaking times of 1, 2, 4, 8, 16 and 24 μs is used. A peaking time of 4 μs is utilized for the present experiments. Gain range is a continuous variable from x 2.5 to x 3000 through coarse gain and fine gain adjustments. Coarse gain is facilitated through nine position rotary switch (5 to 2000 in a 1-2-5 sequence) and fine gain is facilitated by a ten turn precision potentiometer with linear calibration from 500 to 1500 in multipliers of 0.5 and 1.5. Provision for pole zero baseline correction is available in this amplifier through an adjustable P/Z control.

2.2.2.5 Multi-Channel Analyzer (MCA)

The linear amplifier output is fed to a Multi-Channel Analyzer (MCA) for further processing and it provides a visual display of the spectrum. When MCA operates in pulse height analyzer mode, the input pulses are sort out into channels according to the amplitude. A Single Channel Analyzer (SCA) counts the pulses between a lower limit and upper limit defined by the user. MCA can be considered as an array of SCAs with different lower and upper limits. Thus MCA covers the whole voltage range at the same time. In MCA the amplitude of the analog signal from linear amplifier is converted to corresponding digital signals with the help of an Analog to Digital Converter (ADC) and this digital value is used as the address of a memory location which will increment according to the pulse amplitude.

In nuclear spectroscopic systems, ADCs converts the analog signal to digital signal according to their peak value. Therefore, this ADC is known as peak sensing ADC. Most of the ADCs used for spectroscopy system is meant to work in the span of 0 to 10 V. The conversion gain of the ADC mentions the total number of channels available. The conversion is achieved with the help of a comparator where one of the inputs will be the analog signal to be converted. A constantly increasing ramp signal is applied to the other input of the terminal and when the ramp voltage becomes larger than the signal, corresponding digital value of the ramp is provided as the digital output. Another type of ADC which uses mainly for spectroscopy applications is Wilkinson type ADC, where a capacitor is charged using the input voltage. Then the capacitor discharges and a scaler counting from a constant frequency clock is gated on at the start of capacitor discharge. When the capacitor discharges fully, the scaler gate is put off and the contents in the scaler will be proportional to the charge on the capacitor. This method is more linear than other conversion methods and hence preferred for spectroscopy work. MCA sort out incoming pulses according to the pulse height of the analog signal with the help of an ADC and record the count at each pulse height in a memory. The value in each of this memory channel will increment corresponding to the digital value from ADC. The gamma spectroscopic data acquisition is done by FAST COM 8K MCA PC add-on card. It includes a built-in pulse height analyzing Wilkinson type ADC with 500 ns conversion time and 8 k conversion range i.e., 10 V pulse will be stored in 8192th channel. The present system provides 8192 channels and the number of counts corresponding to each channel i.e., pulse height spectra is displayed. The features are high-resolution graphics displays with zoom, linear and logarithmic (auto) scaling, grids, region of interests, Gaussian fit, calibration using diverse formulas and FWHM calculations.

2.2.3 Shielding

The source and detectors are well shielded to ensure the minimum background radiation and to increase the signal to noise ratio in the detector resulting in improved sensitivity. The sources employed in scattering and transmission experiments are shielded using 160 and 100 mm thick lead cylindrical structures respectively and the detector with 50 mm thick lead shield. The lead shields are lined and enclosed in stainless steel sheets of thickness 5 mm.

2.2.4 Collimators

In the present study, well collimated source and detector systems are employed. In scattering experiment, collimating the source and detector help to obtain the information from an elemental volume determined by the intersection of source and detector beams known as voxel. Multiple scattered photons affect the signal-to-noise ratio and reduce the contrast and sensitivity and can be minimized by introducing a ‘hard collimation’ or collimators. In transmission experiments collimators are used to obtain narrow parallel beam geometry and to avoid the buildup factors. Cylindrical lead collimators of various sizes and opening diameters (7 mm and 5 mm) are used in the present experiment to achieve the best results in each case studied.

2.2.4.1 Voxel size calculation

In a gamma scattering experiment, the size of the voxel determines the spatial resolution of the system. When smaller diameter source and detector collimators are used with a reduced distance to sample position small voxel size can be achieved. As the distance between source to sample and sample to detector increases, divergence of beam also increases and this results in the increase of the voxel size. An accurate calculation of voxel size is needed for proper interpretation of the result. Similarly during the design of a system, or during the selection of proper collimators or source detector locations, an idea about the voxel size is unavoidable. Since the source beam and detector point of view are divergent in nature, voxel size can be calculated from determining the intersection volume of two cones. The voxel size is calculated using the method described by Balogun [4, 5] from the information of scattering angle, collimator length, diameter and distance between the sample to source and sample to detector.

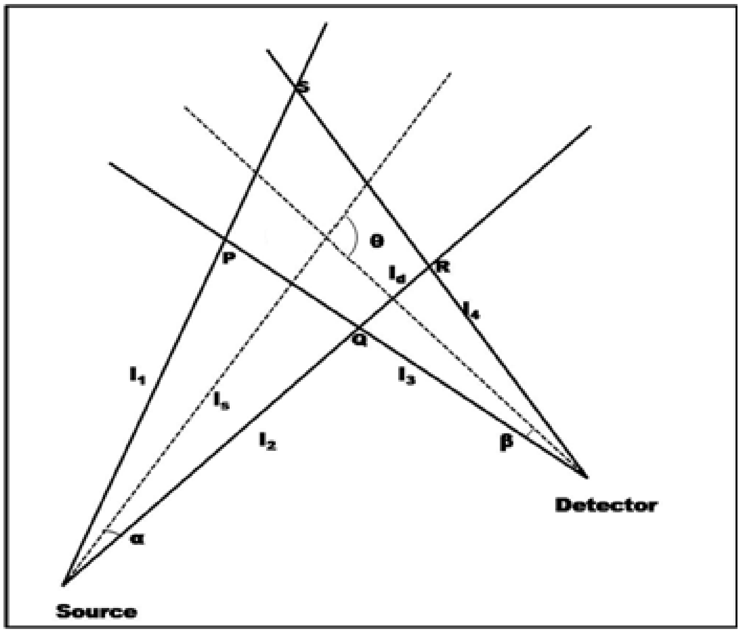

Figure 2.7 Geometry used for calculating the voxel size.

The voxel size is calculated using analytical and Monte Carlo methods. The geometry used for calculating the voxel size is shown in figure 2.7 and the scattering angle θ, divergence of source and detector beams α and β respectively are marked in the same figure. The parameters α and β are calculated from the collimators length and radius. The equations of four straight lines (l_1, l_2, l_3 and l_4) can be obtained from α and β and the intersections of any two pair of these lines define the corners (P, Q, R, S) of the voxel. In analytical method a sequential scanning of an elemental volume of known size across the volume defined by the region PQRS is carried out. Whenever the elemental volume is inside the voxel defined by the corners (P, Q, R, S), a counter is increased. Finally the total volume is calculated as the product of counter and the elemental volume.

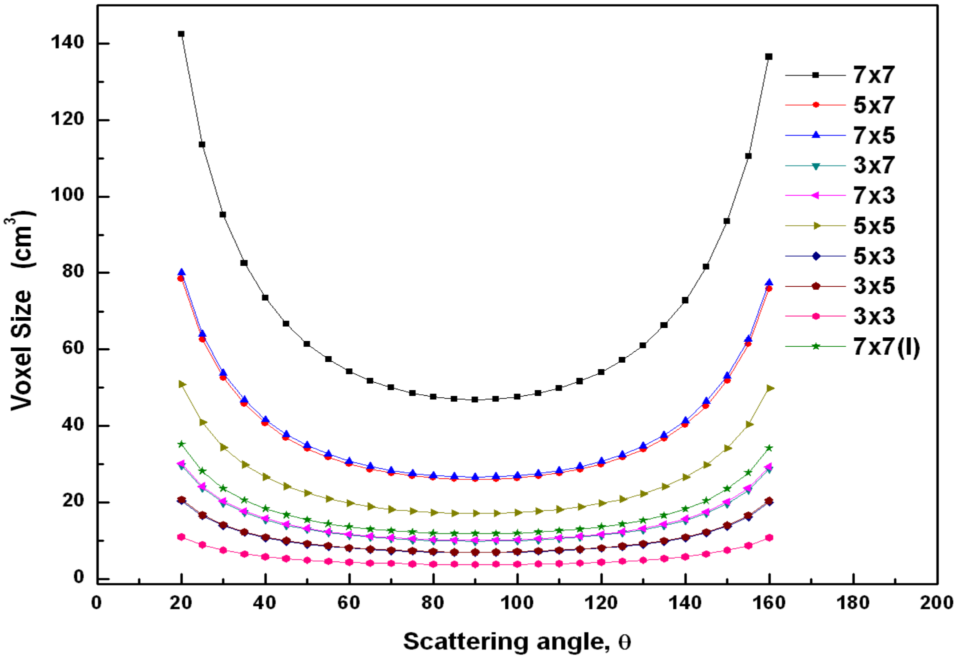

Figure 2.8 Calculated voxel sizes for different collimator combinations (source diameter x detector diameter) as a function of scattering angle.

The size of the voxel for various collimators and scattering angles are calculated. Figure 2.8 shows calculated voxel sizes as a function of scattering angle for various source detector collimator combinations. It can be seen that voxel size is minimum at 90º and remains almost same in the angular range 60 to120º and all the experiments are carried out in this angular range. It is observed that a smaller voxel size resulting in improved spatial resolution can be achieved by incorporation of 3 mm collimators for source and detector. But relatively higher scanning times are needed to achieve even a 2% statistical uncertainty in scattered intensity and it demands a compromise between scanning time and achievable spatial resolution. Hence a 7x7 combination (i.e., 7 mm collimators for both source and detector) is selected only when bulk properties are to be determined. A 5x7 source-detector collimator combination is used for obtaining desired improved resolution in some of the experiments. All the collimators selected are of length 8 cm. The voxel size comparable to that obtained by using 3 mm collimators either on source or detector can be achieved by selecting a 7 mm diameter and 14 cm length collimator (7x7(l)) with less divergence at detector end as seen in figure 2.8. This combination of collimators is used for three dimensional imaging experiments which demanded a higher accuracy.

When the sample size is much smaller compared to voxel selected for investigation, a condition which describes the geometry of the sample is also incorporated to the above method. The condition imposed is that the scattering volume is considered only when the elemental volume is inside the intersection of two cones as well as the geometry of the sample defined.

2.3 Experimental procedure

The scattering experimental set-up consists of CNC controlled 6-axis source detector system and a 4-axis job positioning system. The source and detector are mounted separately on the source and detector sub assemblies of 6- axis system. The motion of the specimen disk is derived by 4 servo motors. Three motors are used to move it in three mutually perpendicular Cartesian coordinate system denoted X, Y, Z. One more servo motor used to rotate it and this coordinate is denoted as W. The servo motors are controlled by Galil's DMC 2040 motion controller programmed with Galil commands and the commands are communicated from PC via high speed RS 232 port. The DMC controller will send the pulses to servo motors. In the present system each pulse will move along X, Y, Z-axes linearly by 1 micrometer and each pulse corresponds to 0.0004° rotation in the W axis. The servo driver receives the input signals from the controller system for generating motion in servomotors by transmitting the electrical signal according to the signals from the controller. The controller system can be programmed by the user as per the required motion. The controller is programmed by the binary or ASCII Galil Commands. The positional accuracy of source and detector system is ± 50 μm for X and Z-axis travel stages and for 4- axis job positioning system it is ± 10 μm for X, Y and Z-axis travel stages. The positional accuracy for θ rotary stages for both the systems is ± 0.25°.

The scattering source and detector positions can be moved using the user input commands. An optical method using laser pointer is used to ensure the alignment and to locate the scattering position. The sample holder is at a distance of 93.4 cm and 52.1 cm from the source and the detector surfaces respectively. A test specimen is placed in the centre of the scattering position and the scattered intensity is recorded. An exact scattering location is zeroed on by moving the test specimen around the scattering position and this corresponds to the maximum intensity point. In similar way transmission source and detector positions are optically aligned and the sample holder position is fixed as described earlier. The sequence of sample movement and data recording are automated and synchronized and is described in detail in the next section.

2.3.1 Automation details

Three dimensional scanning of the objects are obtained using a raster movement of sample along the lateral, horizontal and vertical directions. To achieve fast and effective voxel by voxel scanning, it is required to have a synchronized data collection and automatic translation of the sample (or detector and source system). In the present work, the translation, rotation and vertical motions of 4-axis CNC controlled job position system and MCA data acquisition are fully automated and synchronized using VB based windows application program. The block diagram of the components used for automation and synchronization of sample movement and data collection is shown in figure 2.9.

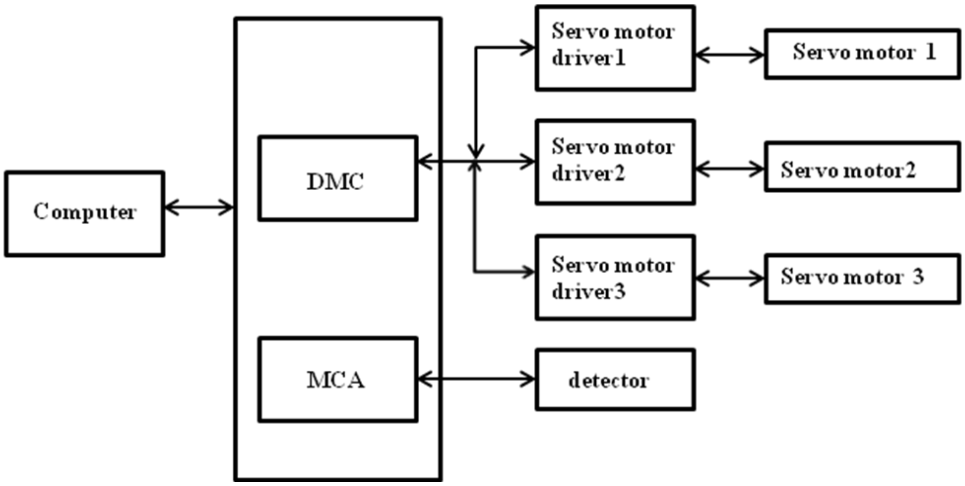

Figure 2.9 Block diagram of automation and data collection

The data acquisition, parameter setting of the MCA and the 4-axis motion are automated using dynamic link library and Galil Active-x tool files. The PC first send the signal to DMC to reset the position by energizing the servo motors and then it will direct the MCA to collect the data in preset live time. Many different tasks can be executed by simple commands such as initialization, position sensing, repositioning the scanner, start and stop a measurement, store the accumulated data on disk and automatically execute all steps for a complete sequential scanning. The collected counts in the specified energy region are stored in the output file of PC. The output file contains parameters of collection time, scanning period, X, Y and Z positions, gross and net photopeak counts for the given region of interest. Figure 2.10 shows the images of control panel (top) and automation screens (bottom).

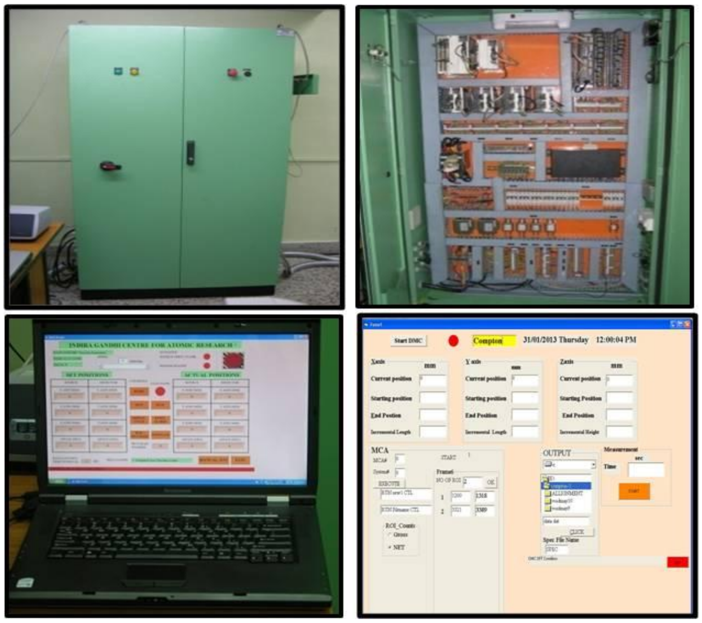
Start DMC
Compton
31/01/2013 Thursday 12:00:04 PM
X axis
Y axis
Z axis
mm
Current position
Starting position
End Position
Incremental Length
Incremental Height
MCA
MCA#
System#
EXECUTE
START
Frame
NO OF ROI
OK
ROI_Counts
Gross
NET
OUTPUT
ALLIGNMENT
CLICK
Spec File Name
Measurement
sec
Time

Figure 2.10 Images of control panel and data collection screen

2.3.2 Data analysis

Scattering and transmission PHS are collected simultaneously and appropriate corrections are applied for continuum and background counts. Figure 2.11 is a typical PHS showing scattered and transmitted photo peaks at 252 and at 661.6 keV respectively. A background spectrum is collected with bare sample holder without any sample in its position and the same is subtracted from all the spectra for further analysis.

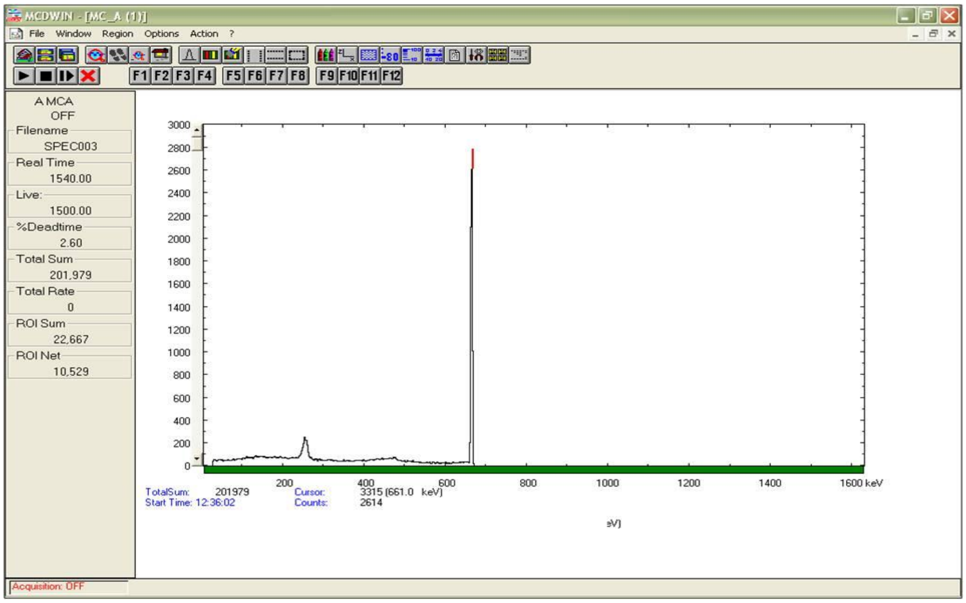
MCDWIN - [MC_A (1)]
File
Window
Region
Options
Action
?
F1
F2
F3
F4
F5
F6
F7
F8
F9
F10
F11
F12
3000
2800
2600
2400
2200
2000
1800
1600
1400
1200
1000
800
600
400
200
0
200
400
600
800
1000
1200
1400
1600 keV
eV]

A MCA
OFF
Filename: SPEC003
Real Time: 1540.00
Live: 1500.00
%Deadtime: 2.60
Total Sum: 201,979
Total Rate: 0
ROI Sum: 22,667
ROI Net: 10,529
TotalSum: 201979
Start Time: 12:36:02
Cursor: 3315 (661.0 keV)
Counts: 2614
Acquisition: OFF

Figure 2.11 PHS of scattered (252 keV) and transmitted (661 keV) intensities

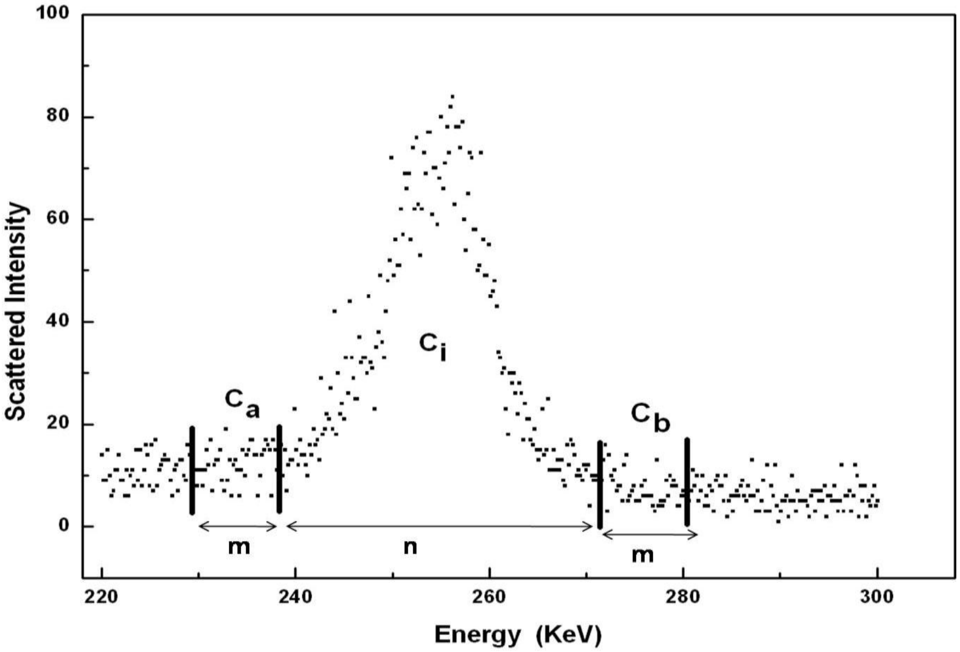

Figure 2.12 Continuum subtraction for photopeak

The area under the photopeak is used for further analysis. But the scattered photo peak is affected by the Compton continuum of transmitted intensity and hence a proper correction is required and this is carried out as follows [3]. The integrated counts under the photo peak for n channels are calculated as C_i as indicated in figure 2.12. A constant Compton continuum contribution to the photo peak is assumed in the present case and taken into account. The counts to be subtracted from photo peak are obtained by calculating the average continuum count per channel from the gross count of m channels Ca and C_b as indicated in the figure 2.12. The corrected photo peak count C is calculated using the following formula:

$$C = C_i - n\frac{(C_a + C_b)}{2m} \tag{2.1}$$

2.4 MCNP

The Monte Carlo simulations have been done to provide support of the experiment. The simulation takes into account the detailed known characteristics of the source, detector and the scatterer, in calculating the PHS. The MCNP4C [1] radiation transport code developed by Los Alamos National Laboratory, USA is applied to perform the calculations in this work and it is a general purpose, three-dimensional general geometry, time-dependent code, which is used to calculate coupled neutron-photon-electron transport in bulk media. For photons, the code accounts for incoherent and coherent scattering, the possibility of fluorescent emission after photoelectric absorption, absorption in pair production with local emission of annihilation radiation, and bremsstrahlung. MCNP provides a nearly predictive capability of how radiation interacts with matter. In MCNP simulations, each particle (photon) is tracked from creation to termination with all interactions based on physics models and cross-sections, and all decisions (location of interaction, scattering angle, etc.) are based on pseudo-random numbers. Usually, the results of a simulation are normalized per starting source photon. New source photons are randomly created until a preset number of histories are tracked and the simulation is ended. The MCNP code is very effective in obtaining a simulated spectra produced by gamma rays in a detector provided the experimental set-up can be modeled accurately.

2.4.1 Detector, source model

A detailed three dimensional geometry consisting of well collimated and shielded source and detector assemblies and the object is modeled with exact dimension, distance and orientation. Two ^{137}Cs radioactive source capsules each of activity 77.7 GBq (total 155.4 GBq) deposited inside stainless steel and the HPGe detector is modeled with the surrounding lead shielding and a 0.007 m beam collimator for both source and detector. The HPGe detector consists of a crystal of size 0.066 m × 0.066 m surrounded and sealed by an aluminum layer of 0.002 m thick in front and 0.001 m on sides. Sample dimensions and their distances from the collimator edge of source and detector set-up, the scattering angle and the sizes of the source and detector collimators are incorporated in the modeling. Any small deviation in the geometrical parameters of the entire set-up may lead to inaccuracy in the simulated spectra. Hence great care has been taken while measuring the distances, angle etc. For modeling the source and detector, the cross sectional diagrams given by the supplier/manufacturer have been referred.

2.4.2 Pulse Height Spectra (PHS) simulation

The simulated PHS can be compared with the experimental ones to support the experiment and confirm the results. The PHS in MCNP is the distribution of the energy deposited in a “cell”, i.e., the gamma ray energy spectrum in a physical model of a detector.

F8 tally: F8 tally of MCNP is employed to obtain the simulated PHS and it is analogous to physical detector. The estimation is based on the following approach. When a photon enters the cell, the cell is credited with energy (E_{in}) times the weight (ω) of the incoming photon. If the photon leaves the cell, the product of Energy (E_{out}) and weight (ω) is deducted from the cell energy.

$$E_{cell} = \sum_{tracks} (E_{in}\omega - E_{out}\omega) \tag{2.2}$$

At the end of each history, the energy in each cell is divided by the source weight. Hence for each history, only one count is added to the spectrum. The pulse height tally is used to obtain the energy distribution of pulses created in the volume of the germanium crystal. The F8 energy bins correspond to the total energy deposited in a detector in the specified channels by each physical particle.

GEB card: Gaussian broadening is provided to the spectra by MCNP function called 'GEB card 'and hence a good representation of the experimental spectra is achieved. The constants a, b and c take care the broadening and they are obtained from

$$FWHM(MeV) = a + b\sqrt{(E + cE^2)} \tag{2.3}$$

where E is the energy in MeV. Scattering experiments are performed at three different angles using the same set of source and detector collimators and the corresponding FWHM and scattered energy values are used to obtain the constants a, b and c.

Source biasing: For the pulse-height estimates used in this study, the source biasing represents the only feasible method to improve computational efficiency. Source is adjusted to emit into a restricted solid angle depending upon the collimator size, and thus to avoid unneeded calculations.

Binning and comparison: The simulated pulse height spectra contain 28 bins each with 3.615 keV width and the photon energies ranged from 198 to 303 keV. The experimental spectrum is rebinned to the same energy grid as of MCNP for comparison. Each simulation is run with 2.1×10^9 source particles for decreasing the relative variance. Each value of simulated spectra is multiplied by source activity and acquisition time to make the simulated spectra directly comparable with the background subtracted experimental PHS.

References

1. Briesmeister, J.F., (Ed), MCNP™, LA-13709-M Manual, (2000)
2. Leo, W.R., "Techniques for Nuclear and Particle Physics Experiments", Second revised edition, Springer, First Indian reprint (2010)
3. Knoll, G.F., Radiation Detection and Measurements, Third Edition, Wiley-India, (2009)
4. Balogun, F.A., Appl. Radiat. Isot., 50 (1999), 317-323
5. Balogun, F.A., Brunetti, A., Cesareo, R., Radiat. Phys. Chem., 59 (2000), 23-30

Chapter III Detection and quantification of thickness loss due to corrosion in mild steel

3.1 Introduction

Corrosion is the degradation of materials due to interaction with its environment and it is one of the major problems in infrastructure maintenance and responsible in part for deterioration of capital-intensive systems, such as bridges, buildings, nuclear power plant concrete structures, pipelines, storage tanks, aircraft ships, cars, trucks, and machinery. Corrosion can cause serious damage to structures, which include leak, crack and this eventually leads to the breakdown of the structure itself. Thus periodic inspection, early detection and prevention of corrosion are highly desirable for any industry for its sustainable growth. A wide range of Non Destructive Evaluation (NDE) techniques have been reported in the literature that may be suitably employed for the monitoring of corrosion of steel for the purpose of diagnosing the cause and extent of the corrosion. Many of the technologies of NDE lend themselves to the detection, characterization and quantification of corrosion damage and generally the methods for corrosion detection depend on the thickness loss of the component during corrosion. This is normally the underlying concept for corrosion detection by NDE methods. No single means of corrosion detection is either ideal or suitable for all forms of corrosion. Visual inspection is the simplest detection method. But there are many occasions where visual inspection cannot work out like hidden corrosion in insulated pipes, inside the pipes in processing plants and petrochemical industry, in reinforced concrete structures and in aircraft industry. Eddy current test, radiography, ultrasonic method, acoustic emission method and leak test are some of the other methods used for this purpose.

Gamma scattering NDE technique for corrosion detection is desirable because the technique doesn't demand two sided access and which can be used for imaging large vessels containing hot, corroded objects and unclean and rough surfaces [1]. Gamma scattering technique is a suitable method for corrosion detection due to following reasons; i) it doesn't require any surface preparation ii) it can be used at any temperature iii) measurement can be carried out safely and iv) the system is portable [2]. The utility of scattering technique for contactless thickness measurements in steel sections was studied earlier [3-5]. By introducing different wall thicknesses and paraffin deposits, the feasibility of scattering technique for detection of corrosion and paraffin deposit thickness was studied [6-11], and a direct relationship between the thickness and scattered intensity was established. Scattered intensity profile obtained from scattered intensities at different point along the thickness of sample was used to determine the thickness. As the thickness of the sample increases, there exists a saturation thickness and from that thickness onwards scattered intensity starts falling due to attenuation effect. This saturation depth depends upon the incident photon energy, composition and density of sample. When high-energy gamma rays are used, greater saturation depth is obtained for low atomic number (Z) and low density samples.

A Compton scattering method for detection and quantification of corrosion in Mild Steel (MS) plate is discussed in this chapter. Since MS is a high density material, the attenuation of incident and scattered gamma rays is very high. Owing to this fact a direct relationship between the thickness and scattered intensity cannot be established in MS plates. A reconstruction algorithm to reconstruct the densities of the objects under investigation and an unambiguous interpretation of the signal as a function of material thickness at any point of the thick object being inspected is described. In this method only the knowledge of the target material's mass attenuation coefficients (composition) for the incident and scattered energies are enough to reconstruct the thickness of the each voxel of the specimen being studied. A reference sample (uncorroded) with known thickness is selected for quantification of thickness loss. A comparison of quantification of corrosion using scattering technique with ultrasonic technique is available in the literature [2]. In the present work the results of gamma scattering technique is compared with other radiation based NDE techniques such as radiography and gamma transmission.

3.2 Algorithm used for attenuation correction and density iteration

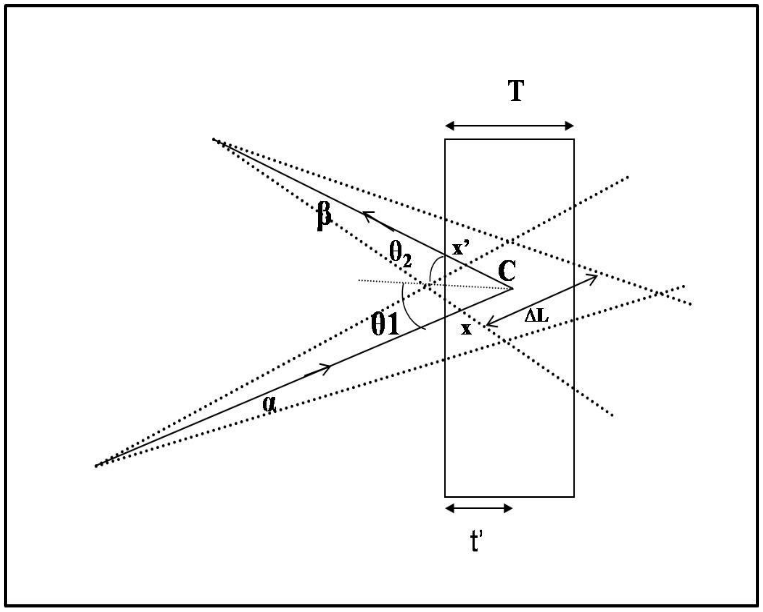

Figure 3.1 Geometry for calculating the attenuation factor

The intensity of scattered photon that reaches the detector from a sample is a combination of three processes (attenuation of the incident gamma photons, scattering and attenuation of the scattered gamma photons) and the detail description of final relation between these processes and the scattered intensity is given in section 1.2.3.1. The modification required for the equation (1.13) to quantify the thickness loss is as follows.

The geometry for calculating the Attenuation Factor (AF) for the voxel is shown in figure 3.1. Let C be the point at the centre of the voxel, α and β are the incident and scattered paths respectively and t' be the thickness of the MS flat plate at which scattering takes place. Then for this case the incident and scattered paths are given by the following relations.

$$x = \frac{t'}{\cos(\theta_1)} \tag{3.1}$$

$$x' = \frac{t'}{\cos(\theta_2)} \tag{3.2}$$

The attenuation factor (AF) given by equation (1.15) can be rewritten in terms of equations (3.1) and (3.2) as follows:

$$AF = \int_0^T \exp-\left\{\left(\frac{\mu(E\ )}{\rho}\right)\rho\frac{t'}{\cos(\theta_1)} + \left(\frac{\mu(E')}{\rho}\right)\rho\frac{t'}{\cos(\theta_2)}\right\}dt'$$

$$= \frac{\left[1 - \exp-\left\{\left(\frac{\mu(E)}{\rho}\right)\sec(\theta_1) + \left(\frac{\mu(E')}{\rho}\right)\sec(\theta_2)\right\}\rho T\right]}{\left(\left(\frac{\mu(E)}{\rho}\right)\sec(\theta_1) + \left(\frac{\mu(E')}{\rho}\right)\sec(\theta_2)\right)\rho} \tag{3.3}$$

The equation (3.3) is incorporated in equation (1.13) for the quantification of thickness loss. The average thickness of voxel for corroded plate can be calculated by taking the ratios of

$I_s(P)$ of corroded to reference and an algorithm is written for obtaining thickness by incorporating the above equations into it.

3.3 Experimental procedure

3.3.1 Sample description

Two MS flat plates (a corroded and another one a non-corroded taken as reference) of dimensions 23.5 (length) x 15.5 (breadth) cm^2 were chosen for corrosion detection and quantification. Thickness of the reference sample was 1 cm.

3.3.2 Gamma scattering method

The MS plates were placed on the sample holder at a distance of 84.5 cm from the source and the detector's distance from the plates is 33.7 cm with the angle of scattering 109º. Both the source and detector are collimated using collimators of 7 mm diameter and the size of the resultant voxel was of 20.85 cm^3. Scattered photon intensities from five different locations of the reference and corroded plate were detected and analyzed using MCA card. A background spectrum for the same duration was recorded without samples in position and subtracted from those scattered spectra recorded with sample in position and the scattered intensity was calculated from the area under the photopeak. The same experiments were also carried out at scattering angle of 91º.

3.3.3 Gammatography

The gammatography experiments were carried out using the same computer controlled scanning system in a narrow beam and good transmission geometry set-up consisting of 3 mm collimator in source and 7 mm collimator in detector. The transmitted photon intensities with and without samples in position recorded and the thickness loss was estimated from the measured transmitted intensities.

3.3.4 Radiography

The radiography of the MS plates was carried out using Balteu 160 kV X-ray machine. The digitized radiographs with a resolution of 50 μm were processed for the detection of corrosion damage in five different locations. Optical density of the film will vary with the change in thickness for a particular material which is radiographed and the calibrated values with known thickness variation are taken as input for determination of corrosion damage at the unknown location.

3.4 Quantification of thickness loss

The experimental scattered Pulse Height Spectra (PHS) is plotted as a function of energy for reference and corroded MS flat plates at two scattering angles and is shown in figure 3.2.

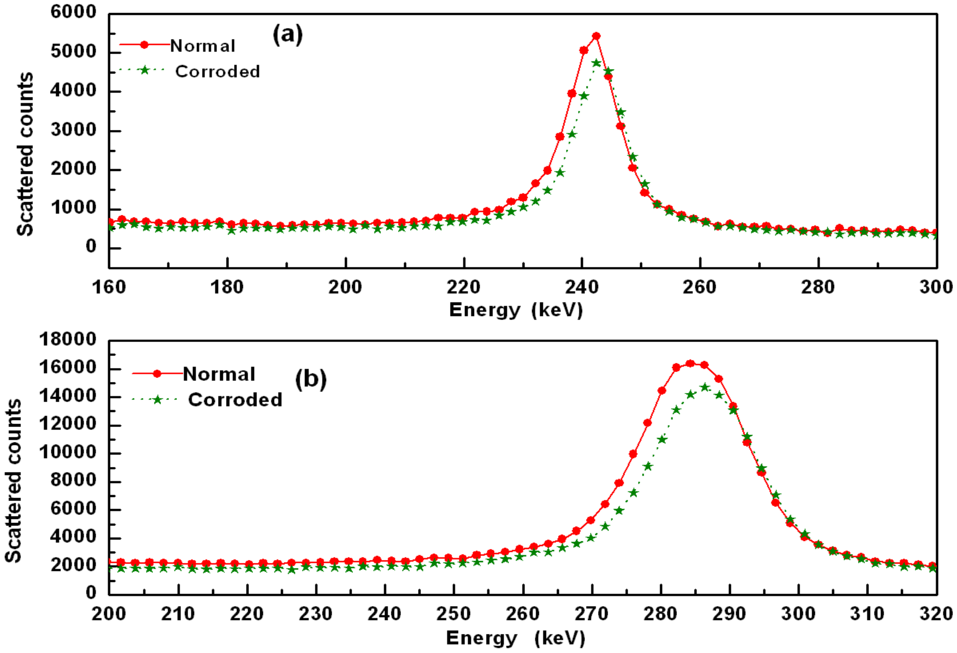

Figure 3.2 Experimental scattered PHS obtained from reference and corroded MS plates for scattering angles of 109° (a) and 91° (b).

The scattered intensities are calculated from the area under the photo peak of the background subtracted spectra. The scattered intensity from corroded MS flat plate decreases by 11.95% and 12.13% at scattering angles 109º and 91º respectively (figure 3.2) compared to reference plate. The decrease in scattered intensity from the corroded plate is due to the reduction in electron density. Since corroded and non-corroded plates are made up of same material, the decrease in electron density can be attributed to reduction in material volume and as the area of the scanning region remains the same in both the cases, the decrease in material volume is due to the reduced thickness. Hence the scattered intensity is directly related to the thickness of the voxel investigated. The average thickness of corroded MS plate is reconstructed from the corresponding experimentally obtained scattered intensities using the reconstruction algorithm described in section 3.2. A decrease of 2.8 and 2.91 mm from the reference sample thickness (10 mm) for scattering angle 109° and 91° are obtained from the reconstructed intensities of PHS shown in figure 3.2(a) and 3.2(b). The experimental results are derived from the scattered intensities obtained from the corresponding voxels of corroded and reference samples and the thickness loss obtained at two different scattering angles are in good agreement with each other. This confirms the validity of reconstruction algorithm for any scattering angle. The background subtracted scattered spectra from five different locations of the sample are shown in figure 3.3 and the photo peak region of the spectra are shown in the inset.

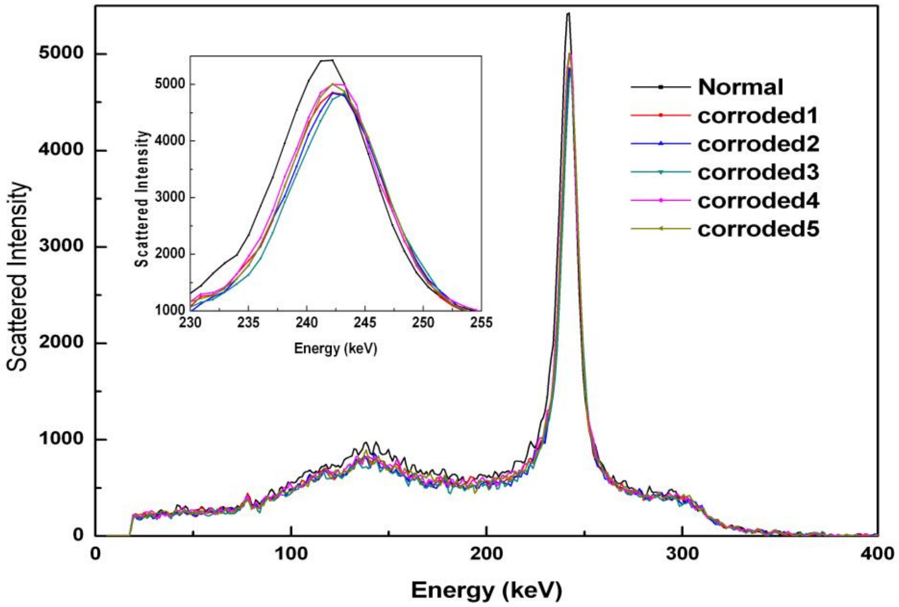

Figure 3.3 Experimental scattered PHS for scattering angle of 109° obtained from normal and from different spatial locations of corroded MS plates and corresponding photo peaks are shown in the inset

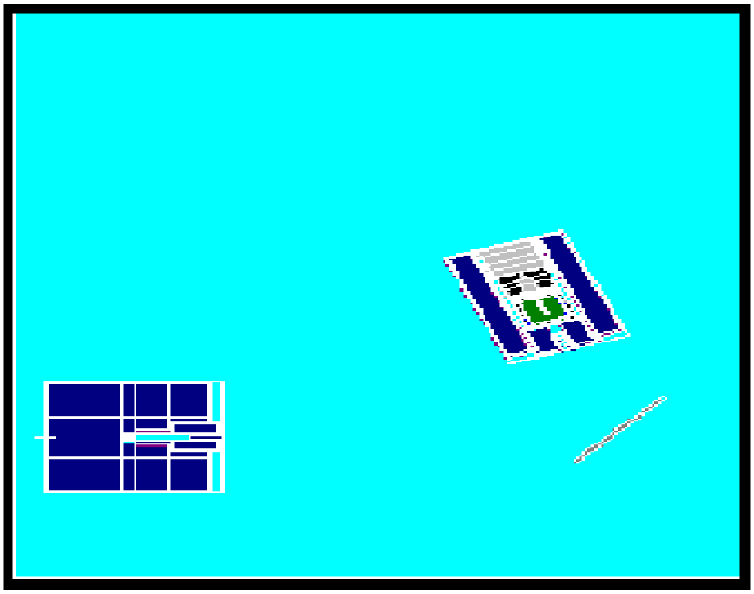

Figure 3.4 Cross sectional view of experimental set-up modeled in MCNP

The cross sectional view of MCNP [12] simulated geometrical set-up is shown in figure 3.4. The exact dimension and geometrical details of the experimental arrangement are incorporated in the modeling. The result of MCNP PHS simulations and their comparison of the spectral shape with the experimental ones are shown in figure 3.5.

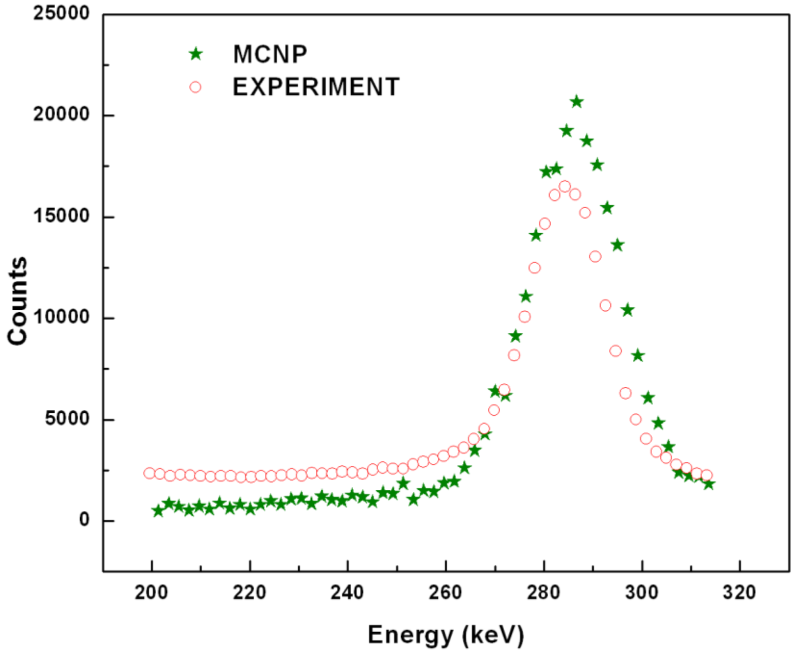

Figure 3.5 Comparison of MC simulated scattered spectra with experimental results at scattering angle 91°

A good agreement in the shape of the PHS is observed between the experimental spectra and those of Monte Carlo (MC) simulated ones. Thus measurements support the MC simulations. In field conditions one will be looking for corroded structures with density losses varying from few percent onwards. The MC simulation of MS flat plate corrosion varying from 0.0% extending up to 60% is carried out. The photo peaks of the simulated scattered spectra are shown in figure 3.6 and a gradual decrease in the scattered intensity is observed as a function of a magnitude of corrosion.

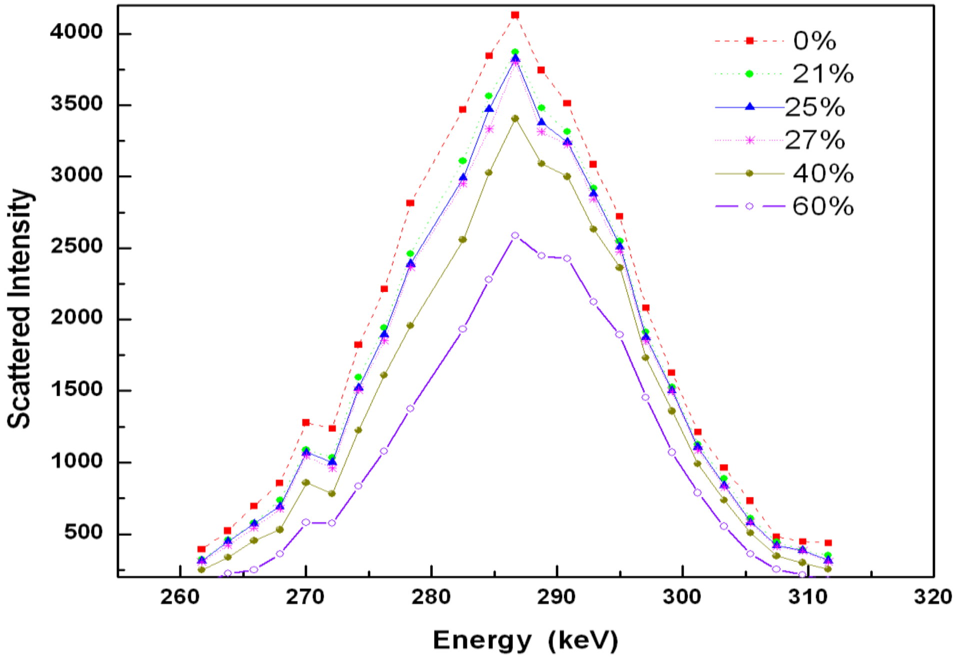

Figure 3.6 Simulated PHS for various amount of corrosion

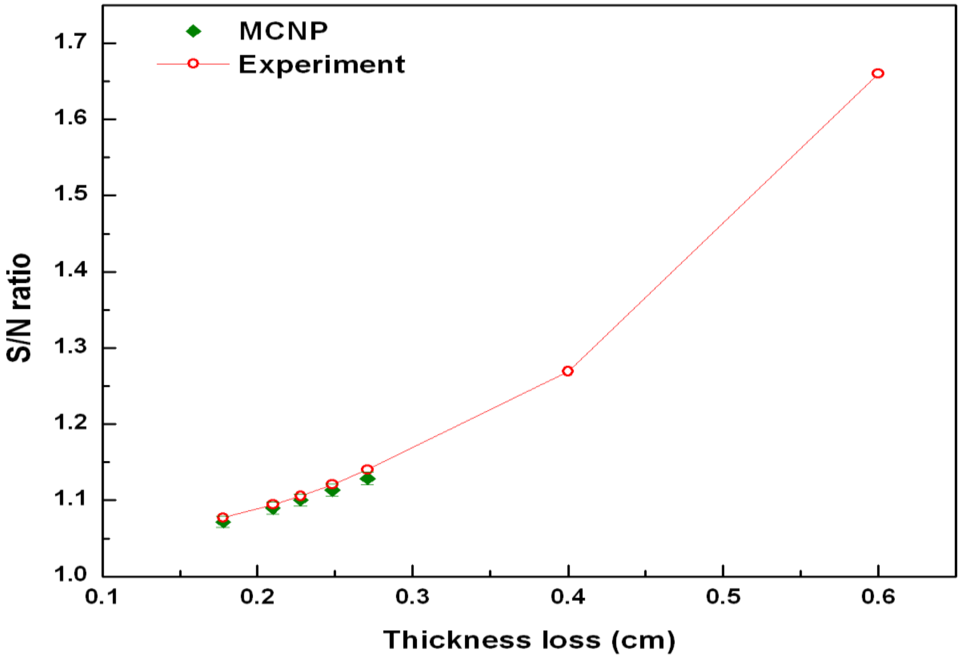

Figure 3.7 Quantitative estimates of the values of S/N plotted as a function of thickness loss

A quantitative estimate of the values of signal -to- noise (S/ N) ratio from these spectra i.e., the ratios of count rate of reference MS plate to corroded one as a function of thickness loss are plotted and are shown in figure.3.7. A good agreement in S/N ratios is obtained between experimentally obtained and MC simulated spectra. In the present experiment, a minimum thickness loss of 1.77 mm is detected which corresponds to a decrease in intensity by 6.7%. Theoretically, a decrease in count by three standard deviations will ensure 99.7% confidence level and a probability of false alarm as less as 0.0015 [11] can be considered as corrosion and which is equivalent to 0.5 mm decrease in thickness. But in experimental conditions, the contribution from background and electronic noise should also be considered. Considering all these factors, if a decrease of scattered intensity by more than 5% is considered as corrosion, minimum detectable limit using the present experiment set-up is 1.4 mm. The functional dependence of Compton scattered intensity with thickness is established through simulation and experiment.

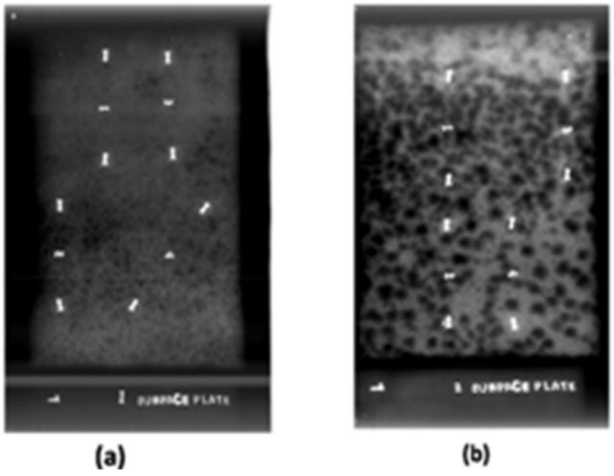

Figure 3.8 Radiographic images of (a) reference sample and (b) corroded sample

Figure 3.8 shows the radiographic images of the reference and corroded plates. It is observed form the radiographic image figure 3.8(a) that corrosion damage initialization has occurred in the reference plate also. Thicknesses at five different locations of corroded MS plate are evaluated using the known calibrated values of reference sample thickness.

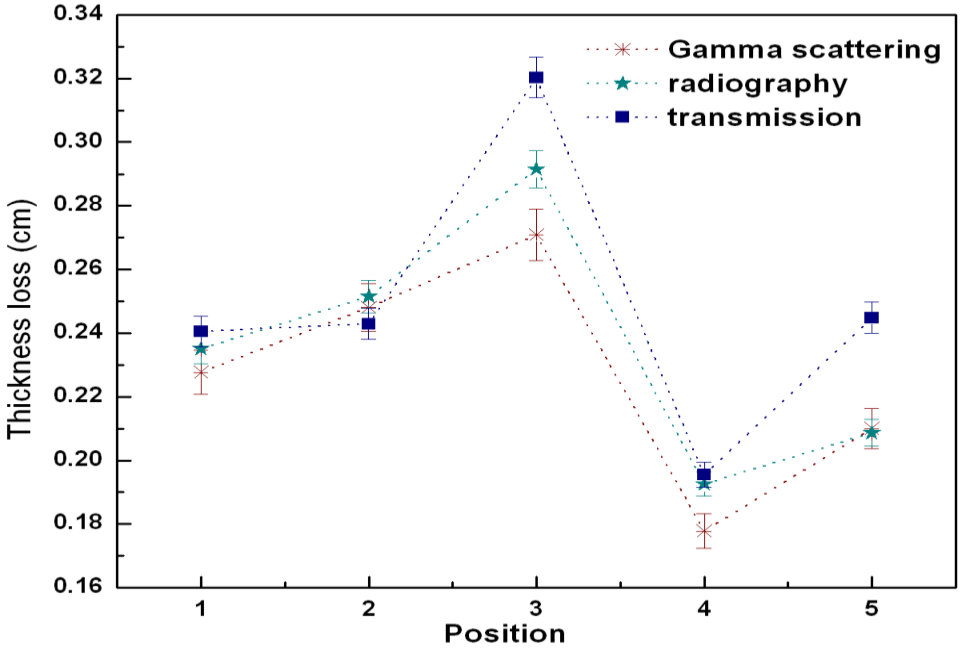

Figure 3.9 Measured thickness loss in cm by gamma scattering, radiography and gammatography techniques

The loss in thicknesses due to corrosion measured by gamma scattering method are compared with those values obtained from gammatography and radiography techniques and are shown in figure 3.9. The error on measured thickness loss by gammatography, scattering and radiography is 2%, 3% and 2% respectively. Statistical uncertainties and the errors on the mass attenuation coefficients taken from photon cross section database XCOM [13] are taken into account in calculating the resulting error in the thickness loss determination. The errors on transmitted and scattered intensities are less than 1%. A relative error of 1% is considered for the mass attenuation coefficients [13]. The percentage thickness loss estimated at different positions of the corroded MS plate varies from 17.78 - 27.0 by gamma scattering, 19.5 - 32.03 by gammatography and 19.26 - 29.15 by radiography method.

The variation in the results obtained by different methods is due to the following reason. Thickness loss determined by all of these methods is the average point values obtained from a fixed area of the voxel chosen and this is likely to be slightly different in each method. Overall three different techniques showed the same trend at all the five positions and hence these results are consistent and in line with each other. The accuracy of the results can be improved by reducing the voxel size

Even though the present study is limited to corrosion of mild steel, it can be extended for thickness measurement in any materials with low Z value. Relatively lower source strength or low energy X-ray or gamma sources can be used for materials with low Z and low density. Corrosion hidden by insulators or surface coatings can also be detected by providing proper attenuation correction. Moreover, compared to radiography, radiation exposure is much lower in the case of gamma scattering method [6]

References

1. Abdul-majid, S., Balamesh, A., *18th World Conference on Nondestructive Testing*, (2012)
2. Dawoud, U M., Corros. Sci., 51 (1995), 660-663
3. Putman, J.L., Jefferson, S., Cameron, J.F., Kerry, J.P., Pulsford, E.W., J. Sci. Instrum., 32 (1955), 394398
4. Asa’d, Z., Asghar, M., Imrie, D.C., Meas. Sci. Technol., 8(1997), 377-385
5. Silva, I.L.M., Lopes, R.T., de Jesus, E.F.O., Nucl. Instrum. Meth. A., 422 (1999), 957-963
6. Abdul-majid, S., Tayyeb, Z., *Middle East Nondestructive Testing Conference & Exhibition*, (2005)

7. Lopes, R.T., Valente, C.M., de Jesus, E.F.O., Camerini, C.S., Appl. Radiat. Isot., 48 (1997), 1443-1450
8. Abdul-majid, S., Deasalination, 91 (1993), 35-49
9. Yacout, A.M., Van Haarsen, M.H., Dunn, W.L., Appl. Radiat. Isot., 48 (1997), 1313-1320
10. Bridge, B., Gunnell, J.M., Imrie, D.C., Olson, N.J., Nondest. Testing. Commun., 2 (1986), 103-113
11. Ong, P.S., Patel, V., Balasubramanyan, A., J. Nondestruct. Eval., 16 (1997), 135-146
12. Briesmeister, J.F., (Ed), MCNP™, LA-13709-M Manual, (2000)
13. Berger, M.J., Hubbell, J.H., NBSIR 87-3597, MD 208991987

Chapter IV Measurement of concentration and interface level of fluids/solutions

---

4.1 Introduction

There are many situations where the fluid level has to be monitored or maintained continuously. The fluid monitoring technology has come of age in recent years; its level of sophistication varies widely across industries. Detection of levels and the decision according to that are required in the catalyst plants. Waste water treatment plants need to continually monitor various parameters like Biochemical Oxygen Demand (BOD), Chemical Oxygen Demand (COD), and total dissolved solids and water levels [1]. Float gauge where a buoyant solid floats on the top of the fluid and sight gauge in which a transparent tube is attached to the sides of the container are the two basic level detection methods [2]. But when two fluids are transparent, interface level determination using sight gauge will be difficult. Similarly, in sealed containers float gauge is also less reliable. Ultrasonic, radar, florescence and capacitance based level measurements are some of the many methods that widely used for this purpose. No single means of fluid density and interface measurement techniques are either ideal or suitable in all cases. There are major advantages and disadvantages of each fluid level and interface characterization technologies.

Gamma ray based measurement is a viable tool for the level monitoring of highly carcinogenic, toxic, explosive and pressurized fluids as it doesn’t require any physical contact with the fluids. Fluid level gauging based on this technique is very effective in fully enclosed, high temperature and high pressure vessels where level measuring devices of contact type are impossible or undesirable to use. Gamma transmission based liquid-level gauges are widely used in the petroleum industry to measure the level of hydrocarbons in cracking units and tank farms, and in the chemical industry for determining the height of various materials in closed vessels or reactors. In processing industries, levels of molten glass, molten metals, and paper pulp slurries in closed vessels are also being measured in this manner. The heights of solids, such as catalysts in hoppers or scrap metal in cupolas, are being controlled with transmission level gauges [3]. There are some instrument's descriptions available in literature where gamma ray transmission level sensors are used [4, 5]. Collimated gamma rays are used in both transmission and back scattering geometry for the fluid level gauging [6]. Density measurements for solutions (miscible and immiscible) and slurries in pipelines are carried out on-line using gamma scattering transmission methods [7]. The bulk density of slurries can be used for the calculation of solid weight fraction [8, 9]. When there is no well defined boundary between the liquids, the interface region can be characterized by determining the density variations from one liquid to other. In pipelines, the density profile measurement is employed to know the time of arrival of each liquid and extend of interface [10]. This technique is employed in well logging to locate the interface between liquids in underground storage cavities [11]. Radiation based density profile measurement of liquids is used in distillation columns. When the two interfacing liquids are similar in density (like in hydrocarbon products), the change in their elemental content can be used to distinguish between the interfaces [12] and this can be achieved by gamma scattering technique. Some of the gamma scattering based level detectors reported in literature are mentioned in chapter I.

Measurement of concentration of minerals or fluids in body organs is very crucial for effective diagnosis and treatment of many diseases and gamma ray or X-ray transmission/scattering techniques are effectively employed for this purpose. The quantification of Bone Mineral Density (BMD) in trabecular or mandibular bones for the interpretation of osteoporosis [13-15], stable iodine content determination in tissue [16], characterization of tissue, fat and blood [17, 18] are some of the many areas in medical field where transmitted or scattered intensity is used [19]. Both gamma ray transmission and scattering techniques are used independently or in combination for the determination of soil water concentration [20, 21], frost concentration [22], moisture concentration in building materials [23], ash content in coal [8, 9] iron content in iron ore and in mine water treatment plants [24]. Determination of uranium concentration in solutions is highly desired in nuclear fuel fabrication and reprocessing plants and dual energy gamma ray transmission method (122 and 662 keV for low uranium concentration and 356 and 662 keV for high concentration) is utilized for this purpose [24]. The dependency of scattered photon counts on concentration in saline solutions was already established experimentally [25, 26]. The molar extinction co-efficient of amino acids having different concentrations was calculated from transmission experiment [27]. In all these applications it is required to monitor and determine very small changes in concentration.

The transmission method is more efficient when the transmission properties of the sample differ sufficiently. But there are many situations in medicine, industry, agriculture and food processing where there is a need of differentiating materials having nearby densities and composition consisting of elements which are neighbours in periodic table. The present chapter discusses the utility of scattering method in determining the interface level detection of immiscible fluid-fluid combinations and fluid-air combination enclosed in cylindrical glass tubes and quantifying the density or concentration of the solutions which are having closer attenuation parameters. The effectiveness and suitability of this method are discussed elaborately in this chapter. An intercomparison of the gamma scattering technique with the transmission method and the sensitivity and accuracy achievable by these techniques are also discussed. A unique nonlinear extrapolation method is described in detail to study the effects of multiple scattering and its correction.

4.2 Sample details

Two different sets of samples were used in the present study. The first set consist of biologically important solutions in different concentrations and second set consist of industrially important fluids having different but closer densities. The solutions of KI, NaCl, $C_6H_{12}O_6$ and K_2HPO_4 having closely lying density and attenuation co-efficient were prepared in varying concentrations (0 to 25 g in 100 ml for K_2HPO_4, NaCl and $C_6H_{12}O_6$ and 0 to 10 g in 100 ml for KI). KI solutions and K_2HPO_4 solutions in varying concentrations are used as the test phantoms for determination of stable iodine content in thyroid glands and for BMD quantification respectively. NaCl and $C_6H_{12}O_6$ are present in human body and they are used for food preservation also. The combinations of polar and non polar fluids like glycerine-olive oil, glycerine- castor oil and water- hexane were chosen for fluid level and density measurements. The densities of these selected fluids are hexane (0.651 g/cm^3), olive oil (0.8-0.9 g/cm^3), castor oil (0.96 g/cm^3), water (1 g/cm^3) and glycerine (1.26 g/cm^3).

The experimental set-up is shown in figure 4.1. The solutions were taken in a thin glass container having diameter 2.8 cm and placed on the job positioning system’s specimen disk located at a distance of 93.4 cm from the source and 52.1 cm from the detector. The scattering angle is 109º and 7 mm diameter collimators were used for both source and detector and the resulting voxel size is 49.53 cm^3. The incident and scattered photon energies are 661.6 and 243 keV respectively. The experiments were carried out by vertical scanning of solution container in steps of 1 cm and each voxel was scanned for adequate time (1000 s) to get enough counts with statistical uncertainty less than 2%. A combination of collimators 7 mm in detector and 5 mm in source and resulting voxel size of 27.5 cm^3 was used in fluid interface level determination for obtaining improved resolution and better accuracy. The thin glass container with castor oil (top) and glycerine (bottom) immiscible fluid combination with a well defined interface mounted on the specimen disk is shown in figure 4.1.

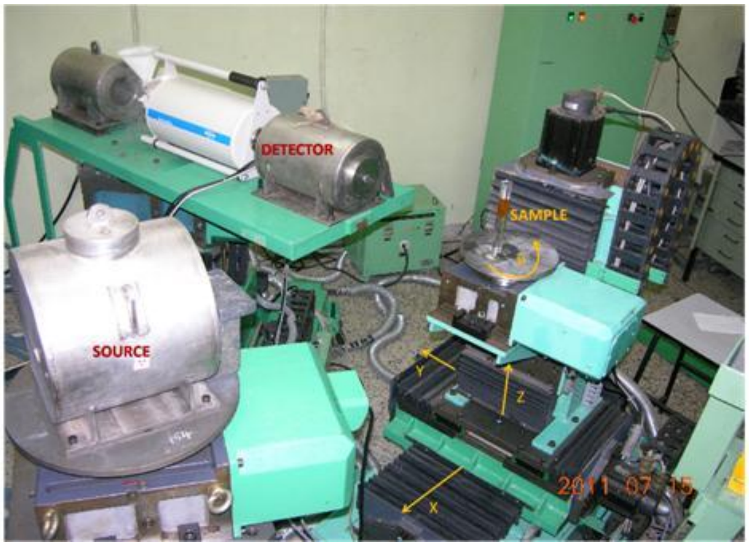

Figure 4.1 Experimental set-up with source, sample and detector labeled.

4.3 Multiple scattering

4.3.1 Scattering experiments

MCNP simulations have been carried out by incorporating the exact experimental geometry, sample parameters like density and concentration in to the modelling. The Pulse Height Spectra (PHS) are simulated using F8 tally and Gaussian broadening is provided using GEB card. The results of MCNP simulated PHS spectra are compared with those obtained by experiment. Figure 4.2 shows the spectra for water (left) and 15 wt % NaCl solution (right) and figure 4.3 shows the spectra for glycerine (left) and olive oil (right).

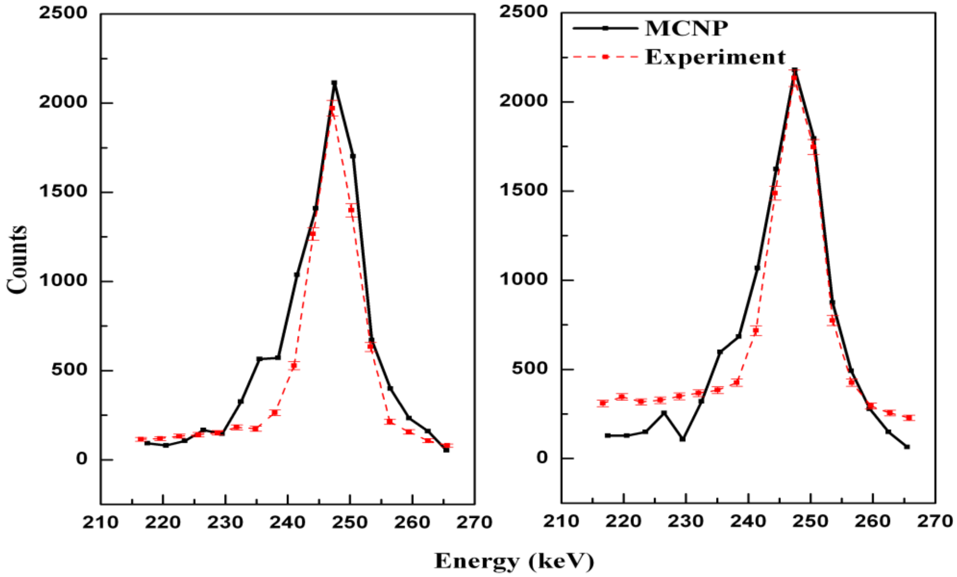

Figure 4.2 Comparison of MCNP spectra with experimental ones for water (left) and 15 wt % NaCl (right)

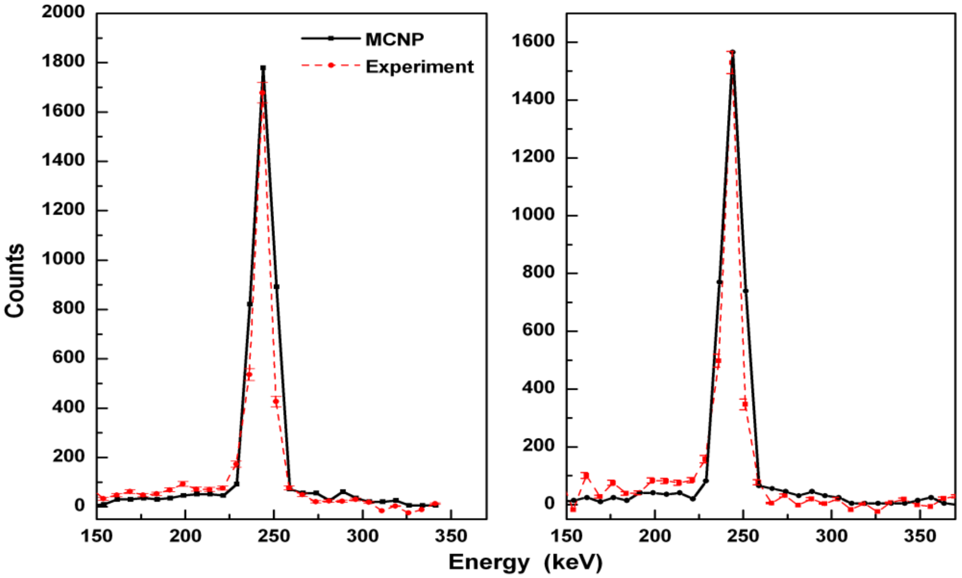

Figure 4.3 Comparison of MCNP spectra with experimental ones for glycerine (left) and olive oil (right)

A good agreement in the shape of the PHS is observed between the experimental spectra and those of MCNP simulated ones in all the four cases. Thus MCNP supports the experimental findings. MCNP simulated scattered intensities are used for calculating the multiple scattering contributions. The MCNP simulations are carried out for various concentrations of solutions for different scattering and transmission volumes by varying the axial thickness (t) of the sample. In the present study different t values are achieved by simulating cylindrical samples of varying radius x. Total scattered intensities (n_c) from different sample thicknesses within the present voxel and energy width ΔE are calculated from the area under the photo peak of corresponding spectra. The scattering volume ΔV inside the voxel is a function of axial thickness, t. The scattering volume is calculated following the method described in section 2.2.4.1. The scattered photon per electron, $n_c/\Delta V$ is calculated from the ratio of the number of electrons in the voxel to scattering volume and normalised with experimental value corresponding to axial thickness 1.4 cm.

The $n_c/\Delta V$ is plotted as a function of radius 'x', of the scattering volume. If no attenuation or multiple scattering effects are present a constant $n_c/\Delta V$ is expected but, a nonlinear reduction in scattered photons per electron is observed as a function of sample radius, x. A non linear function of the below form fits well to the data where A and B are the constants.

$$\frac{n_c}{\Delta V} = A\exp(-\mu\, x) + Bx \qquad (4.1)$$

Here μ is considered as the sum of the attenuation coefficients for incident and scattered photon energy i.e., $\mu = \mu(E) + \mu(E')$

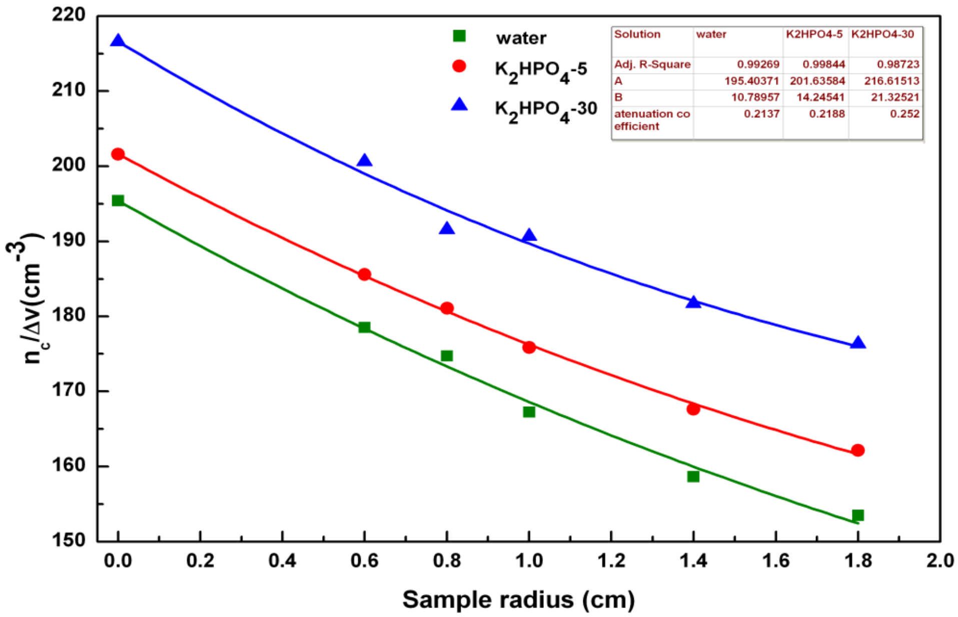

Solution	water	K2HPO4-5	K2HPO4-30
Adj. R-Square	0.99269	0.99844	0.98723
A	195.40371	201.63584	216.61513
B	10.78957	14.24541	21.32521
atenuation co efficient	0.2137	0.2188	0.252

Figure 4.4 $n_c/\Delta V$ as a function of sample radius for water, 5 wt % K_2HPO_4 and 30 wt % K_2HPO_4. The fitted curves with fitting parameters (inset table) along with extrapolated ones are shown.

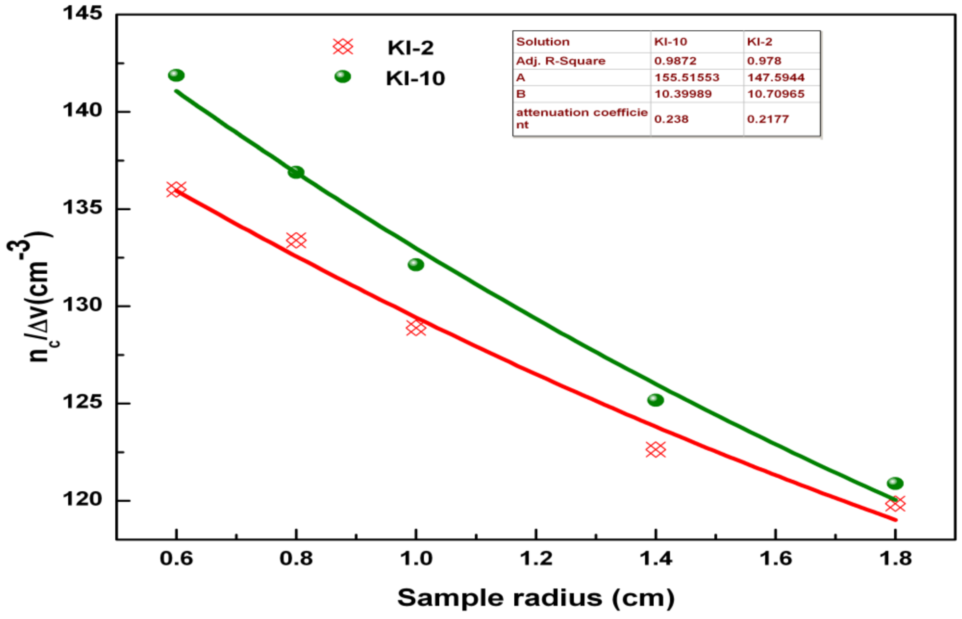

Solution	KI-10	KI-2
Adj. R-Square	0.9872	0.978
A	155.51553	147.5944
B	10.39989	10.70965
attenuation coefficie nt	0.238	0.2177

Figure 4.5 $n_c/\Delta V$ as a function of sample radius for 2 and 10 wt % KI. The fitted curves with fitting parameters (inset table) along with extrapolated ones are shown.

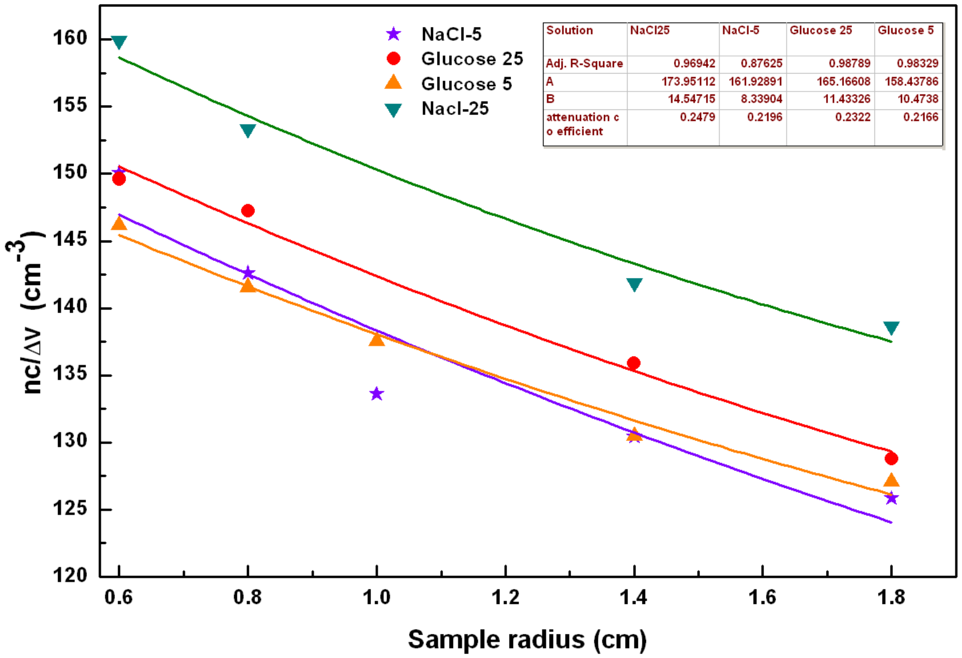

Solution	NaCl25	NaCl-5	Glucose 25	Glucose 5
Adj. R-Square	0.96942	0.87625	0.98789	0.98329
A	173.95112	161.92891	165.16608	158.43786
B	14.54715	8.33904	11.43326	10.4738
attenuation c o efficient	0.2479	0.2196	0.2322	0.2166

Figure 4.6 $n_c/\Delta V$ as a function of sample radius for 5 and 25 wt % glucose and NaCl. The fitted curves with fitting parameters (inset table) along with extrapolated ones are shown.

The figures 4.4, 4.5 and 4.6 show the fitted curves (eq. 4.1) for various solutions. The $n_c/\Delta V$ values plotted are obtained by normalizing the MCNP simulated intensities to experimentally obtained intensities at sample radius 1.4 cm. Since the n_c is resulted from a combination of attenuated and multiply scattered signals, a combined exponential and linear function is used for fitting the scattered intensities of different sample thicknesses. The fitted function has a linear term (Bx) corresponding to multiple scattering contributions and an exponential term for attenuation. The constant (A) obtained from the best fit is the extrapolated scattered intensity for zero axial thickness/radius and parameters (A & B) obtained from fitting and the R^2 values representing the goodness of the fit are shown. The nonlinear function used for fitting is a good approximation in the present mean free path range studied ($\mu t \leq 0.35$). The obtained R^2 values are tabulated in table 4.1 and which indicates the goodness of fit and appropriateness of the suggested relation. The extrapolated counts at zero axial thickness $\left(\frac{n_c}{\Delta V}\right)_{t=0}$ contains absorption corrected singly scattered component which directly depends on the solution density and hence on concentration. The ratios of these extrapolated counts to that of water are calculated. It may be mentioned here that Weyrich [28] used a semi empirical relation which proves a linear relation of multiple scattering with thickness in smaller μt region.

Solution	Concentration (wt %)	Density (g/cm^3)	Multiple to single scattering ratio	R^2 values
water		1	0.078	0.99
KI	2	1.015	0.102	0.98
NaCl	5	1.025	0.071	0.88
Glucose	5	1.026	0.089	0.98
K_2HPO_4	5	1.033	0.099	0.99
KI	10	1.062	0.094	0.99
Glucose	25	1.078	0.097	0.99
NaCl	25	1.097	0.111	0.97
K_2HPO_4	30	1.177	0.138	0.98

Table 4.1. Multiple to single scattering ratio calculated from the constants obtained from fitting for various solutions

The constant B of equation 4.1 obtained from the fit is related to multiple scattering and hence the multiple to single scattering ratio (S_m/S_1) for a given axial thickness (x) is calculated as:

$$\frac{S_m}{S_1} = \frac{B * x}{\left(\frac{n_c}{\Delta V}\right)_{t=0}} \tag{4.2}$$

where S_1 and S_m are the single and multiple scattering terms respectively.

The ratios S_m/S_1 given in table 4.1 varies from 0.071 to 0.138 and is a function of the material composition, effective atomic number (Z) and density of the solutions. A good agreement is seen in the same mean free path range with the values and trend of previous studies [29].

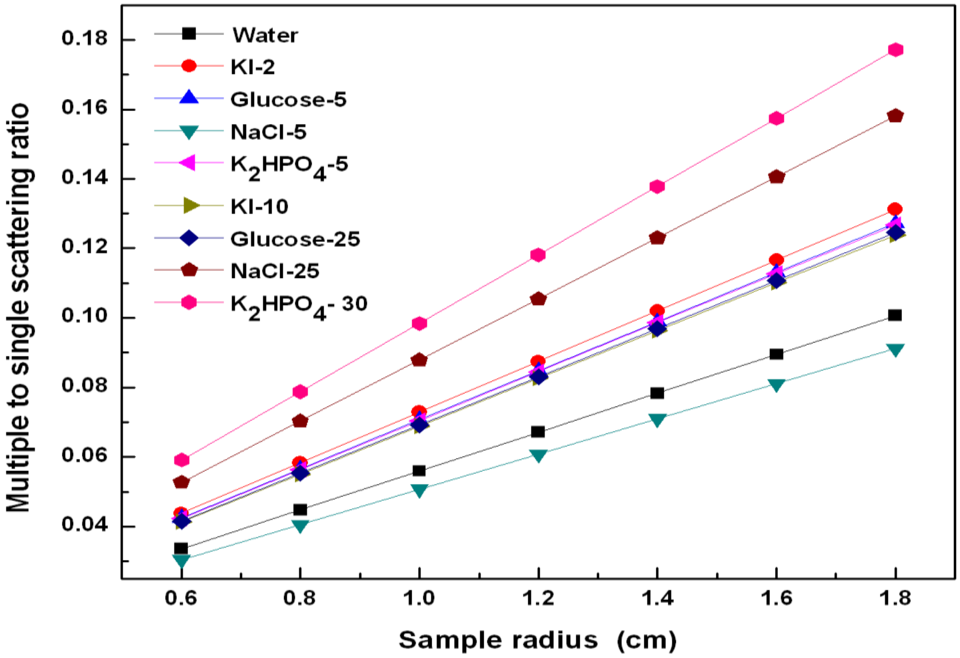

Figure 4.7 Multiple to single scattering fraction (S_m/ S_1) for various solutions as a function of radius of the sample

Multiple to single scattering ratio values for lower density solutions obtained are approximately same, whereas an increase in the values of multiple to single scattering ratio with density is observed for higher density solutions. A linear relationship between the sample radius and multiple to single scattering ratio is assumed in the fitting model.

According to this relation, multiple to single scattering ratio increases with sample radius as shown in the figure 4.7. A higher multiple to single scattering ratio is obtained with higher concentration for same thickness in accordance with table 4.1.

4.3.2 Transmission experiments

Multiple scattering contributions in transmission experiments are defined as build up factor. The attenuation coefficients derived from MCNP transmission simulations with different sample thicknesses are checked for the presence of multiple scattering in terms of build up factor. MC simulations have been carried out to calculate the effect of build up on the transmission results for two detector collimators (0.5 and 0.7 cm diameters) and for axial thickness of 30 wt % K_2HPO_4 solution sample varying from 2.4 to 4 cm corresponding to μt values 0.23 - 0.39. The gamma photon intensities received by the detector for each of these collimators are calculated from MCNP simulation. The attenuation coefficients are calculated from these simulated intensities and plotted as a function of sample thickness and the results are presented in figure 4.7. A constant value of attenuation co-efficient is expected for different sample thicknesses in the absence of build up due to scattered intensities. The present experimental values are relatively very close for axial sample thickness range of 2.4 to 4 cm. The linear attenuation coefficients vary from 0.0955 to 0.0967 cm^{-1} for measurements with 0.7 cm collimator and 0.0953 to 0.0962 cm^{-1} for measurements with 0.5 cm one. It can be seen from the figure 4.8 that the measured attenuation co-efficient of different thicknesses are reasonably constant and agrees well with the value computed using the XCOM program (0.0977 cm^{-1}) [30] within 2% and hence the present transmission results are free from multiple scattering contribution.

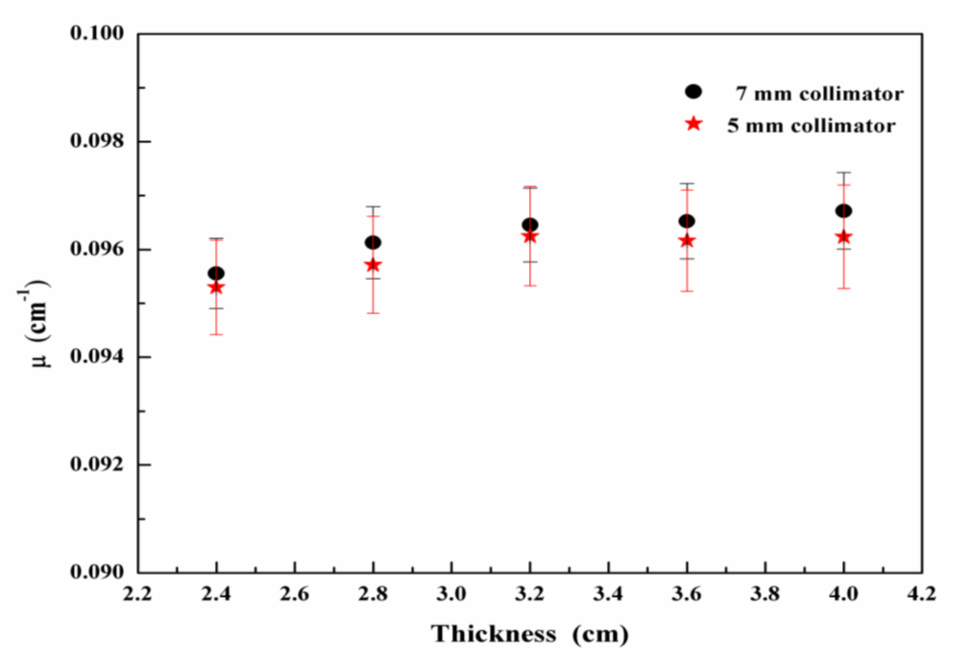

Figure 4.8 Transmission attenuation co-efficient obtained from MCNP simulations as a function of sample thicknesses for 0.7 and 0.5 cm detector collimators

4.4 Relative sensitivity

Both gamma transmission and scattering methods are sensitive to density variations. Therefore any variation in solution concentration and the changes in density will be reflected in both transmitted and scattered counts. The relative sensitivity for transmission and scattering methods depends on transmitted or scattered intensity of the sample and the reference sample [31]. The relative sensitivity in transmission method is calculated as,

$$\text{Relative sensitivity}_t = \frac{(I_{tw} - I_{tc})}{I_{tw}} \tag{4.3}$$

where I_{tw} and I_{tc} are the transmitted counts from water and solution (concentration, c) respectively. Similarly, the relative sensitivity in scattering method can also be calculated as

$$\text{Relative sensitivity}_S = \frac{(I_{SW} - I_{SC})}{I_{SW}} \tag{4.4}$$

where I_{sw} and I_{sc} are the scattered counts from water and solution respectively.

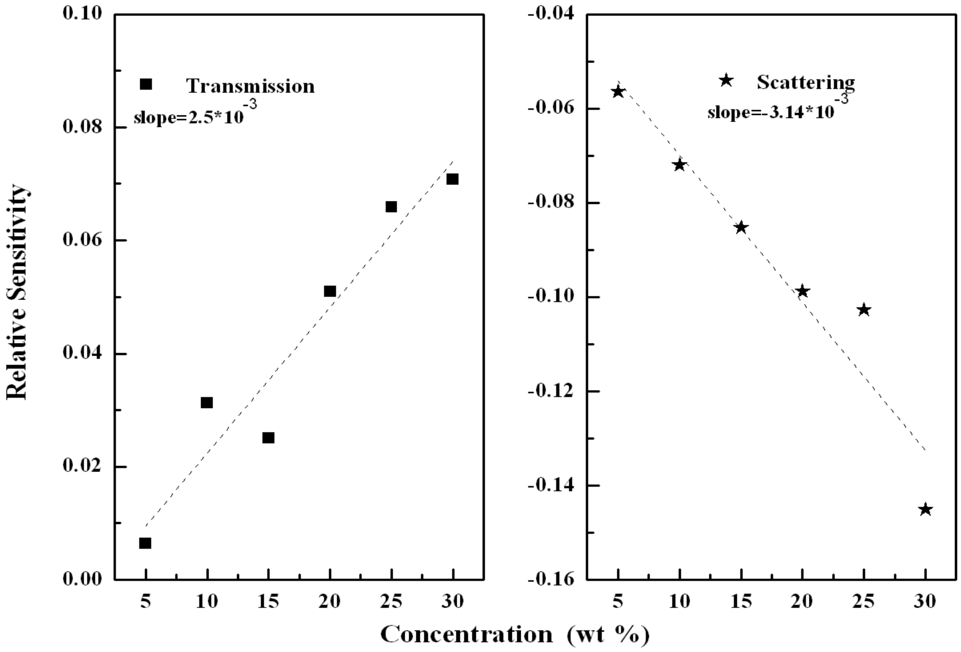

Figure 4.9 Relative sensitivity as a function of concentration in transmission (left) and scattering (right) methods for K_2HPO_4 solution

The relative sensitivity calculated by both transmission and scattering methods are plotted as a function of solution concentration and the results are presented in figure 4.9. The slopes (relative sensitivity/unit concentration) of these curves obtained are given in these figures. It can be observed that the slope for scattering curve is higher by a factor of 1.26 compared to that of transmission curve. Figure 4.10 shows the plot of relative sensitivity as a function of density and their corresponding slopes. In this case also higher slope is obtained for scattering method.

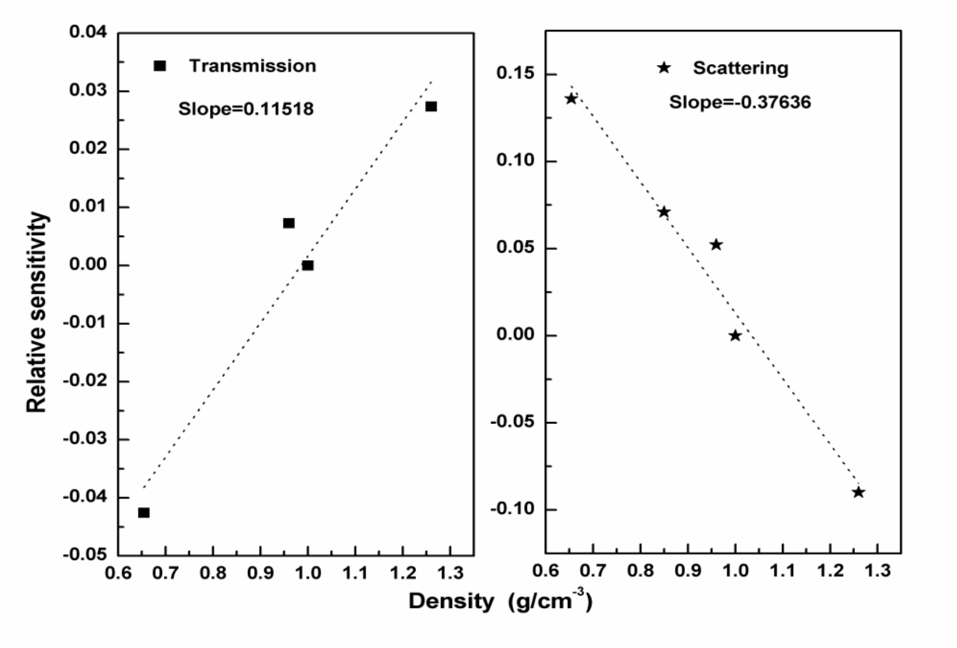

Figure 4.10 Relative sensitivity as a function of fluid density in transmission (left) and scattering (right) methods

Measurement sensitivity is the ratio of change in scattered or transmitted intensity between two different materials (absolute contrast) to the experimental error. Measurement sensitivity of transmission and scattering methods are as given below

$$\text{Measurement Sensitivity}_t = \frac{(I_{tw} - I_{tc})}{\sqrt{I_{tw}}} \tag{4.5}$$

$$\text{Measurement Sensitivity}_S = \frac{(I_{sw} - I_{sc})}{\sqrt{I_{sw}}} \tag{4.6}$$

The equations (4.5) and (4.6) obtained after assuming that statistical uncertainty is the only experimental error.

Measurement sensitivities of both transmission and scattering methods are calculated and tabulated in table 4.2. Same measurement error (statistical uncertainty) is considered for both transmission and scattering methods. Higher sensitivity (magnitude) is observed for scattering method compared to transmission method i.e., for same change in concentration or density, scattered intensity changes are higher compared to those changes in transmitted intensity.

Concentration of K_2HPO_4 (wt %)	Transmission sensitivity	Scattering sensitivity
5	0.649	-5.739
10	3.186	-7.319
15	2.547	-8.671
20	5.182	-10.046
25	6.706	-10.443
30	7.198	-14.750

Table 4.2 Measurement sensitivity of transmission and scattering technique as per equations (4.5) and (4.6)

A good sensitivity assures a large change in measured parameter (counts) even for a small variation in physical parameter (concentration or density) and sensitivity mainly depends on the difference in measured counts. Compton scattering cross sections are relatively high compared to photoelectric cross sections for the energy and for the solutions employed in the present investigation. Moreover, Compton scattered signal depends strongly and linearly on density of the scattering medium. The absorption is relatively less for thin samples ($\mu t<<1$) and low-Z solutions and hence change in transmitted intensity will be relatively small. Due to all these factors scattering technique yields better sensitivity compared to transmission method.

4.5 Fluid interface and level detection

The fluids interface levels of immiscible fluid combinations of olive oil-glycerine, castor oil-glycerine and hexane-water are measured by gamma scattering and transmission methods. These combinations of fluids are selected mainly because of their similar attenuation properties and densities. The measured counts as a function of vertical heights for all the above four fluid combinations are shown in figure 4.11.

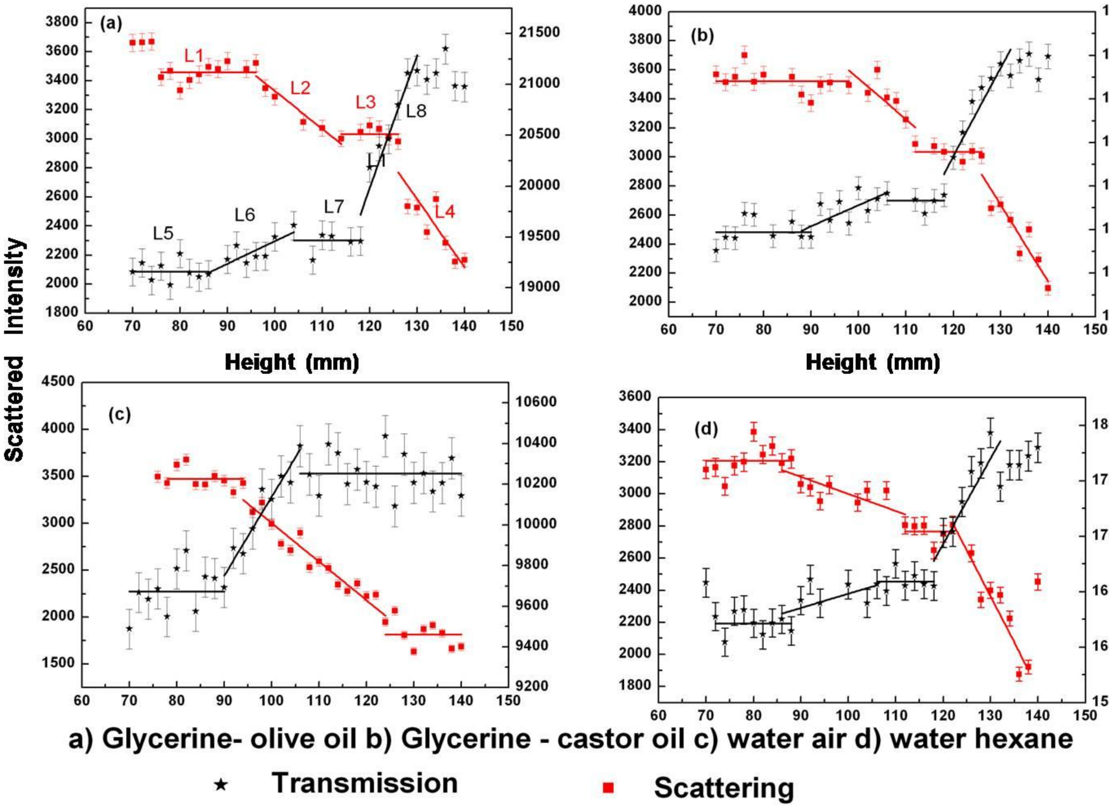

Figure 4.11 Measured transmitted and scattered counts as a function of vertical height of glass container

Any change in the scattered intensity/transmitted intensity indicates the change in fluid level, or change in the fluid density on the raster scanning. The different regions are shown in figure 4.11 and the fitted curve representing the constant/slope region is within the statistical uncertainties. The total scattered counts are same within the statistical uncertainties as long as the voxel is in high density fluid region of the immiscible fluid combination. This region is represented by (L1) in figure 4.11(a). As voxel moves towards the interface, the scattered counts decrease gradually due to the increased amount of contribution from low density fluid (L2). Again a constant scattered intensity region (L3) is observed as the voxel enters completely into the low density fluid. The slope region represented by L4 is the interface between low density fluid and air. An opposite trend is observed in transmitted intensities. A constant but low transmitted intensities are obtained (L5) for high density fluid region. As the voxel moves from high density to low density fluid, an interface with positive slope is obtained and the same is represented by L6. A constant but, higher transmitted counts are obtained in L7 region, which represents the low density fluid. Region represented by L8 is equivalent to L4 of scattered intensity profile. The selected regions for least square fitting of the scattered and transmission methods are different due to different voxel sizes in these methods. The midpoint of the fitted region is taken as the interface level and the measured interface levels from scattering method are closer to actual levels. The interface level representing the midpoint of the fitted region is not affected by the multiple scattering. This is due to the presence of almost same amount of multiple scattering in all the points used for fitting. From figure 4.11(d) water hexane combination have closer and smaller densities and hence a smaller slope in both transmission (12.891) and scattering (-10.699) is observed. Slopes of the interface region for glycerine-castor oil and glycerine–olive oil combinations i.e., fluids having almost similar density differences, are 22.355 and 24.258 respectively from transmission and -26.022 and -27.966 respectively from scattering. A much higher slope is obtained from both transmission (38.873) and scattering (-41.090) for water air combinations where density difference is more. From the above mentioned results, it can be stated that slopes obtained from scattering method are higher compared to those obtained from transmission.

The measured interface levels from scattering method are closer to actual levels and it can be seen from table 4.3 that the percentage deviations are higher in the case of transmission method compared to scattering method. Instead of following the fitting methods for determination of interface region, the same can be obtained by taking the derivative of the curve. When the voxel is in constant density region, a zero derivative is expected and deviation from this behaviour indicates the presence of interface region. The statistical uncertainties arising from the scattered/transmitted intensities are considered for calculating the error in the interface values.

		Scattering		Transmission	
Immiscible fluid - fluid combination	Actual level (cm)	Measured level (cm)	% deviation from actual level	Measured level (cm)	% deviation from actual level
Water-hexane	10.5	9.91±0.18	6.16	9.68±0.08	7.73
Glycerine-castor oil	10.5	10.61±0.19	1.18	9.81±0.07	6.55
Glycerine -olive oil	10.5	10.70±0.19	2.2	9.79±0.08	6.75
Water-air	10.5	10.82±0.21	3.32	9.71±0.10	7.55

Table 4.3 Immiscible fluid-fluid interface levels (measured from the bottom of the glass container) along with levels obtained from scattering and transmission methods

Transmission technique requires a radioactive source either inside the fluid or outside the container and the detector on the opposite side of the source. Transmission technique results in fewer gamma rays reaching the detector due to higher absorption in large containers and high fluid density. This limits the effectiveness of transmission technique in fluid density and interface measurements. Even though the neutron detection method is reliable for monitoring fluid interface, residual radiation will remain in the detected fluid because of the neutron activation. The complicated radiation shielding and high investment make this method not suitable for large scale applications. The back scattering technique has the advantage of one sided source and detector arrangement enhancing reasonable counts at the detector even in dense fluids and larger containers. Thus the scattering technique can be used effectively for interface level detection of fluids with closer densities and attenuation parameters, high density fluids and large size containers. Since any deviation in scattered intensity will attribute to change in fluid i.e., interface, the back scattered mode can function in both switch on/off and continuous mode. The switch on/off mode is used in determining whether the fluid is above or below a certain level by keeping the source and detector fixed, while the continuous mode is used for continuous level investigation by the movement of source detector assembly. Scanning duration depends on the strength and energy of gamma source and, the density and composition of the fluid. In the present experimental set-up it takes 400 s counting time for obtaining scattered intensity with less than 3% uncertainty. This time can be reduced by increasing either the voxel size or source strength and by compromising on the statistical accuracy.

The scattered intensity of glycerine-olive oil column for various measurement times are plotted in figure 4.12. It is observed that a clear indication of interface can be obtained within 60 s per voxel scanning. As measurement time increases the interface becomes clearer.

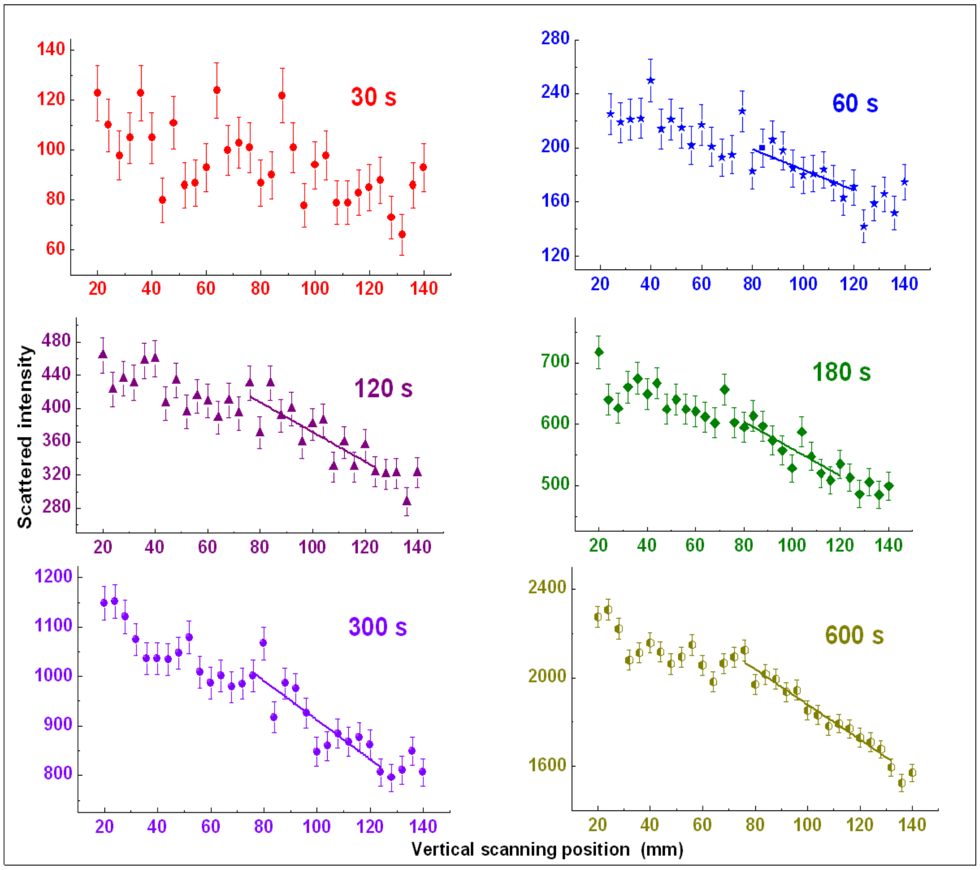

Figure 4.12 Scattered intensity profile of glycerine olive oil column for various durations

4.6 Attenuation correction and surface imaging

Since the scattered intensities are affected by attenuation of both incident and scattered photons, attenuation correction is required to account for the same. Prior knowledge of the composition of the object is required for this purpose [32] and the same is simulated. The test sample is simulated by assigning to each grid (pixel) attenuation co-efficient corresponding to incident gamma energy. The path length dl in each pixel is obtained from the angle formed by incident gamma photon to the normal of the object and the co-ordinates of scattering point. Each path length dl is multiplied by the corresponding pixel value (μdl). Total incident attenuation correction is calculated by exp (∑μdl) over the path length. The total scattered attenuation correction is also calculated using same method by assigning the attenuation co-efficient corresponding to scattered energy as pixel value and calculating scattered path. The attenuation corrected scattered count is given by:

$$I_{corr} = I_s \ \exp\left[\sum \mu dl\right] \exp\left[\sum \mu' dl'\right] = K\ \rho \qquad (4.7)$$

The corrected scattered count is having a direct proportional relation with the density. In the present study, the standard density is used to calculate the attenuation function and this demands the uniformity of the material within the pixel. The figure 4.13 shows the image of simulated sample and incident and scattered paths used for calculating correction factors.

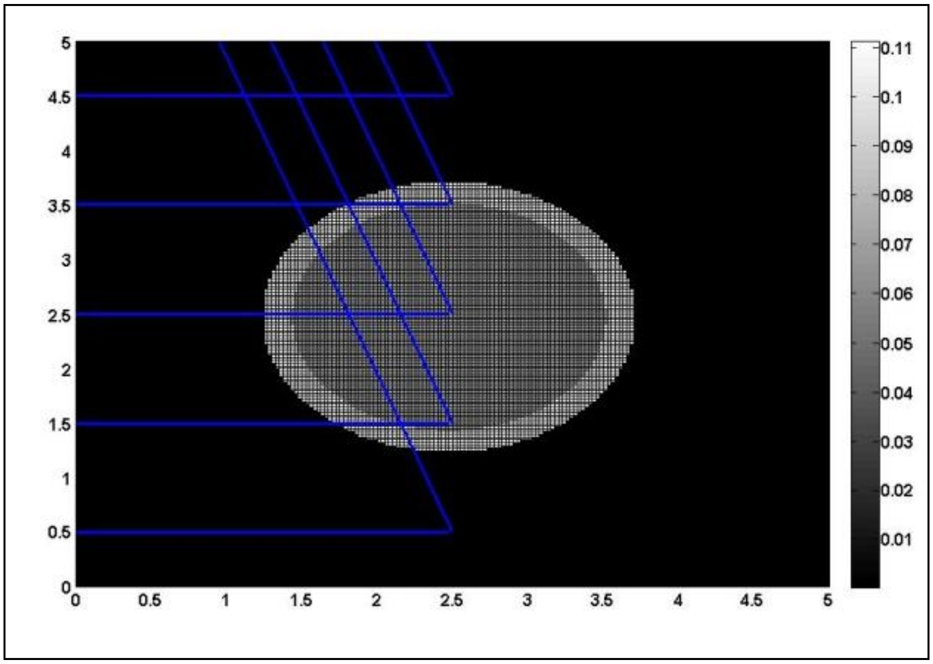

Figure 4.13 Image of the simulated sample with both incident and scattered paths are shown

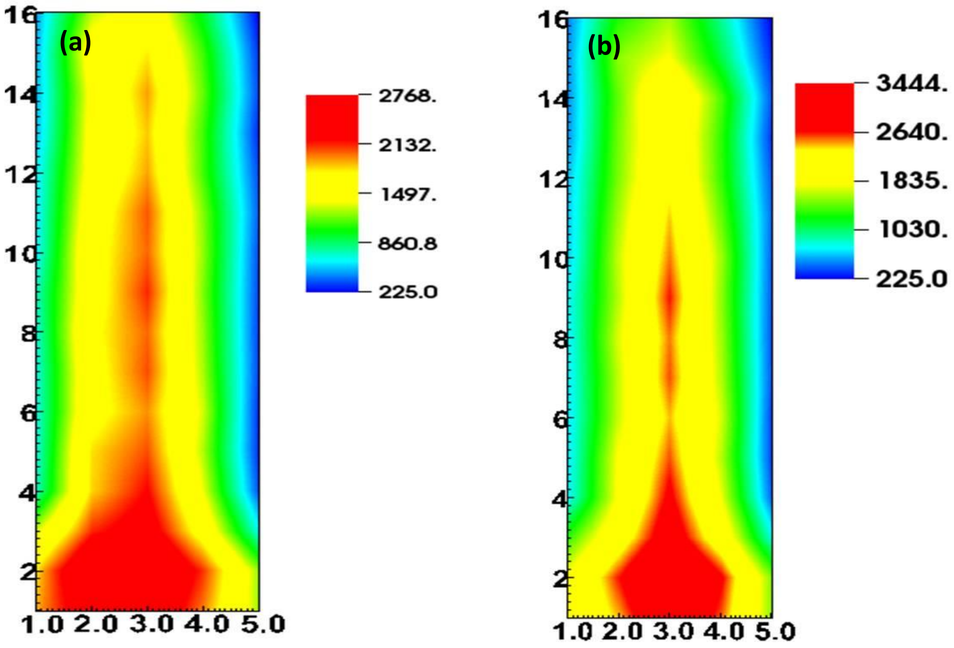

Figure 4.14 Surface image of water hexane column from raw counts (a) and attenuation corrected counts (b)

Figure 4.14(a) and figure 4.14(b) show the images of water–hexane combination obtained from raw scattered counts and the attenuation corrected ones respectively. The attenuation correction enhances the contrast of the images and the water–hexane interface becomes clearly visible and the blue and green regions in the figure represents air column. Red and yellow regions represent the fluids and the container regions. The same combinations of fluids enclosed in Stainless Steel (SS) cylindrical container of 0.025 m diameter and 0.002 m thickness and PVC cylindrical container of 0.025 m diameter and 0.0015 m thickness are also scanned individually. Figure.4.15 shows the images obtained from attenuation corrected counts of glycerine–castor oil, glycerine–olive oil and water-hexane combination in PVC, SS and glass pipes. The attenuation through the different container material is also taken into consideration while reconstructing these images. This shows that these measurements can be done in any container materials without sacrificing the sensitivity by applying suitable attenuation corrections.

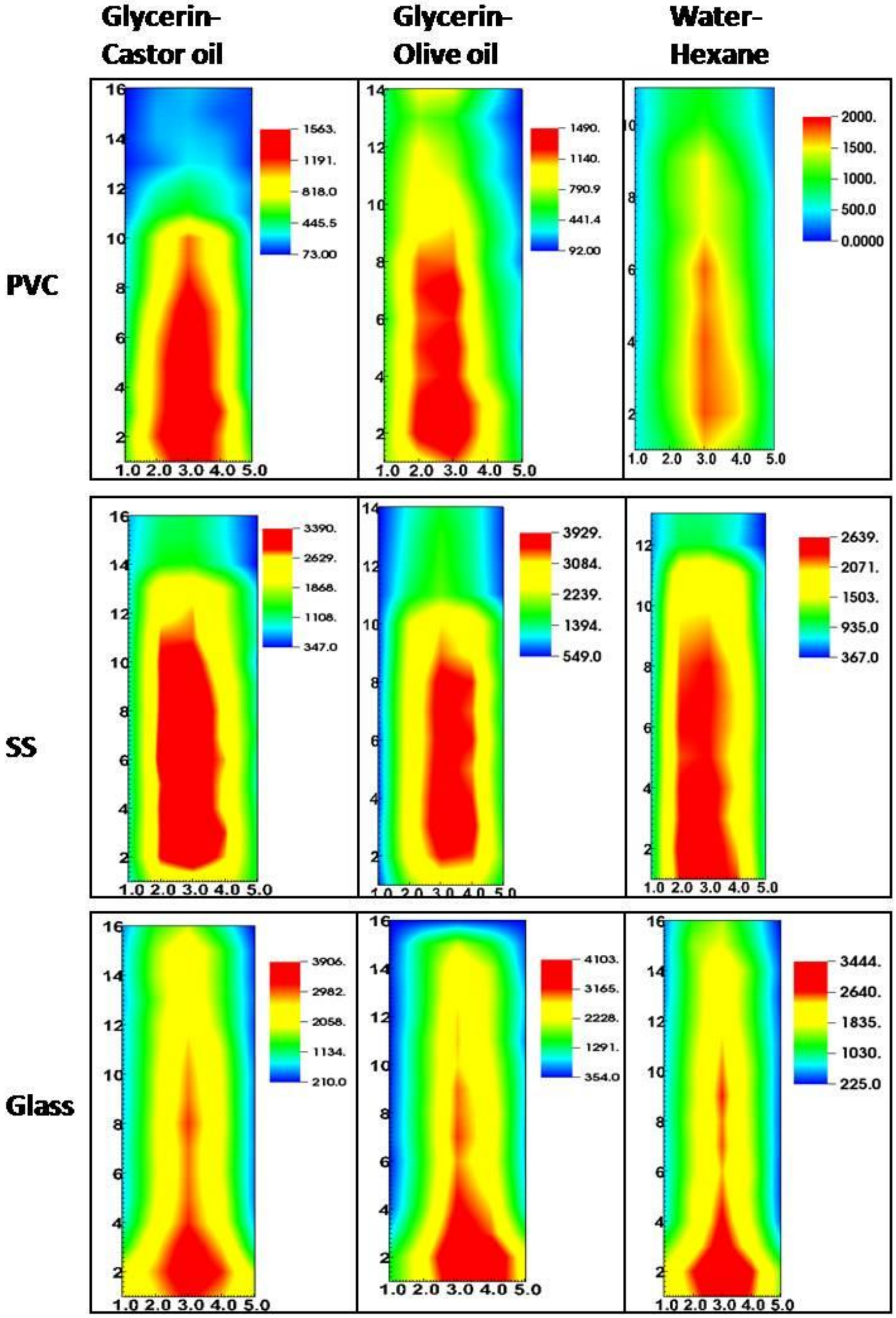

Figure 4.15 Scattered attenuation corrected images of various immiscible fluid combinations in different containers

Since the extrapolated scattered intensity is free from attenuation and multiple scattering effects, it is directly related to sample density. Hence the ratio of the corrected counts (extrapolated ratio) of solutions and water is calculated to obtain the ratio of their densities. In order to verify this point, experiments were carried out using the samples described in 4.2.

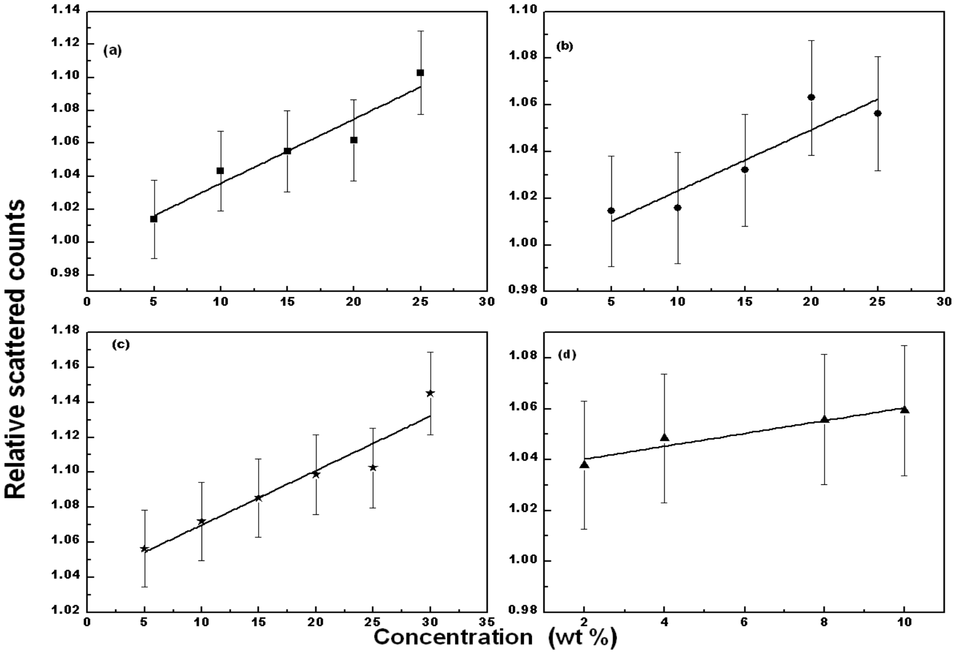

Figure 4.16 Relative scattered counts (solution/ water) for varying concentrations of (a) NaCl, (b) $C_6H_{12}O_6$, (c) K_2HPO_4 and (d) KI respectively

The scattered photo peak counts from solutions of different concentrations are obtained from the pulse height spectra. The contribution from container glass material was determined by doing experiments with empty container and subtracted from the sample spectra. The scattered count ratios of the solution to water are plotted as a function of concentration and are shown in figure 4.16. An increase in scattered intensity with increase in concentration is observed and a good slope of this curve shows the sensitivity of this method for determining the small differences in concentration of solutions. Statistical uncertainty is represented by the error bar. A straight line fit within the error bar indicates the linear dependence of scattered intensity with concentration.

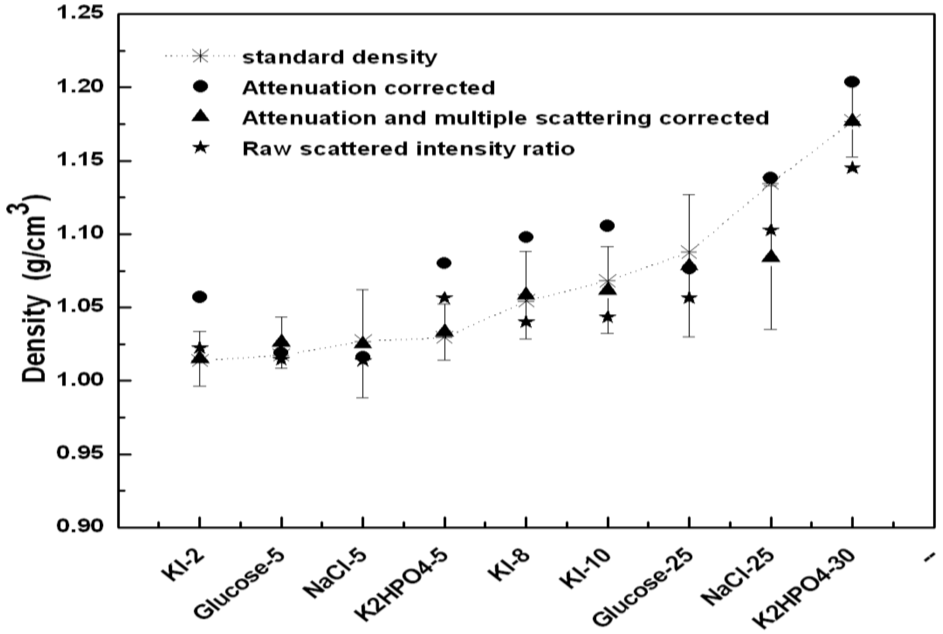

Figure 4.17 Densities obtained by i) non-linear extrapolation method correcting for attenuation and multiple scattering ii) from raw scattered intensity ratio and iii) by attenuation correction only for various solutions are compared with the standard densities

The solution densities obtained from the ratio of extrapolated counts of solutions to that of water are shown in figure 4.17. Densities obtained from ratio of raw scattered intensities of solution and water and by applying suitable correction only to self absorption are shown in figure 4.17. The extrapolated scattered intensity values obtained from fitting using equation (4.1) are free from self absorption and multiple scattering. Therefore, the density ratios obtained using these values agree well with the standard ones within experimental errors. At lower densities, the values obtained by direct ratio method are also found to be in agreement with the standard densities and this is because both attenuation and multiple scattering effects are approximately same for solution and reference sample (water) and cancel out each other. But as density increases, values obtained by direct ratio method deviates from the standard values due to the predominance of multiple scattering and self-absorption factors of solutions compared to reference sample (water).

Since density of the solution depends upon the weight percentage of the solute, the concentration can be calculated from the measured density ratios. The concentrations obtained from the non-linear extrapolation method are given and compared with those of standard ones in table 4.4.

Solution	Prepared concentration (wt %)	Obtained concentration from extrapolation method (wt %)
KI	2	2.22±0.03
NaCl	5	4.68±0.13
K_2HPO_4	5	5.64±0.02
KI	8	8.61±0.04
KI	10	9.11±0.18
Glucose	25	22.33±0.19
K_2HPO_4	30	29.99±0.33

Table 4.4 Concentration of solutions derived from the densities obtained by scattering method

The densities of samples of importance in industry are determined by scattering and transmission methods following the same procedure. Multiple scattering factors are calculated using the non linear extrapolation as shown in figure 4.18 and found to be in 10% range for sample of radius 1.4 cm

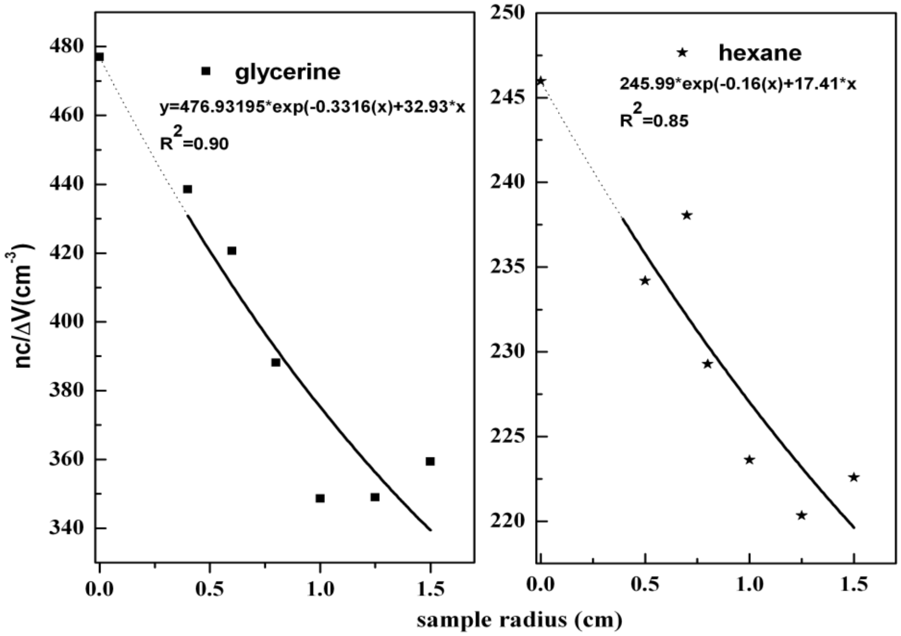

Figure 4.18 $n_c/\Delta V$ as a function of sample radius for glycerine (left) and hexane (right). The fitted curve (inset equation) along with extrapolated ones is shown

The multiple contributions are approximately same for fluids (first set) studied and reference sample water. Hence, even if the multiple scattering contributions are not taken into account, the effect will get cancelled out while calculating the densities with reference to a sample (water). The densities obtained from extrapolated ratios with respect to that of water are also in good agreement with the standard ones. The densities of various fluids with reference to that of water are obtained from the experimental scattered counts corrected for attenuation employing equation (4.7) and are shown in figure 4.19. The errors resulting from estimation of geometrical parameters and cross sections are eliminated in the density calculation by taking the ratio of measured scattered intensities in the same geometrical set-up with respect to water sample. The total uncertainty in the derived density is around 3% and can be further reduced by minimizing the statistical uncertainties associated with measured scattered intensity. Densities obtained by scattering experiments show good agreement with that of standard values in comparison with the densities obtained by transmission experiments.

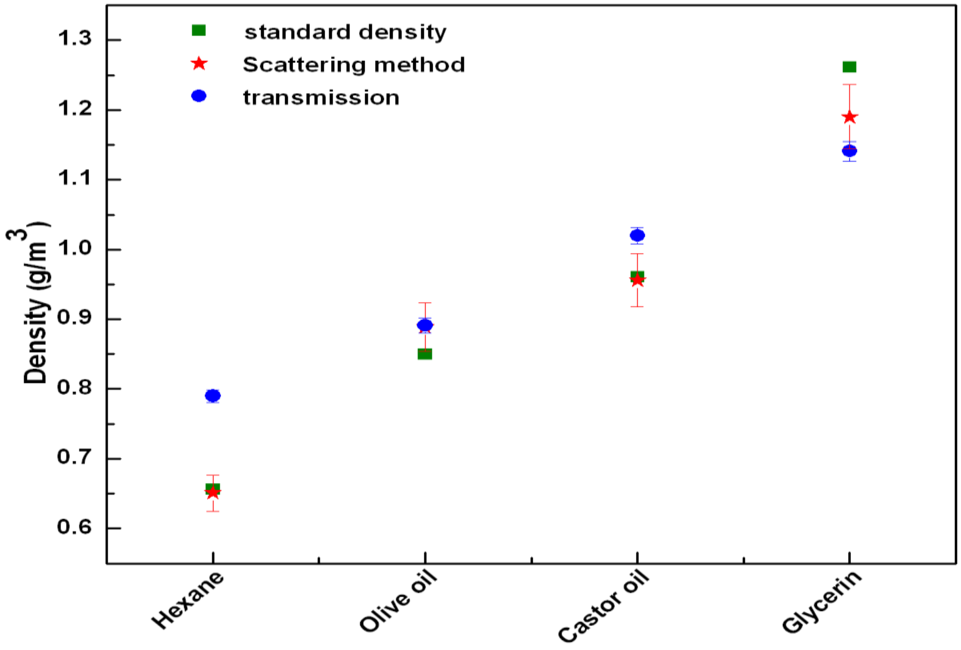

Figure 4.19 Comparison of densities of fluids obtained from scattering and transmission methods with the standard densities

Higher sensitivity is obtained in scattering technique than transmission technique for density and concentration variations. Accuracy in quantification of density is also superior in the case of scattering technique than transmission technique for the selected low dense, low atomic number solutions having similar attenuation properties. The potential of scattering method is proven for obtaining the low-Z solution density/concentration. The goal of accurate concentration determination for low-Z solutions can be achieved due to higher sensitivity of the scattering technique over transmission one along with proper corrections for multiple scattering and self absorption. The measured fluid interface levels from scattering method are closer to actual levels and the percentage deviations are higher in the case of transmission method compared to scattering method. The main advantages of the scattering method as compared to other techniques are the ability to detect fluid-fluid and fluid-air interface levels with better accuracy and resolution without the need for all-round access and the contact with the sample under investigation and the possibility to inspect a chosen volume or point.

References

1. Ahmad, S.R., Reynolds, D.R., Wat. Res., 33 (1999), 2069-2074
2. Kivenson, G., U.S. Patent 4157036 (1979)
3. Libby, W.F., Annu. Rev. Nucl. Sci., 11.(1961), 461-482
4. Carlson, N.R., Rosener, R.E., Lanuke, E.W., U.S. Patent 4441361 (1984)
5. Wolf, A., U.S. Patent 2456233 (1948)
6. Stokes, J.A., Alvar, K.R., Corey, R.L., Costello, D.G., John, J., Kocimski, S., Lurie, N.A., Thayer, D.D., Trippe, A.P., Young, J.C., Nucl. Instrum. Methods, 193 (1982), 261-267
7. Bruvik, E.M., Hjertaker, B.T., Hallanger, A., Flow Meas. Instrum., 21 (2010), 240-248
8. Watt, J.S., Int. J. Appl. Radiat. Isot., 34 (1983), 55-62
9. Gravittis, V.L., Watt, J.S., Zastawny, H., Int. J. Appl. Radiat. Isot., 36 (1985), 879-887
10. Charlton, J.S., Radioisotope Techniques for Problem solving in Industrial Process, Charlton, J.S., (Ed), Glasgow, Leonard Hill, (1986), 204-246
11. Edmonds, E A, Radioisotope Techniques for Problem solving in Industrial Process, Charlton, J.S., (Ed), Glasgow, Leonard Hill, (1986), 247-268
12. Hussein, E.M.A., Hand book on Radiation probing and imaging Vol 2, First edition, Springer (2003)
13. Clark, R.L., Van Dyk, G., Phys. Med. Biol., 18 (1973), 532-539
14. Olkkonen, H., Karjalainen, P., Brit J Radiol., 48 (1975), 594-597
15. Webber, C.E., Kennett, T.J., Phys.Med.Biol., 21 (1976), 760-769

16. Puumalainen, P., Sikanen, P., Olkkonen, H., Nucl. Instrum. Methods., 163 (1979), 261-263
17. Shakeshaft, J., Morgan, H.M., Lillicrap, S.C., Phys .Med. Biol., 42 (1997), 1403-1413
18. Poletti, M.E., Goncalves, O.D., Mazzaro, I., Phys .Med. Biol., 47 (2002), 47-63
19. Elshemey, W.M., Elsayed, A.A., Ali El-Lakkami, Phys .Med. Biol., 44 (1999), 2907-2915
20. Soane, B.D., Campbell, D.J., Herkes, S.M., J.agric.Engng. Res., 16 (1971), 146-156
21. Cruvinel, P.E., Balogun, F.A., Eng. Agric. Jaboticabal., 26 (2006), 151-160
22. Bong, T.Y., Wijeysundera, N.E., Saw., E.L., Lau., K.O., Exp. Therm. Fluid. Sci., 4 (1991), 567-576
23. Bucurescu, D, Bucurescu, I, Rom. Rep. Phys., 63 (2011), 61-75
24. Watt, J.S., Steffener, E.J., Int.J.Appl.Radiat.Isot., 36 (1985), 867-877
25. Gayer, A., Bukshpan, S., Kedem, D., Nucl. Instrum. Methods, 192 (1982), 619-621
26. Guang, L., Shang-Qi, Z., Zhong, H., Shuang-Kou, C., Chinese J. Chem., 25 (2007), 164-167
27. Singh, K., Sandhu, G.K., Kaur, G., Lark, B.S., J Radioanal Nucl Ch., 253 (2002), 369-373
28. Weyrich, W., Ber. Bunsen. Phys. Chem., 79 (1975), 1086-1095
29. Das G., Panda B K., Mahapatra D.P., Padhi H.C., phys.stat.sol.(b), .149 (1988), 355362
30. Berger, M.J., Hubbell, J.H., NBSIR 87-3597, MD 208991987
31. Harding G., Radiat. Phys. Chem., 50 (1997), 91-111
32. Balogun F.A., Spyrou N.M., Nucl. Instrum. Meth. B, 83 (1993), 533 -538

Chapter V Non destructive characterization of concrete for the detection of inclusions and voids and estimation of water content

5.1 Introduction

The primary purpose of nuclear power plant containment is to prevent the release of fission products to the environment in the case of an accident and to provide a shielding under normal operation. Materials having good attenuation properties for both gamma rays and neutron are preferred for this purpose and concrete is the most favoured material due to its high gamma and neutron attenuation co-efficient. It is more effective for neutron shielding because of its low atomic number and presence of hydrogen. Moreover, concrete is relatively cheap and easy to prepare in any form [1]. Concrete is a combination of cement, water and small aggregates mainly sand. The most common defects present in concrete are internal cracks, voids, shallow delamination, honeycombing and surface opening cracks. Detection of defects before it’s propagation to the point of causing failure is very essential for ensuring the structural strength. In the case of reinforced concrete structures, thickness variations due to corrosion, presence of voids and positions of the inclusions such as reinforcing bars, and steel liners are also to be monitored.

Some of the above stated defects such as cracks and corrosion are initiated by the water content variation in concrete. Only part of water added in the mixture will be used for cement hydration. Rest of the water will be present in the capillary pores of the concrete either as gel water which is absorbed or physically bound in gel pores or as free water in capillaries. Even though gel water has lower mobility than free water, no distinction is possible among them. Hence water content in concrete can be of evaporable (gel water and free water) or non-evaporable (chemically bound water) [2]. The shielding effectiveness can be maintained by high non evaporable water content and minimized evaporation of free water. But due to weather conditions such as heat, humidity etc. and inherent porosity, water content in concrete will slowly decreases as a function of time. Drying of concrete will result in free water to escape from capillaries and shrinkage of cement part to compensate the change in surface energy. Uneven moisture formation will lead to uneven shrinkage and which can create cracks. As humidity increases, both gel water and free water increases, which will assure a high neutron shielding. At the same time higher water content can act as a transporting medium of chlorides and other chemicals to interior of concrete to act as a catalyst for corrosion. The concrete durability is influenced not only by the moisture content but also, significantly by the moisture distribution in the concrete specimen. Hence the knowledge of moisture content as a function of time and position allows one to extract information on the permeability of the porous body. Monitoring the water content in concrete and its profile is of higher importance in assuring the strength and durability of any concrete structures.

5.1.1 Radioactive methods for concrete NDE

A particular area of interest for NDE techniques is detection of defects in concrete structures and moreover, NDE techniques are useful for condition assessment of concrete structures. Electrical and magnetic methods, ultra sonic technique, acoustic emission, microwave absorption, impact echo, ground penetrating radar, and nuclear (radioactive) methods are the main NDE methods for concrete. Many detail review and articles on historic evolution of these NDE techniques are available in literature [3-7]. In the case of reinforced concrete structures, these techniques are expected to provide information about thickness variations as well as the position and presence of inclusions such as the reinforcing bars, cracks, voids and delamination, deteriorated zones and moisture. Each of this technique has its own advantage and disadvantages. For example, in the case of moisture content determination gravimetric, electrical and micro wave absorption methods cannot be used to detect the localised moisture content [8]. Nuclear magnetic resonance technique is having high accuracy and spatial resolution but it is less sensitive to bound water content and can be used in small samples only. Neutron radiography is highly sensitive to the water content due to the direct interaction of neutron with hydrogen, yet the experimental data are affected highly with experimental noises [9]. Techniques such as ultrasound and radiography generally provide only qualitative information. Hence, they are not practical for measuring the dimensions of structure, mapping density distributions, or for precisely locating, orienting and sizing the defects. In addition, the complex geometry of the concrete structure, restricted accessibility, and presence of reinforcement and prestressing tendons further complicate the problem. The goal of any NDE technique is to detect and locate the anomalies with in an optically opaque concrete medium through appropriate imaging techniques.

Imaging of concrete structures is very important due to the aging and deterioration of infrastructures [10]. NDE of concrete structures through imaging presents many challenges, since concrete is a non-homogeneous composite material having variable grain size distribution and properties of each constituent materials are different. Imaging can be achieved using techniques such as radiography, Computerized Tomography (CT), infrared thermography, radar imaging and acoustic imaging. Radiography can be used to locate internal defects and reinforced rebars position in concrete through differences in radiation intensity passing through the structure that is captured on photographic film placed on the opposite side of the structure from the source. CT is a method that permits the development of three-dimensional radiograph views of an object. The degree of damage in concrete structures can be assessed using high resolution three dimensional images obtained from CT technique. To obtain a three-dimensional image, it is necessary to have several different views, and this may not be possible in the field.

Radioactive methods for testing concrete are potentially attractive due to its high accuracy and speed. But, complex structures due to shielding requirement, high initial investment and licensing requirements make these methods less popular. A detailed review of radioactive methods used to study concrete is given by Terry W. Mitchel [11]. Nuclear or radioactive methods used for non destructive evaluation are classified into three categories as radiometry, radiography and neutron gamma method. In radiometric method, a source and detector are placed either on the same side or on the opposite side of the concrete sample. The detected intensity is processed to quantify dimensions and physical parameters like composition and density. In radiography method, source and photographic film are placed on the opposite sides of the sample and the image of the sample under investigation is developed. This technique is effective in detecting and locating the defects. In neutron-gamma method, the sample is irradiated with neutron source and the emitted gamma photons are detected. This method is very effective to determine the composition of the concrete sample. Compared to the gamma photons, X-ray photons have low energy and smaller penetration ability. Hence the concrete thickness that can be tested using X-ray radiography is limited.

The various applications of gamma radiometry method in concrete testing for density, thickness and density variations are listed in a review article written by Malhotra [6]. According to this review, Smith and Whiffin [12] introduced the use of gamma radiometry in concrete testing methods. Gamma radiometric method is a well established technique to estimate whether the newly poured concrete meets the strength requirements by monitoring consolidation during construction [13]. Radiometric methods are useful for quality testing of concrete and research and development also. Radiometric techniques are utilized for thickness [14], density [9, 15] and density variation [16] measurements. Radiometric methods can be either in transmission or scattering mode.

Gamma scattering and attenuation properties of concrete are explored in the gamma scattering technique and this technique can be effectively used for thick, extended, two sided access restricted and in-place concrete structures. This technique has been effectively used to detect hidden defects in aluminum blocks and concrete block by many researchers [17-31]. Gamma transmission technique is a well-established method for water content determination compared to gamma scattering technique which is still not investigated in detail. Moisture content estimation using gamma scattering technique have been carried out earlier and the results were based on the relative change in Compton continuum counts [32] and the Rayleigh to Compton scattering ratio [33].

The present work is about the reconstruction of three dimensional images of the sample to detect and quantify the defects in the extended concrete blocks and to estimate the water content in concrete by gamma scattering technique. Water content results obtained from gamma scattering methods are compared with the conventional gravimetric and transmission methods. An improved version of algorithm prescribed by Battista et al. is developed and adopted for the attenuation correction and image reconstruction [34]. This algorithm is based on the point to point scanning method and this avoids the need for multiple detectors and rotation of the sample and it can facilitate for any scattering angle.

5.2 Detection of embedded inclusions in concrete blocks

5.2.1 Sample details

The concrete samples utilized in this study, are made using cement type Portland-CP-II, fine natural sand, coarse aggregate with small diameter and water. Two concrete samples embedded with voids were chosen for void detection and quantification and they are shown in figure 5.1.

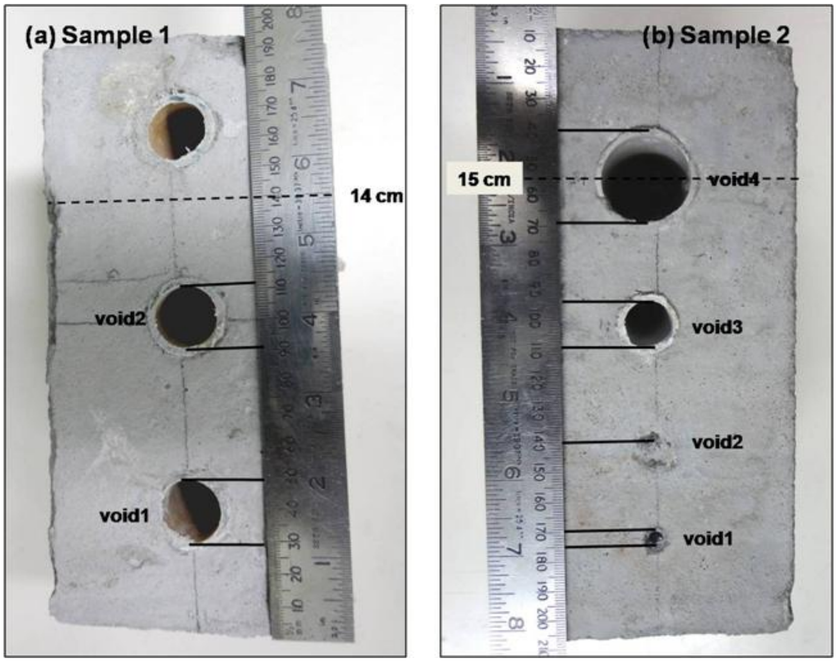

Figure 5.1.Concrete samples ((a) sample 1 and (b) sample 2) embedded with voids

Sample 1: concrete block of size 10 × 10 × 20 cm^3 embedded with three air cavities of diameter 2 cm and depth 4.5 cm.

Sample 2: concrete block of size 10 × 10 × 20 cm^3 embedded with 4 air voids of diameters 0.5, 1, 1.5 and 3 cm placed at 2.5 cm away from two ends of concrete with a spatial distance of 3 cm. Three voids in sample 2 (0.5, 1.5 and 3 cm diameters) are visible and the fourth one (1 cm diameter) is hidden from the surface by a thin layer of concrete.

5.2.2 One dimensional profiles for locating the voids

Two sets of sequential scanning along the vertical height (Z) are performed employing two voxels of size 12.9 cm^3 (small voxel) and 49.5 cm^3 (large voxel) on sample 1 to obtain the locations of voids. Figure 5.2 shows the one dimensional scattered intensity profile of sample 1 as a function of the vertical height.

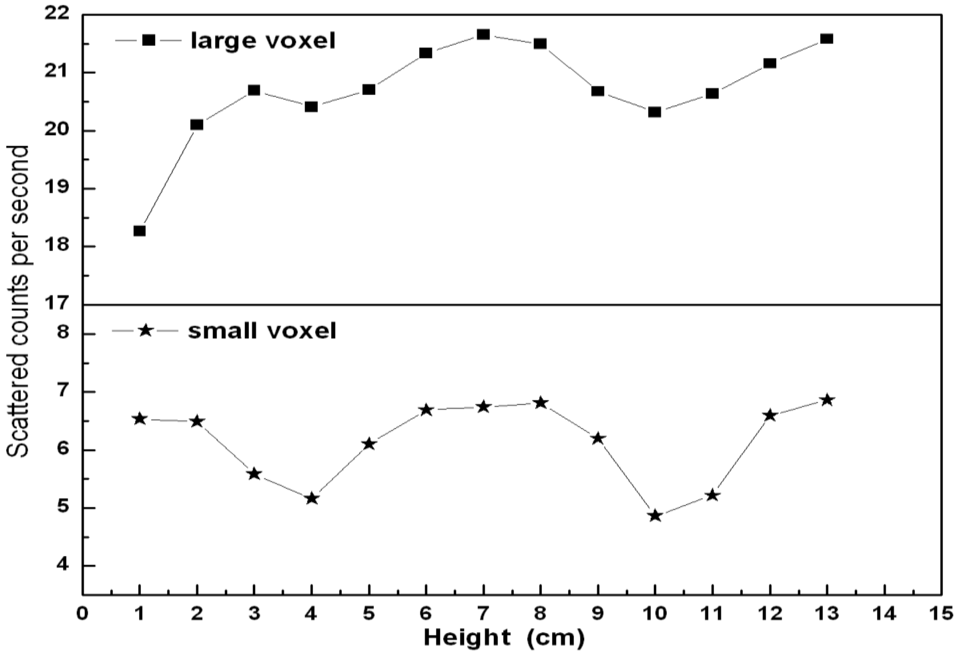

Figure 5.2 One dimensional scattered intensity profile as a function of vertical height for large and small voxel sizes

Both the large and small voxel scanning show a dip at the same positions (4 cm and 10 cm). The void locations obtained experimentally are in agreement with figure 5.1(a).

Relatively better spatial resolution is obtained for smaller voxel size compared to larger one. Higher spatial resolution in the case of smaller voxel is due to lesser overlapping of adjacent voxels. The relative contrast of 28.54% and 6.15% is obtained between the void and concrete phases for the smaller and larger voxel sizes respectively. Because of its higher contrast and superior resolution, smaller voxel size is selected for further detailed scanning of the samples 1 and 2, even though it requires longer scanning time compared to larger voxel size to obtain the same statistical accuracies. Optimum voxel size is a compromise between practical scanning time and required statistical accuracy.

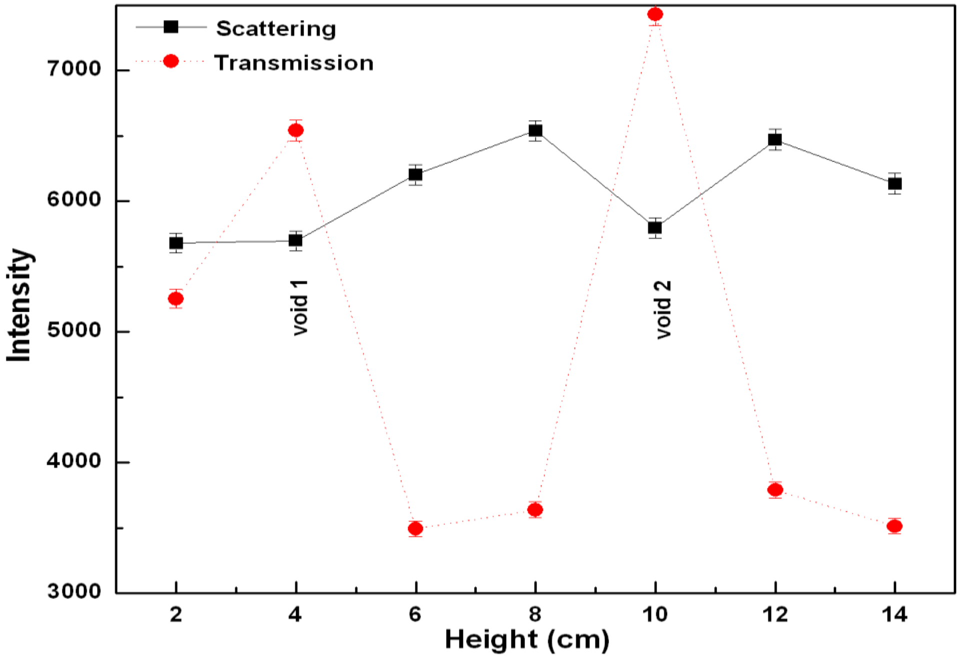

Figure 5.3 Scattered and transmitted intensity profile of concrete sample 1 embedded with two voids

Simultaneous scanning in both the scattering and transmission modes is carried out in sample 1 and sample 2. The intensity profiles of sample 1 and sample 2 are shown in figure 5.3 and figure 5.4. Location of the voids obtained from figure 5.3 and 5.4 are in agreement with figure 5.1(a) and figure 5.1(b) respectively. Generally scattering method shows higher sensitivity than transmission technique. But, the higher sensitivity of transmission technique in the present case is due to the smaller voxel sizes employed in transmission experiments. A finely collimated beam is used in the transmission experiment whereas the divergence of the source beam was more in the scattering. Due to this, the void regions represented in scattering technique have contributions from concrete.

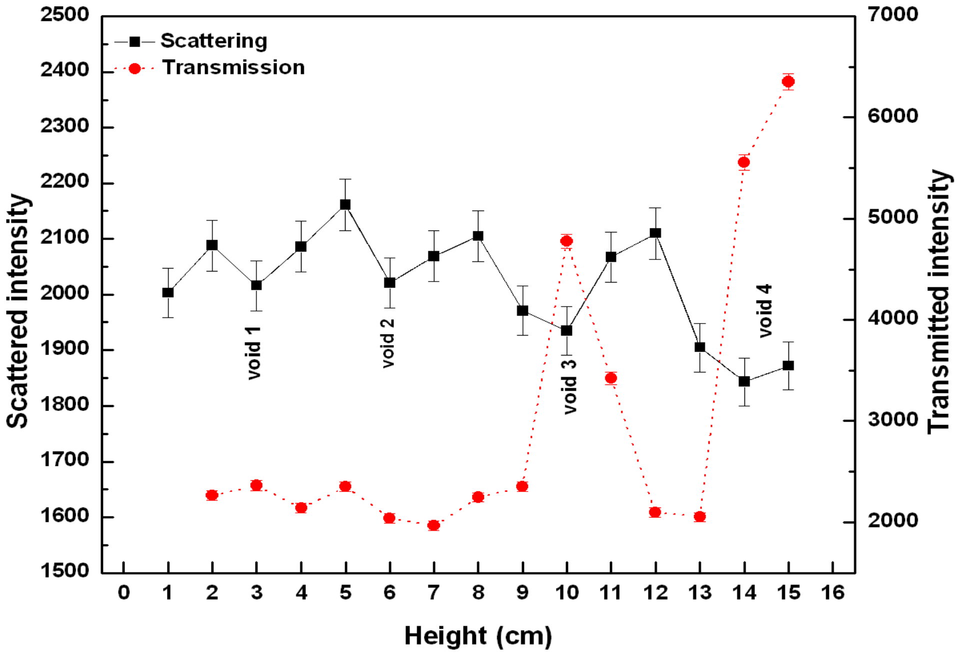

Figure 5.4 Scattered and transmitted intensity profiles of concrete sample 2 embedded with four voids of different sizes

The presence of voids is clearly visible from the plots as a ‘peak’ in the case of transmission profile and as a ‘dip’ in the case of scattering profile. The results on the position of voids from transmission and scattering methods are in good agreement with each other. In the case of sample 2 as the size of the voids increases, the relative change in transmission and scattering mode intensities increases compared to that of a smaller void and a better detection becomes possible. A good NDE system should be able to locate/ detect flaws or intrusions of varying sizes. The ability of the present experimental system in this regard is confirmed through the results obtained on sample 2. Moreover, the present experiment system could locate the hidden void in sample 2.

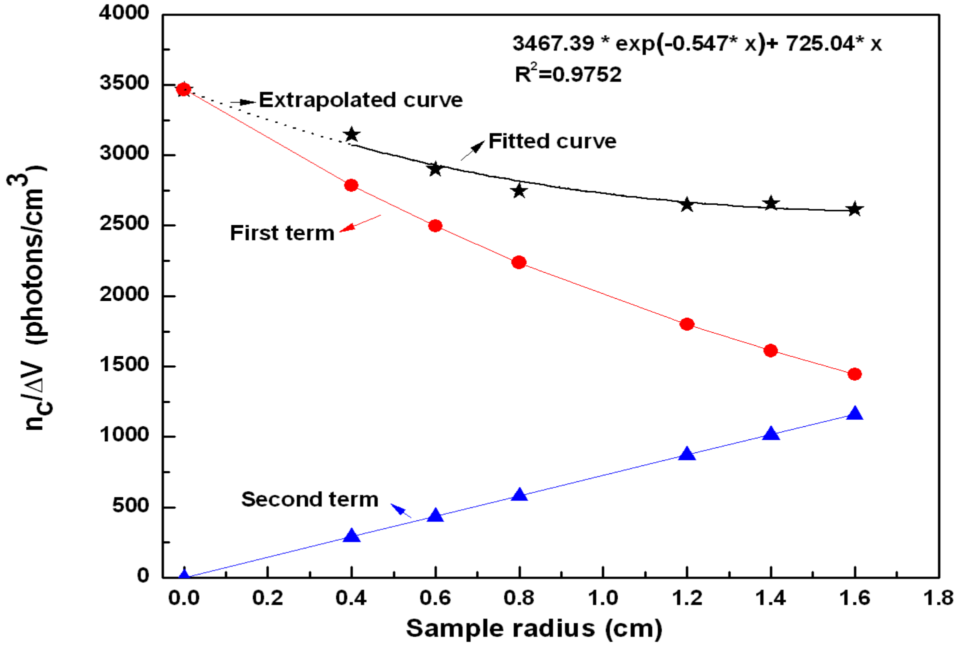

Figure 5.5 Number of scattered photons per electron ($n_c/\Delta v$) as a function of the concrete sample radius inside the voxel (fitted and extrapolated curve)

Multiple scattering factor is calculated as discussed in chapter 4. The MCNP [35] simulation of the scattering phenomena is done for different volumes (scattering centres) of concrete within the voxel by varying the radius (r) of the cylindrical sample. The total Compton scattered intensities within the energy window width ΔE (n_c) are calculated by taking the area under the photo peak. The number of scattered photons per electron ($n_c/\Delta v$) are calculated and plotted as a function of radius r of the scattering volume and is shown in figure 5.5. A non linear fit and extrapolation as explained in chapter 4 is used. The value of co-efficient of x in exponential term obtained from a non linear least square fit is comparable with the linear attenuation coefficient (0.49 cm^{-1}) of concrete obtained from the photon cross section database XCOM [36]. The non linear function is a good approximation describing the variation of scattered intensities as a function of radius of the scattering volume. The R^2 values obtained from least square fitting is 0.97. Both the exponential and linear terms are plotted and are shown in figure 5.5. The multiple to single scattering ratio is obtained from the coefficients A and C and is found to be 37% and the experimental scattered intensities are corrected for multiple scattering using this ratio. A high multiple scattering ratio is due to its dependency on the density of the sample and the voxel size.

5.2.3 Algorithm for reconstruction of density in gamma scattering method

In gamma scattering technique, the attenuation of incident and scattered radiation is significant in the case of thick and extended objects compared to thinner ones. The effects of attenuation increase with increase in depth of point of investigation and hence a detailed attenuation correction method is essential to obtain accurate results. The proposed algorithm for Attenuation Factor (AF) determination, attenuation correction and the density calculation is described here. This is based on point to point scattering method for image reconstruction [34]. The algorithm proposed by Battista et al. is limited to 135° scattering angle and an improvement of the choice of scattering angle is achieved in the present method. The densities of the objects are reconstructed by point to point scanning and a three dimensional visualisation of the sample is achieved by stacking the reconstructed layer densities. The reconstruction algorithm used in the present work is as follows:

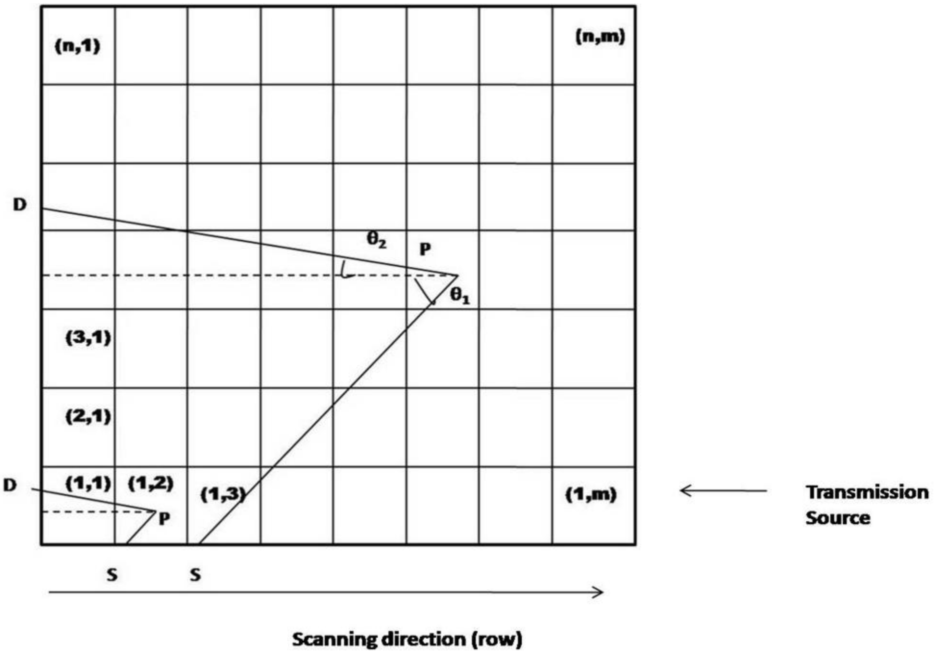

Figure 5.6 Geometry for calculating the attenuation factor

The sample is divided into several volume elements (grids) as shown in figure 5.6 depending upon the voxel size from the intersection of collimator field of views. Source position (S), detector position (D), scanning direction and transmission beam direction are marked in figure 5.6. Both incident and scattered path lengths in each grid have to be calculated in the first step for calculating the attenuation factor. Depending upon the scattering angle, path lengths in each grid can be different. The method followed for calculating the path length in each grid is given below.

5.2.3.1 Algorithm for calculation of incident and scattered path lengths in each voxel

Both incident and scattered gamma ray paths for each grid can be calculated from the knowledge of angles subtended by incident and scattered paths to the normal of the sample and they are represented as θ_1 and θ_2 respectively. In figure 5.6, normal of the sample is represented by dotted lines and gamma ray paths by bold lines. Steps involving in path length calculation are described below.

1. Get input information θ_1, θ_2, co-ordinates of scattering point (X, Y), increment or step size dx, dy.
2. Calculate slopes of incident ray and scattered ray with respect to the normal of the sample.
3. Determine the y-intercepts C_1 and C_2 for both incident and scattered ray respectively.
4. Increment x from 0 to X in steps of dx and calculate the corresponding y co ordinates for both incident and scattered path.
5. Increment y from 0 or C_1 to Y for incident path and Y to C_2 for scattered path in steps of dy and calculate the corresponding x co-ordinates.
6. Club and sort x and y co-ordinates obtained from step 4 and 5 of both incident and scattered path separately.
7. Remove repeated co-ordinate pairs.
8. Draw incident and scattered ray in a grid background where grid sizes are according to the increments.
9. Assign the corresponding grid number to each co-ordinate as shown in figure 5.6.
10. Calculate the path length in each grid from the corresponding coordinates.

Path lengths in each grid will be different depending upon the angles θ_1 and θ_2. The prescribed algorithm is capable of calculating the path lengths in each grid exactly.

5.2.3.2 Algorithm for attenuation correction and density reconstruction

The scattered counts from each of these grids are used for density reconstruction. The main assumptions are that attenuation inside the voxel is negligible and the material inside the voxel is homogenous. The geometry dependent value K is determined for the same geometry from an experimental calibration with known samples. The scattered intensity from the grid which is closer to source and detector, where no attenuation will take place is the initiation for the whole process. According to equation (1.13) scattered intensity from grid (1, 1) (represented by $I_{s(1,1)}$) is

$$I_{s(1,1)} = K \ \rho_{(1,1)} AF_{(1,1)} \tag{5.1}$$

The subscripts represent the grid and all other terms are as explained in equation (1.13). Since the attenuation within the voxel is neglected $AF_{(1,1)}$ is 1 and $\rho_{(1,1)}$ is calculated from K and $I_{s(1,1)}$. On moving to the next grid along the scanning direction, the scattered intensity is

$$I_{s(1,2)} = K \ \rho_{(1,2)} \ AF_{(1,2)} \tag{5.2}$$

AF $_{(1,2)}$ is the attenuation factor arises due to attenuation outside the grid (1, 2). From figure 5.6, SP and PD are the incident and scattered photon path lengths respectively. According to the assumptions stated above, it is the scattered ray through grid (1, 1) contributes to $AF_{(1,2)}$. The scattered path length ($l'_{(1,1)}$) is calculated using the algorithm described in section 5.3.2.1. Then the equation (5.2) becomes

$$I_{s(1,2)} = K\rho_{(1,2)} \exp\ (-\frac{\mu'}{\rho}\rho_{(1,1)} \ \ l'_{(1,1)}) \tag{5.3}$$

Mass attenuation co-efficients of concrete and void are assumed approximately equal for the energies considered in the present experiment. Hence, a common μ'/ρ for scattered energy and a common μ/ρ for incident energy are selected. Thus $\rho_{(1,2)}$ can be calculated on substitution of K, l'$_{(1,1)}$ and $\rho_{(1,1)}$ in equation (5.3). Following the same procedure densities of all the voxel in the 1st row can be determined.

$$\begin{aligned} I_{s(1,3)} &= K\rho_{(1,3)} \exp\ (-\frac{\mu'}{\rho}(\rho_{(1,1)}\ \ l'_{(1,1)} + \rho_{(1,2)}\ \ l'_{(1,2)})) \\ I_{s(1,4)} &= K\rho_{(1,4)} \exp\ (-\frac{\mu'}{\rho}(\rho_{(1,1)}\ \ l'_{(1,1)} + \rho_{(1,2)}\ \ l'_{(1,2)} + \rho_{(1,3)}\ \ l'_{(1,3)})) \end{aligned} \qquad (5.4)$$

and so on .

On going to the next row, incident photon will also get attenuated and the path length and attenuation factors can be calculated following the same simulation.

$$\begin{aligned} I_{s(2,1)} &= K\ \ \rho_{(2,1)}\ \ \exp\ (-\frac{\mu}{\rho}(\rho_{(1,1)}\ \ l_{(1,1)}) \\ I_{s(2,2)} &= K\ \ \rho_{(2,2)}\ \ \exp\ (-\frac{\mu}{\rho}(\rho_{(1,2)}\ \ l_{(1,2)}) + \frac{\mu'}{\rho}(\rho_{(2,1)}\ \ l'_{(2,1)})) \end{aligned} \qquad (5.5)$$

and so on.

Then source will move to row 3 and so on. Thus the process can be represented by the following equation

$$I_{s(i,j)} = K\ \ \rho_{(i,j)}\ \ \exp\ (-\frac{\mu}{\rho}\sum_{k=1}^{i-1}\sum_{q=1}^{j-1}\rho_{(k,q)}\ \ l_{(k,q)} + \rho_{(k,q)}\ \ l'_{(k,q)}) \qquad (5.6)$$

If no scattered or incident paths are present in a grid, corresponding path length will become zero and thus the density of that grid will be insignificant in the equation.

Since the density obtained for a grid will determine the attenuation correction and hence density of next grid, the error in density determination is propagated from one grid to another. So an additional measurement is required for reducing the error and this is achieved by a simultaneous transmission experiment. A transmission test is made in a direction parallel to the scanning direction. An average density of one row is obtained from transmission method from the relation

$$I_t = I_{0t}\exp(-\frac{\mu}{\rho}\rho t) \qquad (5.7)$$

I_t and I_{0t} are the transmitted and incident intensity respectively and t is the thickness of the material. After obtaining the densities of ith row from scattering method and transmission method a correction factor (Δ_i) is obtained on comparison with transmission method.

$$\Delta_i = \frac{\rho_t - \frac{1}{m}\sum_{j=1}^{m}\rho_{s(1,j)}}{\rho_t} \qquad (5.8).$$

The subscripts to ρ are used to represent the technique and m is the number of grid in ith row. Each density in row i is corrected using this factor.

$$\rho'_{(i,j)} = (1+\Delta_i)\rho_{(i,j)} \qquad (5.9)$$

Similarly each row can be corrected on comparison with the transmission experiment. Correction to one row has to be applied before proceeding to the next row. By following this grid to grid density determination procedure, density and attenuation co-efficient of one grid is used for the attenuation factor determination of other grids. Thus this method requires a sequential determination of density.

In the present work larger voxel is used and it demands the attenuation inside the voxel also to be considered, whereas the above algorithm neglects it. While calculating the density of (i, j)th grid, the attenuation effects from grids k>i and q>j are not considered in the above algorithm. The densities of those grids are not obtained since the sequential scanning is following. To overcome these two drawbacks, reconstructed and corrected densities are used again for correcting the attenuation inside the voxel and thus a new set of densities are obtained. Thus the equation (5.9) becomes

$$I_{s(i,j)} = K \ \ \rho_{(i,j)} \ \ \exp \ (-\frac{\mu}{\rho}\sum_{k=1}^{n}\sum_{q=1}^{m}\rho_{(k,q)} \ \ l_{(k,q)} + \rho_{(k,q)} \ \ l'_{(k,q)}) \quad (5.10)$$

Even though the same procedure is repeated, both the path lengths inside the voxel and extension of summation to n and m respectively are used to get a new set of densities. This procedure is continued till densities converge to the same value. The need of employing multiple detectors at various directions and the rotation of the sample are eliminated in this method.

The algorithm for reconstruction of images employed in gamma scattering method is validated by reconstructing the densities of a layer of concrete block of dimension 7 x 7 x 1 cm^3 with uniform density 2.24 g/cm^3 where no voids are present. The scattered intensities from different voxels of this sample are obtained by experiment and by MCNP code. Simultaneous transmission experiments along the scanning direction are also performed. Transmitted intensities are calculated by MCNP method also. The constant K (geometric factor) is obtained from the experiments performed using known sample. The scattered intensities obtained are used for the image and density reconstruction by applying the above algorithm. The reconstructed densities are used again for correcting the attenuation inside the voxel and thus a new set of densities are obtained. This procedure is continued till the convergence of densities of each voxel is obtained and generally this is achieved with in 5 iterations. The contour plots of reconstructed densities from both the methods are shown in figure 5.7. Each voxels are represented by the corresponding density.

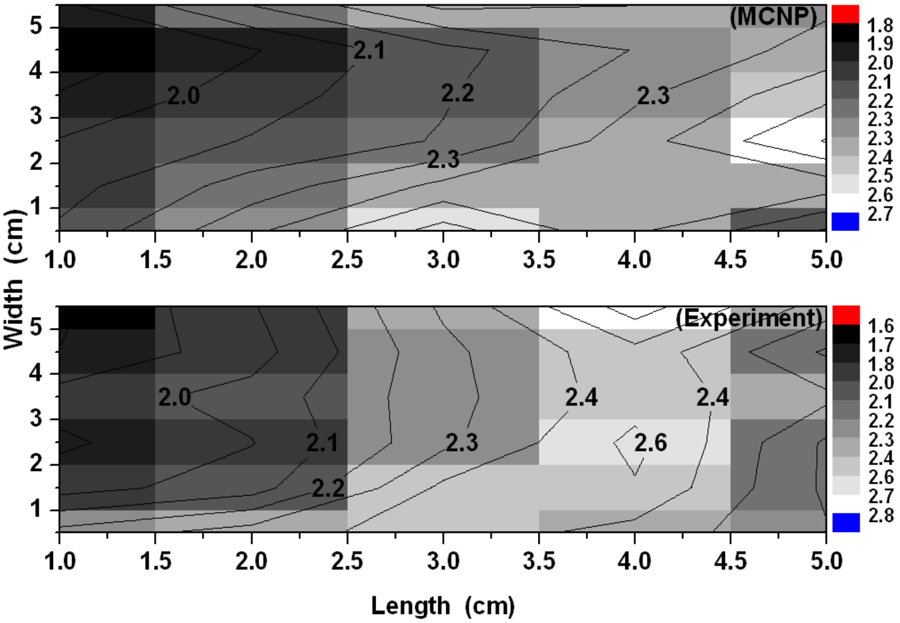

Figure 5.7 Reconstructed density contour plots of a concrete layer from the MCNP and experimental intensities

The calculated densities are in the range of 1.8 to 2.7 g/cm^3 and 1.6 to 2.8 g/cm^3 in MC method and experimental method respectively. Majority of the voxels have densities between 2-2.4 g/cm^3. Thus average densities obtained from MCNP code and experiment, are 2.2217 g/cm^3 and 2.2151 g/cm^3 respectively. Homogeneity of the reconstructed densities are checked from the values of root mean square deviations [34] and found to be 0.1955 g/cm^3 and 0.2694 g/cm^3 respectively. Thus the algorithm is able to reconstruct the density by applying proper attenuation corrections. The deviation will further reduce for smaller voxel sizes due to less attenuation and due to the improved validity of the assumptions in the reconstruction algorithm.

5.2.4 Reconstruction of density images

Both sample 1 and 2 are scanned simultaneously in transmission and scattering mode. Densities of each voxel are calculated by employing the algorithm. The contour plot of the surface densities obtained for both the samples 1 and 2 are shown in figure 5.8. The denser regions (> 1.8 g/cm^3) are represented by dotted lines and lighter ones or void region are represented by thick lines. The criterion of 1.8 g/cm^3 is selected considering the density range obtained for homogeneous concrete sample. The vertical height of the contour regions are selected as the dimension of the void because the reconstruction error will be same in this direction. Dimensions of each voids obtained are also mentioned in figure 5.8. Since the step size used and the voxel size are greater than the size of the smaller voids studied in the present experiment the quantification of these voids may lead to inaccurate results. The better accuracy of the results of quantification can be achieved by reducing the size of the voxel employed in the experiment.

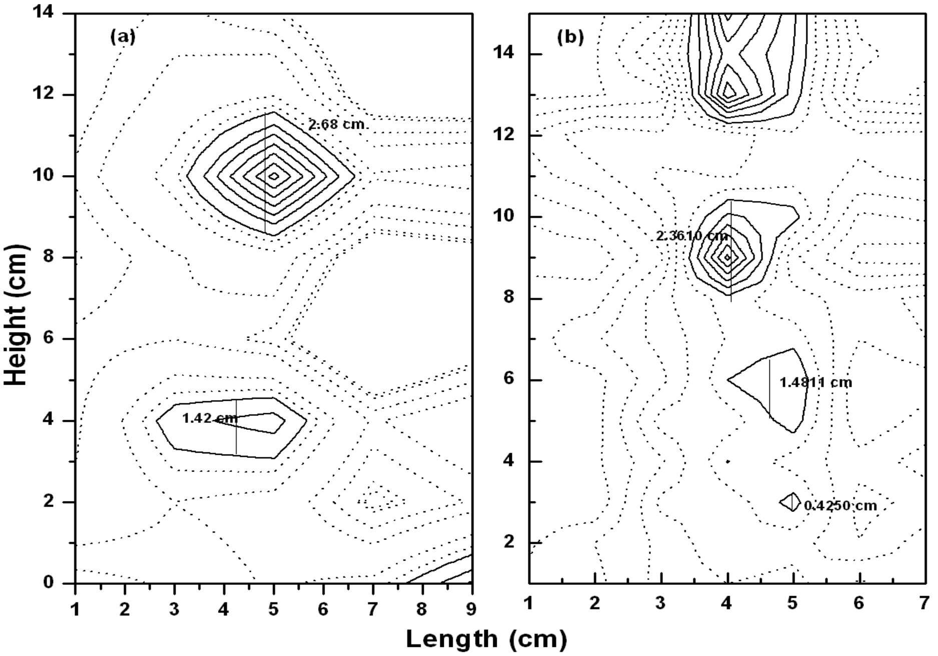

Figure 5.8 Surface contour plots of sample 1 (a) and sample 2 (b)

The three dimensional scanning of the samples 1 and 2 are carried out in horizontal, lateral and vertical directions in steps of 1 cm The three dimensional image of the sample 1 is reconstructed by stacking the densities of each layer and is shown in figure 5.9(a). The positions of the two voids obtained from three dimensional scanning are in agreement with those obtained from one dimensional scanning in vertical direction (figure 5.3). The densities of voids obtained from reconstruction vary from 0.4 to 1.2 g/cm^3. This is mainly due to the background contribution from nearby concrete region to the scattered intensity and this can be minimized by decreasing the size of the voxel. The reconstructed three dimensional image of sample 2 is shown in figure 5.9(b). Due to the constraints in the present experimental arrangement only 15 cm scan of 20 cm sample size is possible and because of this the void at 14 cm vertical height is partially visible. The voids at vertical heights of 10, 6 and 3 cm are clearly seen in figure 5.9(b) which is in accordance with the one dimensional profile (figure 5.4).

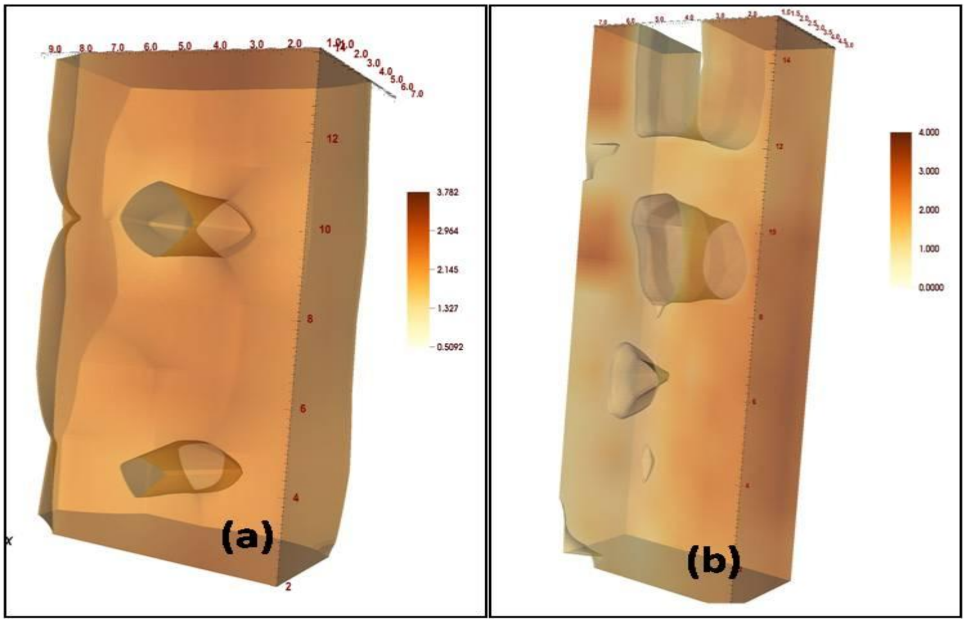

Figure 5.9 Three dimensional images of sample 1 (a) and sample 2 (b) (all dimensions are in cm).

The statistical errors on scattered intensities from higher depths of concrete (> 6 cm) are relatively high due to increased attenuation of the incident and scattered radiation and because of this reason it is not possible to obtain accurate depth information of voids at higher depths. Even though we are utilizing the transmission technique for limiting the error propagation, subsurface defects images can be obtained without a transmission technique. Surface density images of sample 1 with and without utilizing the transmission technique for error correction is given in figure 5.10. Figure 5.10(a) shows the image obtained after correcting the error using transmission counts. Figure 5.10(b) shows the image obtained only from scattering experiment. The voids are located and could be seen in both the figures 5.10(a) and (b), however, the image is better in former compared to later one in differentiating concrete and void phases. Moreover, distinction between void1 and void 2 is better in figure 5.10(a) than figure 5.10(b). Hence the modified attenuation algorithm results in location of the voids without application of transmission method for error propagation correction, even though the error correction improves image quality.

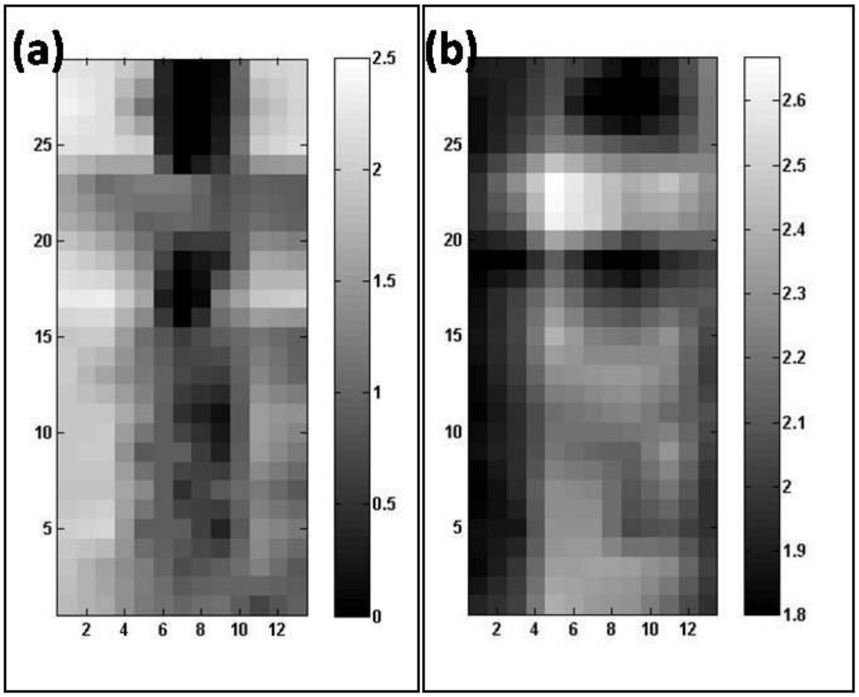

Figure 5.10 Surface images of sample 2 obtained from reconstructed densities with error correction (a) and without error correction (b)

Long scanning time is required in scattering technique; however, this technique is highly advantageous when the sample rotation and direct contact is restricted. In the present experimental set-up, source and detector are far away from the sample due to the configuration of the present experimental system. There is a scope for improvement where source and samples can be placed closer to the scanning object to reduce the scanning time. For practical imaging applications, high statistical accuracy obtained in the present experiment may not be required for quick scan. The results on quantitative determination of voids and objects size position and accuracy of the present reconstruction algorithm can be improved and more precise and point information can be obtained by selecting a relatively small voxel size and choosing larger scanning time. But for quicker scan a sacrifice over the voxel size is desired. This technique could be effectively used for the identification and quantification of voids in concrete up to a depth of 7 cm using ^{137}Cs source in the incident direction and 5 cm in the scattered direction without rotating the sample. Higher depths can be scanned by selecting gamma ray source of higher energy and optimum scattering angle to minimize the attenuation especially in the scattered path and further improvements in the image can be achieved by using gamma ray source of higher strength.

5.3 Determination of water content in concrete

5.3.1 Sample details

Seven similar concrete samples of dimension 5 x 5 x 5 cm^3 of density 2.4 g/cm^3 have been fabricated according to standard mix ratios and cured for 28 days. The concrete mix for the specimen comprised ordinary Portland cement, coarse aggregate, sand and water in the proportion of 1: 3.121: 1.830: 0.484 respectively. The weights of all the samples were found to be same after curing including the reference sample and hence the constant initial water content is assumed. Among these samples one sample is kept as the reference sample and varying amount of water is added to other samples and kept for 24 hours to distribute the water uniformly inside the concrete.

5.3.2 Quantification of water content from experimental intensities

The scattered and transmitted intensities were calculated from corresponding PHS of each sample by integrating the corresponding counts under the photo peak. Experiments were carried out using both sides of the sample and the average of these intensities were taken for further analysis. A background PHS was recorded without sample and deducted from the sample PHS. In the case of transmission experiments, direct intensity was determined by removing the sample.

The volumetric water content, θ, in concrete can be calculated as given below:

$$\theta = \frac{V_w}{V_c} \tag{5.11}$$

where V_w is the volume of the water and V_c is the volume of concrete.

Water content in each sample is calculated gravimetrically using the relation (5.11). Since the density of water is unity, change in mass after absorbing water is considered as the volume of the water. Since no shrink or swell is seen after absorption of water the volume of the concrete sample is assumed to be same

Linear attenuation co-efficient of concrete sample with various amount of added water for both incident gamma energy (661.6 keV) and scattered energy (254 keV) are calculated using XCOM. The concrete composition given by Hubbell and Seltzer has been used for the dry concrete and the fractional weights of various elements used for calculating the attenuation factors are given in table 5.1[37]. The calculated attenuation factors for both transmission and scattering configurations for different water content (0 to 0.096 relative to the concrete volume) for the present sample dimension are tabulated in table 5.2.

Element	Water content in concrete (θ)				
	0	0.024	0.048	0.072	0.096
H	0.0221	0.0230	0.0239	0.0248	0.0257
C	0.0025	0.0025	0.0024	0.0024	0.0024
O	0.5749	0.5781	0.5812	0.5843	0.5875
Na	0.0152	0.0151	0.0149	0.0148	0.0146
Mg	0.0013	0.0013	0.0012	0.0012	0.0012
Al	0.0199	0.0200	0.0196	0.0194	0.0192
Si	0.3046	0.3016	0.2985	0.2955	0.2924
K	0.0100	0.0099	0.0098	0.0097	0.0096
Ca	0.0430	0.0425	0.0421	0.0417	0.0412
Fe	0.0064	0.0064	0.0063	0.0062	0.0062

Table 5.1 Fractional weights of constituent elements in concrete samples with various amount of water content.

Water content (θ)	Attenuation factor in transmission	Attenuation factor in scattering
0	0.388	0.309
0.024	0.384	0.305
0.048	0.380	0.301
0.072	0.376	0.297
0.096	0.372	0.293

Table 5.2 Attenuation factors calculated using XCOM for concrete sample with various amount of water content

5.3.2.1 Transmission technique

Water content in the concrete sample can be determined using the given relation [38]

$$\theta = \frac{1}{\mu_w}\left(\frac{1}{x_c}\ln\left(\frac{I_{0t}}{I_t}\right) - \mu_c\right), \qquad (5.12)$$

where I_{0t} is the intensity of incident radiation, I_t is the transmitted intensity, μ_w is linear attenuation co-efficient of water , μ_c is linear attenuation co-efficient of dry concrete and x_c is the thickness of the concrete sample. μ_c of the dry concrete can be calculated from the transmitted intensity through it.

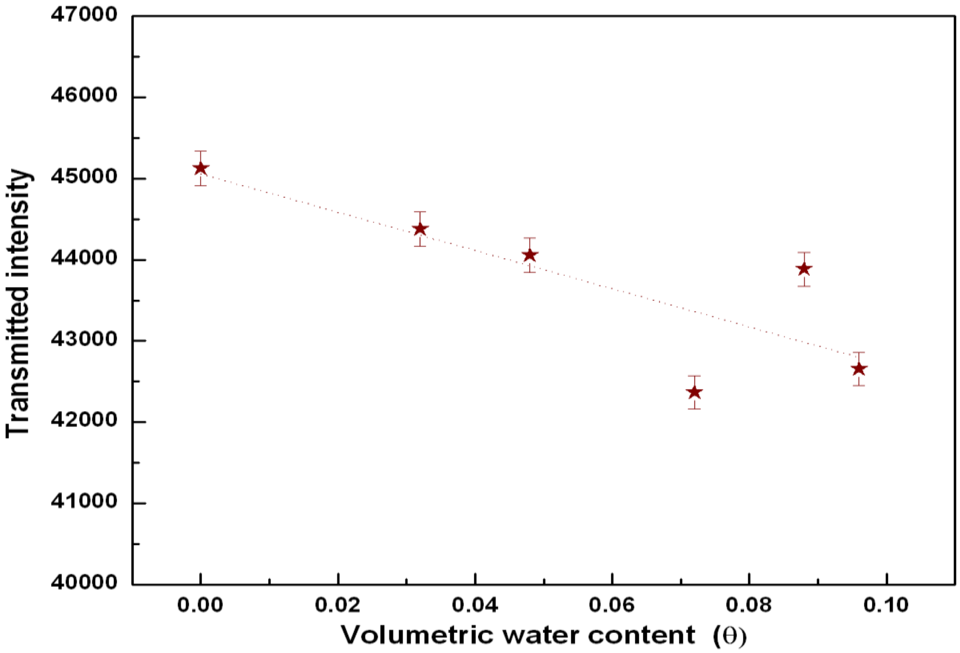

Figure 5.11 Transmitted intensities as a function of volumetric water content.

Figure 5.11 shows the experimental transmitted intensities as a function of θ obtained gravimetrically and a decrease in transmitted intensity is seen and is in agreement with trend seen in table 5.2. Figure 5.12 shows the μ_{cw} the linear attenuation coefficient of water added concrete sample as a function of θ calculated from gravimetric method. It can be seen from the figure 5.12 that a linear relationship exists between μ_{cw} and θ and the slope derived from this relationship is nearly equal to μ_w from theory. The theoretical μ_c (0.1893 cm^{-1}) is higher by a factor of 1.07 times compared to experimental (0.17738 cm^{-1}) one derived from the intercept of the figure 5.12 and this can be attributed to the fact that actual composition of the sample may not be same as that used in calculation. However, a direct relationship between μ_{cw} and θ is established and it validates the equation (5.12).

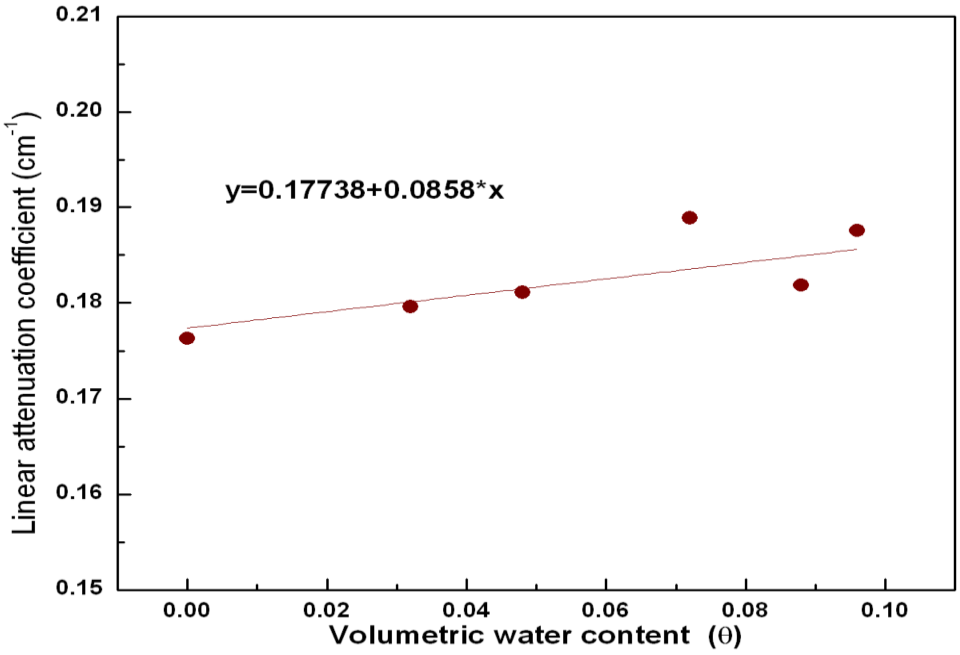

Figure 5.12 Linear attenuation coefficient calculated from transmitted intensities as a function of volumetric water content

5.3.2.2 Scattering technique

The scattered intensity is a function of concrete density and any increase in concrete water content results in more scattering centers and hence scattered intensity gets enhanced. Any change in scattered intensity with respect to reference sample i.e., dry concrete can be used to calculate the water content. Figure 5.13 shows the scattered intensity obtained experimentally as a function of water content determined by gravimetrical method. The scattered intensities are affected by attenuation and a correction factor has to be incorporated which is a function of water content. The attenuation factors given in table 5.2 are modified according to the ratio obtained between theoretical and experimental attenuation factors from transmission method. The correction factor is calculated by taking the inverse of this modified scattering attenuation factor and plotted as a function of volumetric water content. Thus the discrepancy in attenuation factor resulting due to substitution of composition of dry concrete employed in XCOM for calculating attenuation factor is removed. The calculated correction factors are plotted as a function of volumetric water content as shown in figure 5.14.

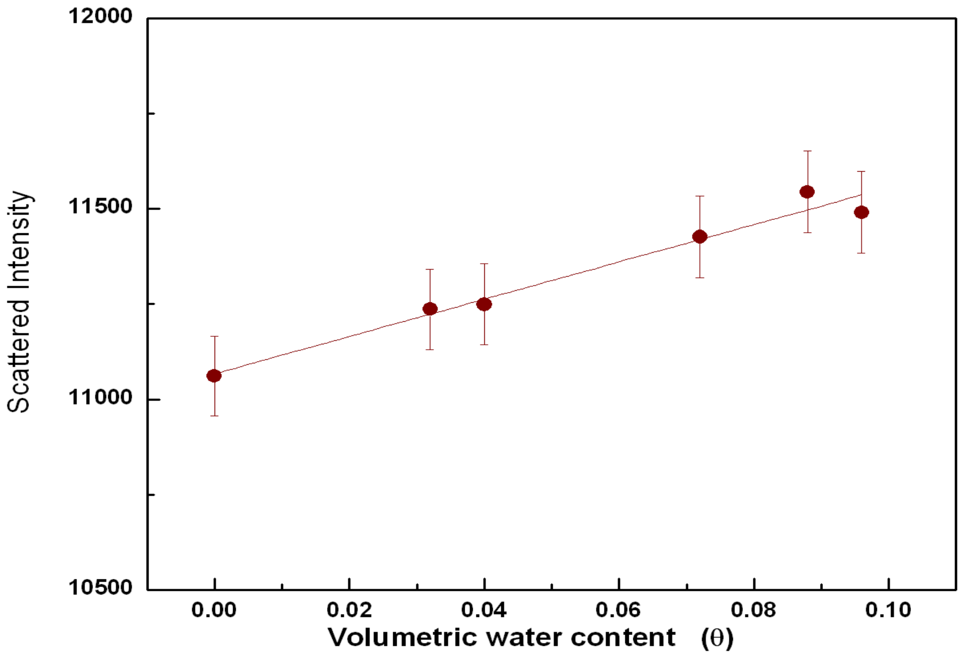

Figure 5.13 Scattered intensity as a function of volumetric water content

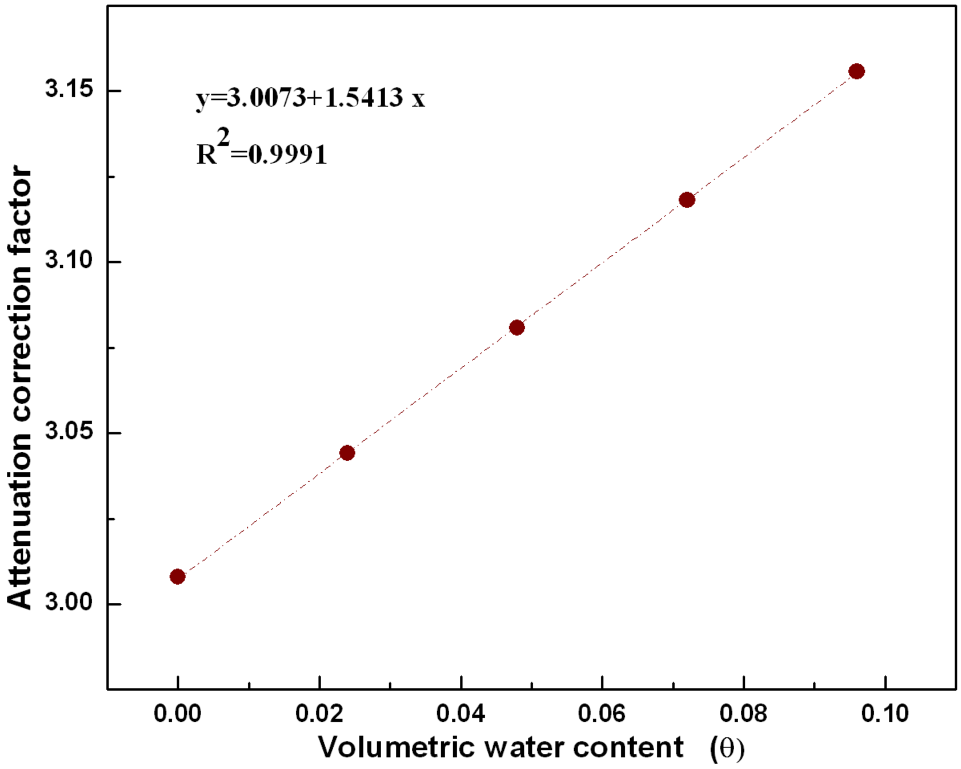

Figure 5.14 Attenuation correction factor as a function of volumetric water content

A linear relationship between the correction factor and the water content is obtained and these factors are used to correct the scattered intensities in samples with varying water content. Volumetric water content is calculated using the following relation

$$\theta = \frac{I_{sw}(A+B\theta)-I_{sc}A}{I_{sc}A}, \qquad (5.13)$$

where I_{sw} and I_{sc} are the scattered intensity from the water added sample and reference sample respectively, A and B are the constants obtained from figure 5.14. Multiple scattering is neglected in the present calculation because it will be nearly same for all the samples and hence the effect likely to be cancelled out on taking the ratio. The volumetric water contents of various samples calculated by gravimetric, transmission and scattering methods using the equations (5.11, 5.12 and 5.13) respectively are given in table 5.3. Except at one point (9.6%)

scattering technique is in good agreement with the gravimetric technique within the accuracy of 6%. But observed deviation is more in transmission technique.

Gravimetric Method	Transmission Method	Scattering Method
3.2	3.89±0.04	3.30±0.04
4	-	3.55±0.04
4.8	5.58 ±0.06	-
7.2	14.7±0.17	7.01±0.09
8.8	6.49±0.07	9.39±0.14
9.6	13.12±0.15	8.29±0.11

Table 5.3 Comparison of volumetric water content (in percentage) determined gravimetrically, transmission method and scattering method.

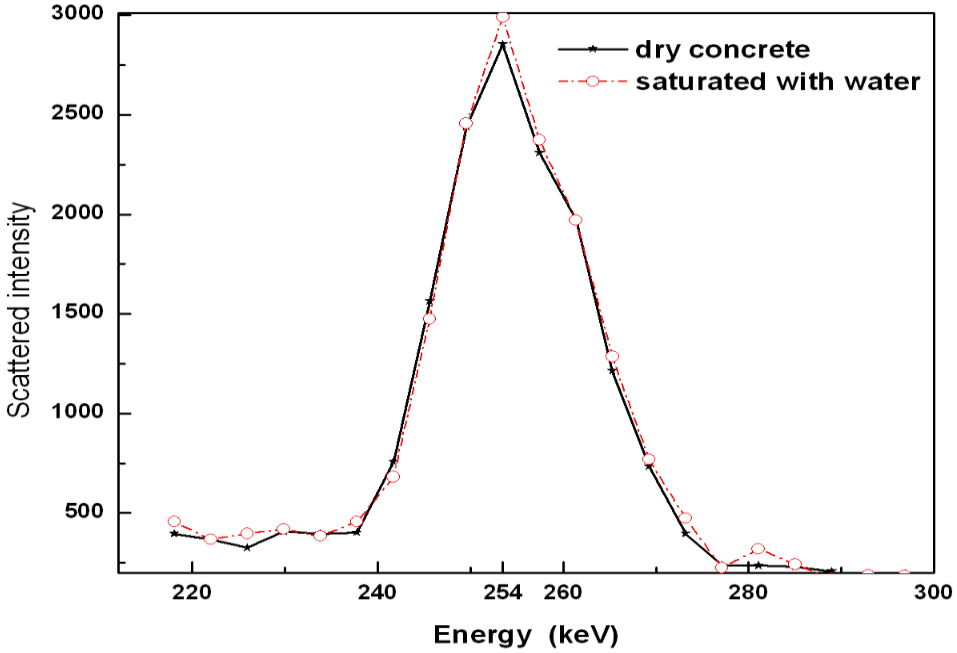

Figure 5.15 MCNP simulated PHS for dry concrete and water saturated concrete

The scattered intensities are simulated using MCNP and the simulated PHS for sample with volumetric water content 0.096 and reference sample are shown in figure 5.15.

A clear indication of increased scattering intensity for samples as a function of added water is obtained from the MCNP simulation, which also supports the experimental findings.

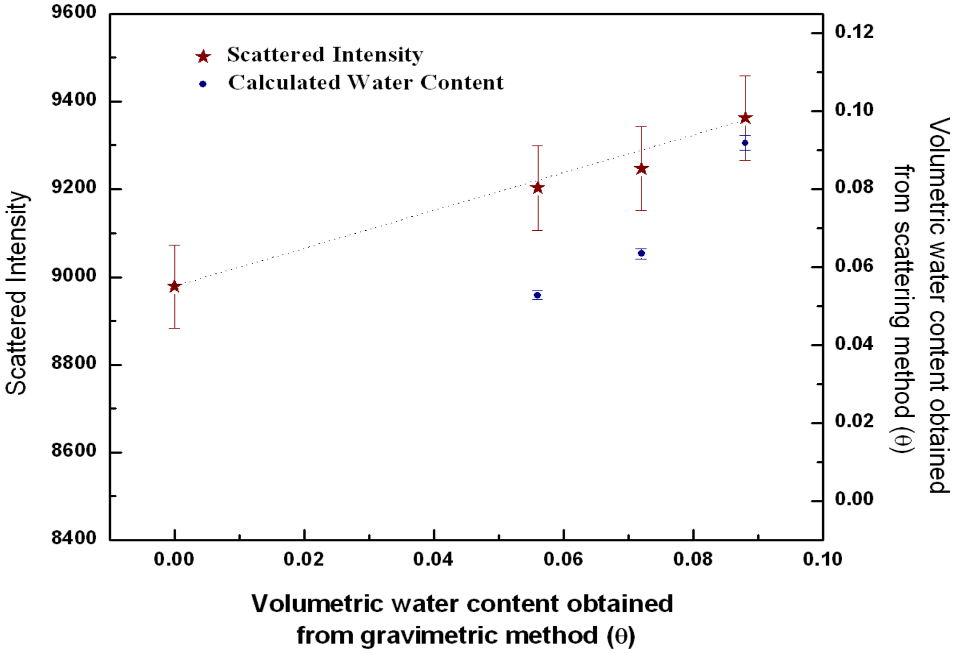

Figure 5.16 Scattered intensities and volumetric content determined from the same sample

Water content is estimated using a single sample to rule out the errors arising from the possible composition variations among different samples. In this method a sample initially with volumetric water content 0.088 is heated in an oven at 105ºC for various durations. Scattered intensities of the sample are measured as a function of heating time and the sample is weighed each time to calculate the water content gravimetrically. This process is continued till the sample attains the weight of the reference sample. The scattered intensities and the calculated water content are plotted in figure.5.16 and a fair agreement is seen between the experimental results and those obtained by gravimetric method.

An accurate estimation of total volumetric water content in measured concrete samples is possible by knowing the exact bound water content of the reference sample. The minimum detectable volumetric water content is 0.02 from the present gamma scattering experiment. For materials having lower sorption co-efficient, gamma scattering method can be used for the moisture profile studies and for higher sorption co-efficient materials, an accurate measurement of moisture profile will be possible only with employment of higher source strength. This method can be employed to find out the point wise distribution of water content in concrete structures otherwise not possible by gravimetric and transmission methods .

References

1. Sahin, S.R., Polat, R., Icelli, O., Celik, C., Ann. Nucl. Energy., 38 (2011), 1505-1511
2. Hilsdorf, H.K., Nucl. Eng. Des., 6 (1967), 251-263
3. Janz, M., Methods of measuring the moisture diffusivity at high moisture levels, Lund Institute of Technology, Division of Building Materials, Lund (1997)
4. Wormald, R., Britch, A.L., Build. Sci., 3 (1969), 135-145
5. Roels, S., Carmeliet, J., Hens, H., Adan, O., Brocken, H., Cerny, R., Pavlik, Z., Ellis, A.T., Hall, C., Kumaran, K., Pel, L, Plagge, R, J. Therm. Envel. Build. Sci., 27 (2004), 261-276
6. Malhotra, V.M., Testing hardened concrete: Nondestructive methods, American concrete institute monograph No.9, ACI/Iowa state university press (1976)
7. Carino, N.J., Nondestructive testing of Concrete: History and challenges, Concrete technology past present and future, V.K.Mehta (Ed), American Concrete Institute, (1994), 623-678
8. Reijonen, H., Pihlajavaara, S.E., Cement Concrete Res., 2 (1972), 607-615

9. Nizovtsev, M.I., Stankus, S.V., Sterlyagov, A.N., Terekhov, V.I., Khairulin, R.A., Int. J. Heat Mass Transfer, 51 (2008), 4161-4167
10. Buyukozturk, O., NDT&E Int., 31 (1998), 233-243
11. Mitchel, T.W., Radioactive/Nuclear Methods, Chapter 10 in Handbook on Nondestructive testing of Concrete, Malhotra, V.M., Carino, N.J., (Eds), CRC Press (1991), 227-252
12. Smith, E.E., Whiffin, A.C., The engineer, 194 (1952), 278-281
13. Tayabji, S.D., Whiting, D., Trans. Res. Rec., 1110 (1988), 90-100
14. Preiss, K., ACI Journal & Proceedings, 63 (1966), 743-748
15. Simpson, J.W., Build. Sci., 3 (1968), 21-29
16. Harland, D.G., Mag. Concrete. Res., 18 (1966), 95-101
17. Holt, R.S., Cooper, M.J., NDT Int., 20 (1987), 161-165
18. Holt, R.S., Cooper, M.J., Jackson, D.F., Nucl. Instrum. Methods, 221 (1984), 98-104
19. Mullin, S.K., Hussein, E.M.A., Nucl. Instrum. Meth. A., 353 (1994), 663-667
20. Balogun, F.A., Spyrou, N.M., Nucl. Instrum. Meth. B., 83 (1993), 533-538
21. Harding, G., Radiat. Phys. Chem., 50 (1997), 91-111
22. Achmad, B., Hussein, E.M.A., Appl. Radiat. Isot., 60 (2004), 805-814
23. Ho, A.C., Hussein, E.M.A., Appl. Radiat. Isot., 53 (2000), 541-546
24. Banerjee, K., Dunn, W.L., Appl. Radiat. Isot., 65 (2007), 176-182
25. Sharaf, J.M., Appl. Radiat. Isot., 65 (2007), 1330-1336
26. Adil, N., Brit. J. Nondestr. Test., 19 (1977), 72-77
27. Gautam, S.R., Hopkins, F.F., Klinkseik, R., Morgan, L.L., IEEE. Trans. Nucl. Sci., 30 (1983), 1680-1684

28. Hussein, E.M.A., Whynot, T.M., Nucl. Instrum. Meth. A., 283 (1989), 100-106
29. Tuzi, S., Sato, O., Appl. Radiat. Isot., 41 (1990), 1013-1018
30. Tuzi, S., Sato, O., Appl. Radiat. Isot., 44 (1993), 1279-1284
31. Shivaramu, Bose, A., Margret, M., arXiv:0912.1554
32. Raghunath, V.M., Bhatnagar, P.K., Meenakshisundaram, V., Nucl. Instrum. Methods., 206 (1983), 303-307
33. Shivaramu, Vijayakumar, R., Rajasekaran, L., Ramamurthy, N., NDE 2002, National Seminar on ISNT, Chennai, (2002)
34. Battista, J.J., Santon, L.W., Bronskill, M.J., Phys. Med. Biol., 22.(1977), 229-244
35. Briesmeister, J. F, (Ed), 2000, MCNP™, LA-13709-M Manual
36. Berger, M.J., Hubbell, J.H., 1987, NBSIR 87-3597, MD 208991987
37. Hubbell, J.H., Seltzer, S.M., 1995, Tables of X-ray mass attenuation coefficients and mass energy-absorption coefficients 1 keV to 20 MeV for elements Z=1 to 92 and 48 additional substances of dosimetric interest, NISTIR 5632.
38. Da Rocha, M.C., Da Silva, L.M., Appoloni, C.R., Filho, O.P., Lopes, F., Melquiades, F.L., Dos Santos, E.A., Dos Santos, A.O., Moreira, A.C., Potker, W.E., De Almeida, E., Tannous, C.Q., Kuramoto, R., Cavalcante, F.H.D.M., Barbieri, P.F., Caleffi, A.F., Carbonari, B.T., Carbonari, G., Radiat. Phys. Chem., 61 (2001), 567-569.

Chapter VI Conclusions, summary and future scope of work

6.1 Conclusions and summary

The present experimental study could emphasis the sensitivity and accuracy of gamma scattering method as an NDE tool for determination of flaws in low Z materials. The direct relationship with the scattered intensity and material density is utilized for the characterization of samples in this study. Major findings from this study are summarized below.

- The ability of gamma scattering technique for NDE of low Z materials with different density ranges (0.651-1.26 g/cm^3), (2-2.4 g/cm^3) and 7.9 g/cm^3 is demonstrated in this work.
- The scattered PHS simulated using MCNP for various samples are in agreement with those obtained from the corresponding samples experimentally. The area under the photo peaks obtained from experimental PHS and MCNP simulation are found in agreement within 10% variation. Thus MCNP simulations support the experimentally obtained results.
- Scattering method is found to be a possible method for the detection of thickness loss due to corrosion in MS plate.

  - ➢ The method prescribed for attenuation correction and iterating the thickness from scattered intensities is used for quantification of thickness loss with respect to a reference sample. The percentage thickness loss estimated at different positions of the corroded MS plate varies from 17.78 - 27.0 by gamma scattering, 19.5 - 32.03 by gammatography and 19.26 - 29.15 by radiography method. Overall these results are consistent and in line with each other.
  - ➢ Signal to Noise ratios for various percentages of corrosion obtained from MCNP simulation and experiments are in good agreement. The experimental and MC simulation results show that the scattering method is highly sensitive to changes in electronic and physical densities of the volume element under study and the magnitude of embedded corrosion can be clearly identified and quantified by monitoring single scattered events.
  - ➢ The gamma scattering system used in the present study could detect the corrosion in MS plate with a minimum detectable limit of 1.4 mm. Accurate average thickness can be determined by selecting a small scattering volume.

- A semi empirical method for accounting the self absorption and multiple scattering are prescribed with an accuracy of $R^2 > 0.9$.
  - ➢ The density values obtained by making use of this extrapolated intensity agree with that of standard densities. Therefore, a calibration of system based on this extrapolation method is suggested for correcting self absorption and multiple scattering.
  - ➢ An increase in MSF is obtained with density and the calculated MSF values are in agreement with the literature values in the present mean path.

    - Multiple scattering effects found to be negligible when two samples with same density were compared. An accurate accounting of attenuation and multiple scattering contributions is required for density determination in high dense samples.

- The gamma scattering method is employed for the quantification of density and concentration of low Z solutions/fluids with comparable attenuation parameters and the results are in agreement with the standard values.
    - Higher relative sensitivity is obtained for scattering technique than transmission technique in radiologically thin samples as a function of density and concentration of the solutions.
    - Accuracy in quantification of density is also superior in the case of scattering technique than transmission technique for the selected low dense, low atomic number solutions having similar attenuation properties.
    - A minimum resolution of 0.025 g/cm^3 is obtained from scattering technique in low density materials.
    - The goal of accurate concentration determination for low -Z solutions can be achieved due to higher sensitivity of the scattering technique over transmission one along with proper corrections for multiple scattering and self absorption.
- Gamma scattering level gauges could locate the fluid-fluid and fluid –air interfaces accurately and the slopes obtained from different polar and non polar combinations are employed for this purpose.
    - A clear indication of interface is obtained with in 60 s per voxel scanning and as measurement time increases the interface becomes clearer.

  - Higher accuracy is obtained for scattering technique compared to transmission technique.
  - This has obvious consequences for the level determination in large/thin high temperature reservoirs on-line where other conventional methods may inadequate.
- Scattering and transmission techniques are used for determination of voids and volumetric water contents in concrete blocks.
  - Scattered and transmitted intensities clearly indicated the presence of voids in the concrete samples. The minimum detectable limit using the present experimental setup is void of 5 mm diameter.
  - A good agreement of the experimental results in the positional accuracy and a fair agreement in the quantification of void sizes and densities with the actual ones are achieved.
  - The density reconstruction algorithm prescribed is effective to calculate the path length inside each grid for any scattering angle. The algorithm is utilized to reconstruct the densities of each voxel of a homogeneous concrete block from the corresponding experimental and simulated scattered intensities. Thus average densities obtained from MCNP code and experiment, are 2.2217 g/ cm^3 and 2.2151 g/cm^3 respectively with root mean square deviations of 10 %.
  - The algorithm is used to reconstruct the three dimensional density images of the concrete samples embedded with voids.
  - Even though the prescribed algorithm utilizes the data obtained from transmission method for reconstruction, surface and near surface images can be obtained directly from scattered intensities.

- The present system could be effectively used for the identification and quantification of voids in concrete up to a depth of 7 cm using ^{137}Cs source in the incident direction and 5 cm in the scattered direction without rotating the sample.
- The scattering technique could estimate the water content in concrete and a variation of 2% can be detected. The volumetric water content calculated from scattered intensities is in good agreement with the gravimetric results.

6.2 Improvements and future scope of study

The longer scanning duration of the present system is one of the areas where improvements are required for developing the system for field study and on line applications. The present experimental setup demands a scanning time of 10 min per voxel for lighter samples to obtain a statistical accuracy of 2%. This is due to the large distance between source and sample. However, the scanning time can be reduced by decreasing the distance between the source and sample and thereby the resolution can be improved. Scanning duration can be reduced by employing high strength source with proper shielding and this will be useful mainly for a lab scale study.

The spatial resolution of the system depends upon the voxel size. Since the collimator size define the voxel size, new collimator designs including the split collimators can improve the voxel size and resolution.

Higher depths can be scanned by selecting gamma ray source of higher energy and optimum scattering angle to minimize the attenuation especially in the scattered path and further improvements in the image can be achieved by using gamma ray source of higher strength.

The uncertainty in the measurement can be minimized by increasing the scattered intensity. This can be achieved by either increasing the source strength or by increasing the measurement duration.

The perspective areas and potential fields of scattering technique putting forward from the present study are listed

1. The preliminary studies of Compton scattering system for moisture content determination proved the potential of this technique and substantial improvements and research can lead to online moisture profile studies with scattering technique using a faster scanning system.
2. Even though the present study is limited to corrosion in mild steel, it can be extended for thickness measurement in any low Z materials. Lower source strength or low energy source can be used for materials with smaller density and attenuation parameters.
3. The hidden corrosion detection under thick structures or insulators can be tested.
4. Reconstruction algorithm can improve further to avoid the use of transmission data enabling to use in single sided geometry.
5. A new potential possibility of gamma photon based technique for detection and reading of bubble detector is described in the appendix. Experimental results are in good agreement with the theoretical model suggested. However the present study is limited to high dose environment, further improvements and research warrants for developing this technique. Portable gamma transmission gauges can be developed similar to the light scattering bubble readers.

Appendix A Gamma photon techniques for detection of nucleation in super-heated emulsion detectors used in neutron dosimetry

A.1 Introduction

Gamma radiation densitometers which utilize the measurement of gamma attenuation and scattering properties are used in the oil industry to determine Gas Volume Fraction (GVF) [1, 2]. In any nuclear facility with neutron fields, monitoring radiation workers for neutron exposure is highly important and superheated liquid detectors are most suitable for this purpose because of their total insensitivity to gamma rays. Making use of the instability of superheated liquids against bubble formation on radiation exposure reported by Glasser [3], it was Apfel [4] who introduced superheated liquid drops for neutron detection and developed a Superheated Drop Detector (SDD) in which superheated liquid drops are placed into a viscous fluid. Later Ing and Birnborn [5] modified it into Bubble (damage) Detector (BD) where a firm polymer medium is used to confine the droplets. Detailed reviews regarding the theory of bubble formation are available in literature [6-10]. In superheated liquid detectors, on neutron exposure a bubble liquid multiphase exists and the present work investigates the feasibility of gamma radiation based GVF technique as a tool for detecting the population density of bubble nucleation. Insensitivity of bubble detector for gamma radiation and change in attenuation and scattering centers on bubble formation are utilized for this study.

Two bubble detectors are selected for this study, the first one is an indigenously developed one (Sample 1) and the other one is a commercially available one from BTI, Canada (Sample 2). The photographs of the samples before and after exposure are shown in figure A.1.

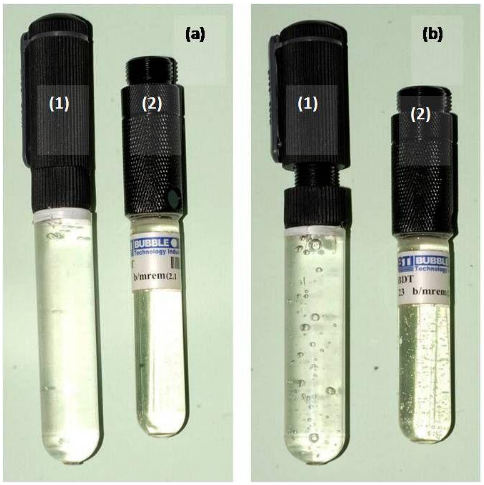

Figure A.1. Photographs of bubble detectors before (a) and after neutron exposure (b)

The liquid droplets become superheated when pressure on the polymer is released by unscrewing the cap. In the superheated condition the transmitted and scattered gamma intensities from these samples before neutron exposure were recorded and confirmed that the samples are insensitive to gamma exposure as no nucleation of the bubbles resulted. Later these samples were exposed to few mSv of dose from Am/Be neutron source (5 Ci) for known intervals of time in order to get desired number of bubbles required to create appreciable change in transmission and scattering intensities. After each exposure the transmitted and scattered intensities were collected. A uniform population density of bubbles throughout the bubble detector medium is assumed on neutron exposure and the same is verified by collecting the intensities at three different vertical locations. These intensities were within the statistical uncertainties and the averages of these intensities were used for further analysis. The bubbles were recompressed after each reading by applying the pressure and the detector was reused.

A.2 Transmission model

The transmitted intensity through an unirradiated bubble detector depends on the thickness of the sample and the composition of the material. Bubble nucleation after neutron exposure results in changes in the attenuation properties of gamma rays and this can be represented by α which is similar to GVF in multiphase flow [2]. In the present case α is the ratio of volume of bubbles to the volume of superheated liquid inside the measurement volume (voxel) which depends upon the population density of bubbles trapped. Attenuation inside the bubble is assumed to be negligible. Transmitted intensity I_t', through the irradiated bubble detector can be written as

$$I_t' = I_{0t} \exp\left(-\mu x(1-\alpha)\right). \tag{A.1}$$

The number of bubbles formed inside the voxel is proportional to exposed neutron dose (*D*) and hence

$$\alpha = kD \tag{A.2}$$

where k is the proportionality constant. On substitution, the value of α, the equation (A.1) can be rewritten as:

$$I_t' = I_{0t} \exp\left(-\mu x(1-kD)\right) = I_t \exp(\mu x k D). \tag{A.3}$$

As per equation (A.3) the transmitted intensity through the irradiated bubble detector increases exponentially with increase in number bubbles or dose and the equation (A.3) can be rewritten as and is given in equation (A.4)

$$y = a\exp(bx) \tag{A.4}$$

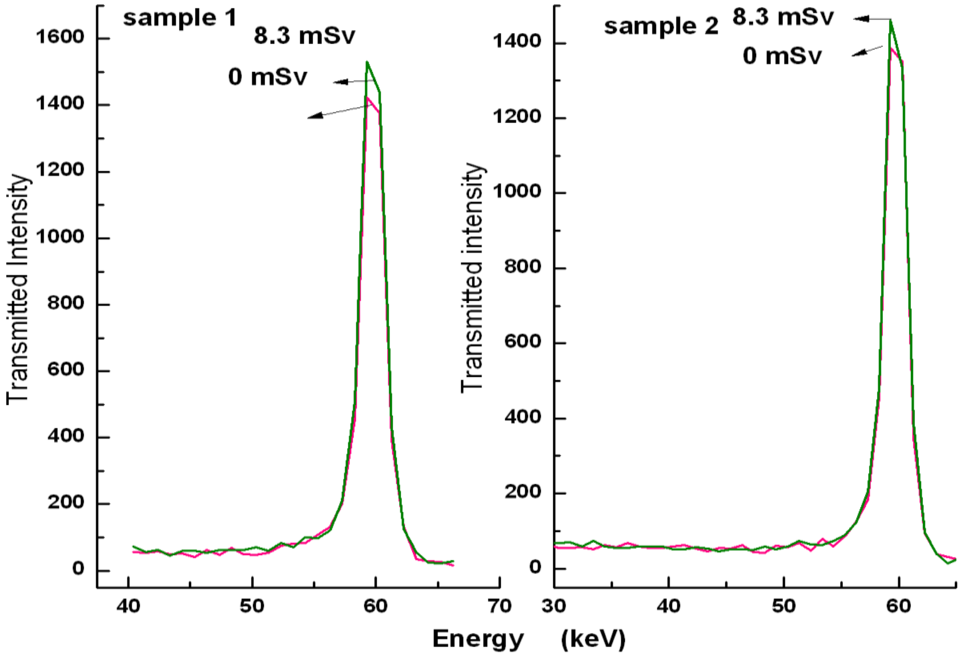

Figure A.2 Transmitted PHS of sample 1 and sample 2 before (0 mSv) and after (8.3 mSv) neutron exposure

Figure A.2 shows the transmitted PHS obtained for both the samples before and after neutron exposure (8.3 mSv). As explained in equation (A.3), increase in number of bubbles results in reduced attenuation and the same can be seen in figure A.2. Thus the transmitted intensity from the bubble detector increases with the increase in population density of bubbles inside the voxel. Transmitted intensity as a function of neutron dose is plotted and is shown in figure A.3. Theoretical model formulated and given in equations (A.3) and (A.4) are used for fitting the experimental data by least square method.

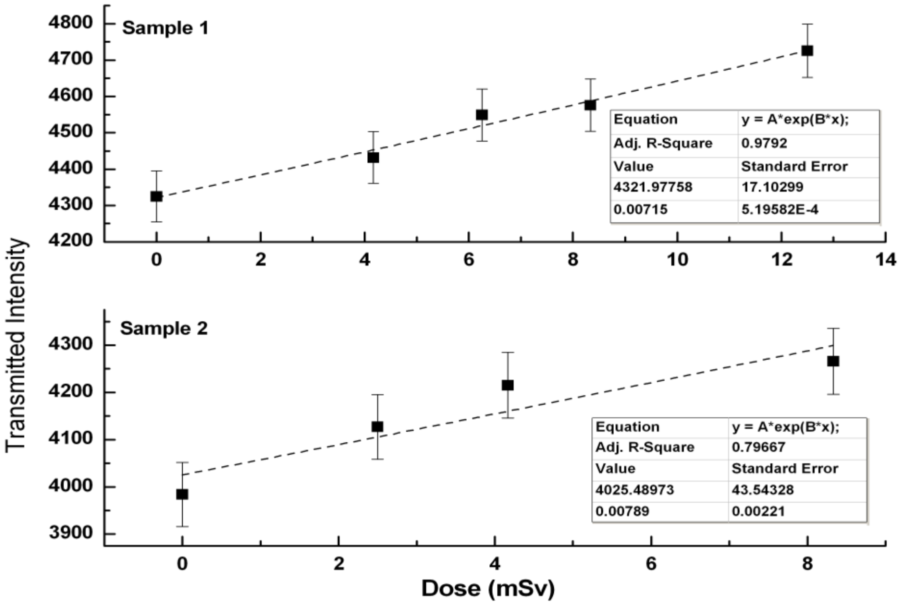

Figure A.3 Experimental transmitted intensities plotted as a function of neutron dose along with the error bars for sample 1 and sample 2. The dashed curve indicates the least square fitting as per the theoretical model formulated and the fitted parameters are shown in the inset.

A.3 Scattering Model

The scattering model explained in section 1.2.3.1 is used for relating the scattered intensity with bubble nucleation. The equation (1.13) is modified for the present case and is given below

$$I_S = K\rho \exp\text{-}\left[\mu d\right]\exp\text{-}\left[\mu' d'\right]V \qquad \text{(A.5)}$$

Here d and d’ are the incident and scattered photon path lengths respectively. As explained in the transmission method, the formation of bubbles on neutron exposure reduces the number of scattering centers and hence the intensity of scattering inside the voxel. Thus the scattered intensity from an exposed sample I_s’ which depends on α can be written as [2]

$$I_{S}' = K\rho\,\mathrm{exp}\text{-}\left[\mu d(1-\alpha)\right]\mathrm{exp}\text{-}\left[\mu' d'(1-\alpha)\right]V(1-\alpha) \tag{A.6}$$

On substitution of equations (A.2) and (A.5), in (A.6)

$$I_{S}' = I_{S}\,\mathrm{exp}\left[\mu dkD)\right]\mathrm{exp}\left[\mu' d' kD\right](1-kD) \tag{A.7}$$

The equation (A.7) can be rewritten into a generalized form as follows

$$y = a\,\mathrm{exp}(bx)\,(1-cx) \tag{A.8}$$

Thus an exponential increase due to reduced attenuation and linear decrease due to reduced scattering are expected in scattered intensity from the neutron irradiated bubble detector depending upon α.

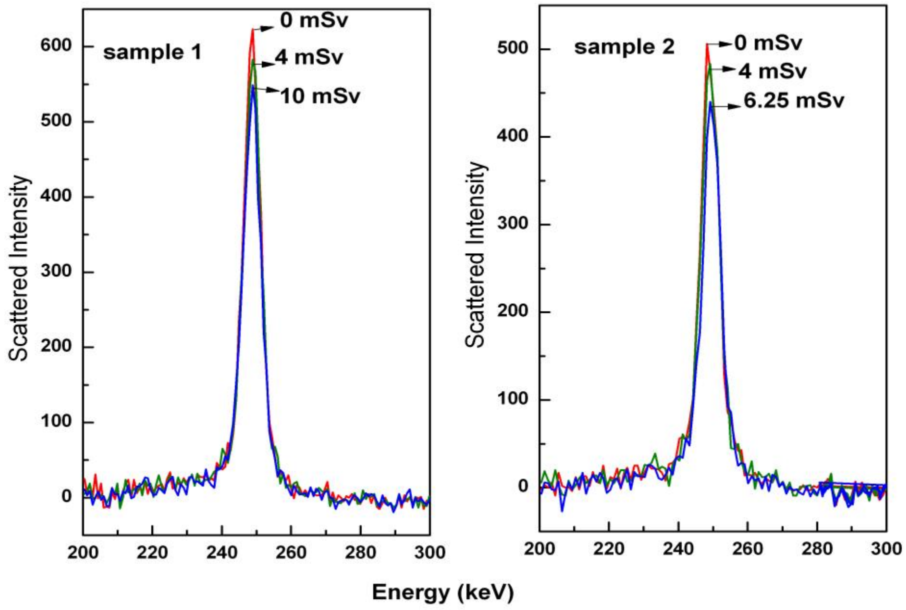

Figure A.4. Scattered PHS of sample 1 and sample 2 before and after neutron exposure for various doses

Figure A.4 shows the scattered PHS obtained from both the samples with and without neutron exposure. The background spectrum is subtracted from each of these spectra and hence the scattered intensity due to increased bubble population is indicated by the differences in PHS. Decrease in scattered intensity is observed with increase in the neutron dose and this is due to the increase in population density of bubbles and hence reduction in scattering centers.

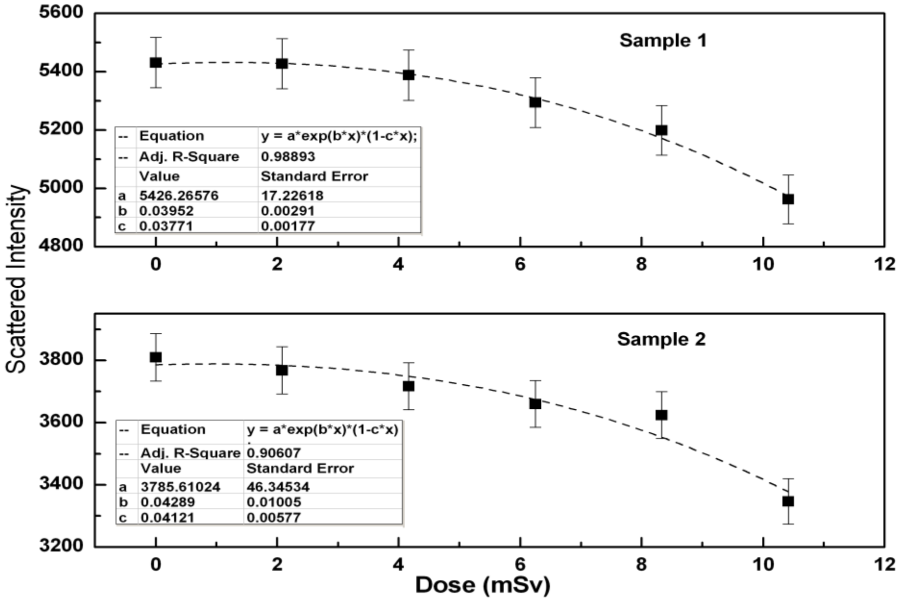

Figure A.5 Experimental scattered intensities plotted as a function of neutron dose along with the error bars for sample 1 and sample 2. The dashed curve indicates the least square fitting as per the theoretical model formulated and the fitted parameters are shown in the inset.

Scattered intensities are plotted as a function of neutron dose which depends on the population density of trapped bubbles and is shown figure A.5. Theoretical scattering model formulated is used for least square fitting of the experimental data. A good agreement with the model is obtained for both the samples. The present experimental set-up where both the sources and the detector are collimated, demands 10 minute scanning per voxel to reduce the statistical uncertainty to less than 2%. This model can be used for calibrating a bubble detector for known exposure doses and the constants obtained from calibration can be used for quantifying the neutron exposure at unknown doses.

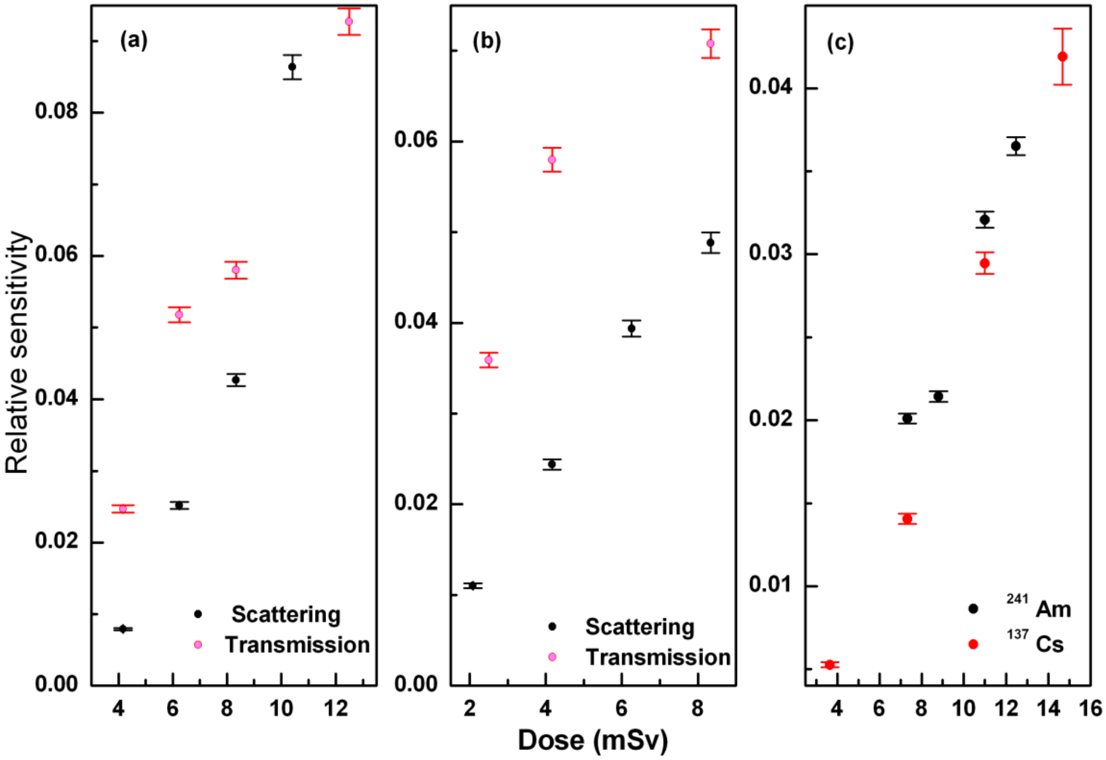

Figure A.6 Relative sensitivities of transmission and scattering techniques for sample 1 and sample 2 as a function of neutron dose (a and b respectively) and relative sensitivities of transmission experiments for 59.54 and 661.6 keV gamma energies (c)

The relative sensitivities for sample 1 and sample 2 are calculated for transmission and scattering methods and plotted as a function of neutron dose in figure A.6(a) and (b) respectively. Relative sensitivity is defined as the change in the scattered or transmitted intensities from an exposed sample with respect to reference intensity (intensity of the unexposed sample). It can be seen from the figure that in the present dose regions studied, the relative sensitivity obtained by transmission technique is higher compared to those obtained by scattering technique and higher the sensitivity, the technique is more efficient. The transmission experiments are also carried out with sample 1 using 661 keV gamma photon energies from ^{137}Cs source. The calculated relative sensitivities (absolute values) as a function of dose at 59.54 and 661.6 keV energies are shown in figure A.6(c) and higher relative sensitivity is seen for 59.54 keV gamma energy compared to those obtained for 661.6 keV. This is because of the higher attenuation coefficients of bubble and polymer media at 59.54 keV compared to 661.6 keV.

Experiments indicate that it is possible to obtain a correlation between neutron dose and transmitted/scattered intensities. The advantage of this technique is that it is more sensitive when the number of bubbles formed is relatively large resulting in practical difficulties of counting them. The present experimental study is limited to high dose environments. In accident dosimetry or criticality measurements, a high dose environment exists and the present photon technique can be effectively used. In the present study PHS are recorded immediately after each irradiation but in bubble detectors generally the bubble size tend to increase as a function of time. The attenuation and scattering parameter change with change in bubble size. Thus the scattered/transmitted intensity recorded immediately after the exposure and after a few days will be different and comparison will not yield same results. For accurate results, the intensities measured under the same experimental geometry and bubble sizes have to be compared.

This work can be considered only as a preliminary study for investigating the viability of this technique. The development of this technique for potential applications warrants further research and experiments especially at lower dose environments with reduced source to sample and sample to detector distance. The present experimental system described is only for the laboratory experiments. But portable source and compact detector systems can be designed and utilized for field study. Owing to the higher relative sensitivity observed in transmission technique, portable transmission gamma ray gauges available can be utilized for this purpose.

References

1. Tjugum, S.A., Johanson, G.A, Holstad, M.B., Radiat. Phys. Chem., 60 (2001), 797-798
2. Tjugum, S.A., Johanson, G.A, Holstad, M.B., Meas. Sci. Technol., 14 (2003), 1777-1782
3. Glaser, D.A., Phys. Rev., 87 (1952), 665-665
4. Apfel, R.E., Nucl. Instrum. Methods, 162 (1979), 603-608
5. Ing, H., Birnboin, H.C., Nucl. Tracks Radiat. Meas., 8 (1984), 285-288
6. Roy, S.C., Roy, B., Current Science, 84 (2003), 516-528
7. Apfel, R.E., Roy, S.C., Radiat. Phys. Chem., 10 (1985), 327-330
8. Roy, S.C., Apfel, R.E., Lo, Y.C., Nucl. Instrum. Meth. A, 255 (1987), 199-206
9. d’Errico, F., Radiat. Prot. Dosim., 84 (1999), 55-62
10. d’Errico, F., Radiat. Prot. Dosim., 120 (2006), 475-479